

Influence of Engineered Roughness on the Flow Instabilities in a Centrifugal Compressor

Model Development & Output Analysis

Prakhar Kapoor

Master of Science Thesis
Report Number: 2641

**Influence of Engineered Roughness on the Flow Instabilities in a
Centrifugal Compressor
Model Development & Output Analysis**

MASTER OF SCIENCE THESIS

For the degree of Master of Science in Mechanical Engineering:
Sustainable Process and Energy Technology at Delft University of
Technology

Prakhar Kapoor

August 29, 2014

Faculty of Mechanical, Maritime and Maritime Engineering (3ME) · Delft University of
Technology

 **mitsubishi turbocharger and engine europe b.v.**

The work in this thesis was supported by Mitsubishi Turbocharger and Engine Europe B.V (MTEE). Their cooperation is hereby gratefully acknowledged.

 **TU Delft** Delft
University of
Technology
All rights reserved.

Copyright © Energy Technology

DELFT UNIVERSITY OF TECHNOLOGY
DEPARTMENT OF
ENERGY TECHNOLOGY

The undersigned hereby certify that they have read and recommend to the Faculty of
Mechanical, Maritime and Maritime Engineering (3ME) for acceptance a thesis
entitled

INFLUENCE OF ENGINEERED ROUGHNESS ON THE FLOW INSTABILITIES IN A
CENTRIFUGAL COMPRESSOR

by

PRAKHAR KAPOOR

in partial fulfillment of the requirements for the degree of

MASTER OF SCIENCE MECHANICAL ENGINEERING: SUSTAINABLE PROCESS AND
ENERGY TECHNOLOGY

Dated: August 29, 2014

Supervisor(s):

Dr. Rene Pecnik

Dr. Adeel Javed

Reader(s):

Dr. Mathieu Pourquie

Prof. Dr. Bendiks Jan Boersma

Abstract

Centrifugal compressors form an integral part of automotive turbochargers. Strict emission regulations and increased engine downsizing in the automotive industry are pushing the turbocharger centrifugal compressors to provide the charged air at very lower mass flow rates. However, at low mass flow rates, the operation and application of centrifugal compressors for a given turbocharger is limited by the fluid dynamic instabilities. These flow instabilities cause the compressor to enter the state of stall and/or surge. Stall defines the lower limit of stable operating range for the compression system. The suppression of this flow instability is a key research focus of turbomachinery aerodynamics. In this thesis, an attempt has been made to reduce the compressor instability and subsequently increase the surge margin by the application of engineered roughness on different compressor parts.

The analysis has been split into two parts. Firstly, CFD analysis have been carried out on several test cases to validate the reliability of the commercial solver. The comparison of the CFD results with the available reference data shows a reasonable agreement in terms of prediction of laminar to turbulent transition location and influence of wall roughness on transition onset location. Secondly, a detailed CFD analysis of the centrifugal compressor has been made in two phases. In the first phase, the overall compressor performance has been simulated from stall to choke over a specific turbocharger rotational speed. In the second phase, a parametric roughness study has been carried out by considering the effects of predefined wall roughness and localized roughness strips on the unstable flow in the compressor at low mass flow rates. For the wall roughness evaluation, the roughness has been applied on the impeller blades, impeller shroud, diffuser and inlet shroud. On the other hand, for the localized roughness strips, roughness have been defined at specific locations at the main blade suction side and the diffuser shroud. The analysis reveals a reduction in flow instability in the compressor domain. The steady state simulations show a significant improvement in the flow structure of the diffuser in terms of the reduction in flow reversal. Furthermore, an improvement in the impeller is observed by reduction in the low momentum wake region.

Table of Contents

Acknowledgments	ix
Nomenclature	xiii
1 Introduction	1
1-1 Motivation	1
1-2 Compressor Stall and Surge	2
1-2-1 Steady Stall	2
1-2-2 Dynamic Stall and Surge	4
1-3 Flow Separation and Boundary Layer Transition	5
1-4 Computational Fluid Dynamics and Transition Modeling	6
1-5 Surface Roughness, Boundary Layer Transition and Applicability to Turbomachinery Flow	7
1-6 Research Questions	8
1-7 Outline of the Thesis Report	9
2 Theoretical Background	11
2-1 RANS Modeling	11
2-1-1 k - ω -SST Turbulence Model	13
2-2 Boundary Layer Transition and Transition Modeling	14
2-2-1 γ - $Re_{\theta t}$ Transition Model	15
2-3 Effect of Surface Roughness on Turbulent Flow Fields	20
2-4 Admissible Roughness	21
3 Validation Cases	23
3-1 Flat Plate	23
3-1-1 Smooth Flat Plate	23
3-1-2 Roughened Flat Plate	24
3-1-3 Flat Plate with Imposed Pressure Gradient	25
3-2 Von Karman Institute Transonic Turbine Guide Vane	28

4	Compressor Performance Evaluation	33
4-1	Compressor Specification	33
4-2	Preprocessing and CFD Setup	34
4-2-1	Geometric Parametrization	34
4-2-2	Computational Mesh and Numerical setup	35
4-2-3	Boundary Conditions	36
4-3	Compressor Performance Analysis	37
4-3-1	Volute Performance Model	37
4-3-2	Performance Curves	39
4-4	Impeller Flow Field Analysis	40
4-5	Flow Phenomenon Responsible for Surge	41
4-5-1	Inlet Recirculation Region	42
4-5-2	Flow Separation within the Impeller	42
4-5-3	Flow Separation within the Vaneless Diffuser	43
5	Roughness Application and Evaluation	47
5-1	Wall Roughness Analysis	47
5-1-1	Effect of Surface Roughness on Diffuser Flow Field	48
5-1-2	Effect of Surface Roughness on Impeller Flow Field	50
5-2	Localized Roughness Strips and their Effect on Flow Field	53
5-2-1	Modeling of Localized Roughness Strips	55
5-2-2	Roughness Parametrization	56
5-2-3	Effects of Roughness Location and Magnitude	56
5-2-4	Effect of Roughness Strips on Diffuser Flow	57
5-2-5	Effect of Roughness Strips on Impeller Flow Field	58
6	Summary and Conclusions	65
A	Reference Data for the Test Cases	69
B	Matlab Code for the Volute Performance Estimation	73
C	Experimental Compressor Map	75
D	Component Wise Mesh Distribution	77
	Bibliography	79

List of Figures

1-1	Inducer velocity triangle and inducer stall [1]	3
1-2	Diffuser velocity triangle [1]	4
2-1	Typical mean velocity distributions, normalized using wall variables, over smooth and rough walls [2]	21
3-1	Variation of skin friction coefficient with Reynolds number for a smooth flat plate	24
3-2	Variation of skin friction coefficient with Reynolds Number for a rough flat plate	25
3-3	Computational domain for flat plate with imposed pressure gradient	26
3-4	Comparison of surface static pressure distribution carried out to validate the computed domain geometry	27
3-5	Effect of trip height on losses at $Tu=0.5$ %	27
3-6	Coefficient of pressure distribution along the plate length	28
3-7	Computational mesh for VKI turbine guide vane	29
3-8	Distribution of heat transfer coefficient over the VKI blade profile.	30
3-9	Skin fiction distribution over the VKI blade profile.	31
4-1	The modeled impeller geometry for the computational fluid dynamic analysis . .	34
4-2	Computational domain for the test compressor	35
4-3	The mesh for computational fluid dynamic analysis	36
4-4	Comparison of the experimental and simulated performance curves for the test compressor	39
4-5	Relative Mach number, meridional velocity and static entropy contours at different streamwise direction at the best efficiency point	41
4-6	Relative Mach number contour at a section located at 80% of impeller spanwise direction	42
4-7	Meridional velocity contours at the diffuser midplane for different flow rates . .	43
4-8	Relative velocity contours at the midspan of the impeller domain	44

4-9	Relative velocity streamlines depicting the secondary flow structure at different operating points	45
4-10	Meridional velocity contours at the diffuser mid-plane for different flow rates . . .	46
5-1	Meridional velocity streamlines along the diffuser meridional plane for different surface roughness	49
5-2	Streamwise locations used to study the spanwise distribution of radial and tangential velocities in the diffuser	50
5-3	Variation of radial velocity from hub to shroud at different streamwise locations (Fig 5-2) along the diffuser	51
5-4	Variation of tangential velocity from hub to shroud at different streamwise locations (Fig 5-2) along the diffuser	52
5-5	Normalized total pressure contours on a section located at 70 % of the impeller spanwise direction	53
5-6	Variation of meridional velocity from the inlet to the outlet of the impeller domain mid span.	54
5-7	Meridional velocity contours of a location close to the trailing edge	54
5-8	Circumferential mass flux distribution at the impeller trailing edge for the different roughness cases	55
5-9	Modified impeller and diffuser domain for the parametric roughness study	56
5-10	Modification of the radial velocity distribution as a result of the localized roughness applied to strip I at the diffuser	58
5-11	Modification of the radial velocity distribution as a result of the localized roughness applied to strip II at the diffuser	59
5-12	Modification of the mass flux distribution as a result of the localized roughness applied to strip 1 at the impeller	60
5-13	Meridional velocity contours depicting the influence of roughness strip 1 on the meridional velocity distribution at the impeller trailing edge	61
5-14	Modification of the mass flux distribution as a result of the localized roughness applied to strip 2 at the impeller	62
5-15	Meridional velocity contours location depicting the influence of roughness strip 2 on the meridional velocity distribution at the impeller trailing edge	62
5-16	Modification of the mass flux distribution as a result of the localized roughness applied to strip 3 at the impeller	63
5-17	Meridional velocity contours depicting the influence of roughness strip 3 on the meridional velocity distribution at the impeller trailing edge	63
C-1	Experimental map of the test compressor	75

List of Tables

3-1	Surface trip parameters	26
3-2	VKI transonic blade geometric parameters	29
3-3	Data pertaining to the VKI turbine guide vane test cases. $M_{is,out}$ and $Re_{c,out}$ are the outlet Reynolds number and Mach number based on the blades chord. Re_M is the Reynolds number based on the velocity and mesh spacing of the turbulence grid in the experimental arrangement, used to obtain specific dissipation rate ω [3]	29
4-1	Compressor specification	34
5-1	Magnitudes of considered roughness elements	48
5-2	Roughness magnitude and location	57
A-1	Boundary data corresponding to the smooth flat plate	69
A-2	Boundary data corresponding to the roughened flat plate	70
A-3	Boundary data corresponding to the roughened flat plate with imposed pressure gradient	70
A-4	Boundary data corresponding to the turbomachinery test case-VKI transonic turbine guide vane	71
D-1	Component wise mesh in the compressor domain	77

Acknowledgments

The completion of the Master thesis would not have been possible without the able assistance of some people, whom I would like to thank.

Firstly, I would like to acknowledge my University supervisor Dr. Ir. Rene Pecnik. I consider myself fortunate to have you as my supervisor. Without your diligence, enthusiasm and direction, my work would not have been productive. Your approach towards problem solving and defining the project scope helped me to streamline the work and the report itself. Thank you very much for your support throughout the study.

Further, I am grateful to MTEE for providing me the opportunity to experience their company. Their cooperation and assistance during the project period is truly appreciated. But, I would like to convey a special thanks to my supervisor Dr. Adeel Javed, who was always available to help me out during the 1 year period of mine at MTEE. I honestly appreciate your willingness to discuss even the smallest of problems with me during the course of this work despite being engaged with your Ph.D. defense. Moreover, a special thanks to all my colleagues at MTEE for being generous enough to a non-Dutch speaker.

I want to express my deepest gratitude to the examination committee. I appreciate their time devoted to reading and evaluating this document.

Also, I am grateful to Ir. Enrico Ranaldi, Ir. Uttiya Sengupta and Ir. Hassan Nemati for their participation and out of the way help for reviewing my work. I would also take this opportunity to thank the staff of department of Process and Energy for arranging everything that I required during the period of my thesis work.

My special gratitude to my fellow friends and colleagues at TU Delft for their enthusiasm and help during the testing periods during the project.

Finally, I would like to thank my parents for their selfless love and support in the completion of the studies and the project in particular. They have been a continuous source of motivation that has propelled me over the time. I owe everything that I am today to them. Thank you for making it all possible

Delft, University of Technology
August 29, 2014

Prakhar Kapoor

Master of Science Thesis

Prakhar Kapoor

"The only way of discovering the limits of the possible is to venture a little way past them into the impossible."

— *Arthur C. Clarke*

Nomenclature

Symbol	Description	Units
A	Area	mm^2
b	Width	m
C_f	Skin friction coefficient	-
C_p	Coefficient of pressure	-
D	Diameter	mm
h	Heat transfer coefficient	W/m^2K
i	incidence angle	$^\circ$
K	Loss coefficient	m/s
k	Turbulent kinetic energy	m^2/s^2
	Geometric roughness	μm
k_s	Equivalent sand grain roughness	mm
l^*	Length scale	m
M	Mach number,	-
	Mass flux	$kg/m^2/s$
N	Rotational Speed	$r.p.m$
p	Instantaneous pressure	Pa
q	Heat flux	W/m^2
R_a	Arithmetic meanline roughness	μm
Re	Reynolds number	-
Re_T	Turbulent Reynolds number	-
Re_v	Vorticity Reynolds number	-
Re_θ	Momentum thickness Reynolds number	-
$Re_{\theta t}$	Transition onset momentum thickness Reynolds number	-
$\overline{Re}_{\theta t}$	Local transition onset momentum thickness Reynolds number	-
r	radius	mm
T	Temperature	K
Tu	Turbulence intensity	%
U	Blade Peripheral Velocity	m/s
u	Instantaneous velocity	m/s

u_τ	Wall friction velocity	-
u^*	Velocity scale	m/s
V	Absolute velocity	m/s
W	Relative velocity	m/s
y^+	Non-dimensional wall distance	-
Greek symbols		
β	Inlet flow angle	$^\circ$
β_b	Blade angle	$^\circ$
ϵ	Loss coefficient	-
η	Efficiency	-
μ	Dynamic viscosity	$Pa.s$
ν	Kinematic viscosity	m^2/s
ν_t	Kinematic eddy viscosity	m^2/s
π	Pressure ratio	-
θ	Boundary layer thickness	mm
	Circumferential angle	$^\circ$
ρ	Density	kg/m^3
τ	Wall sheer stress	Pa
ω	Turbulence eddy frequency	$1/s$
Subscript		
0	Total or stagnation state	
1	Impeller inlet	
2	Impeller outlet	
5	Diffuser exit	
6	Return bend exit	
7	Volute exit	
∞	Free stream	
m	Meridional component	
r	Radial component	
t	Tangential component	
w	wall	
Abbreviations		
CFD	Computational fluid dynamics	
MTEE	Mitsubishi Turbocharger and Engine Europe B.V.	
PS	Pressure side	
SS	Suction side	
SST	Shear stress transport	

Chapter 1

Introduction

1-1 Motivation

The stability of the centrifugal compressors is limited at low mass flow rates by surge, rotating stall or a combination of both. These instabilities have a detrimental effect on the system and should be avoided. In the case of specific application of centrifugal compressors in the automotive turbochargers, this aspect becomes even more important. The demand for fuel economy and emission reduction calls for engine down sizing. The automotive turbochargers compensates for the performance loss accounted by the downsizing requirements. For a turbocharged engine, some of the engine operating points lie close to the surge limit of the compressor. Operation of the compressor at these operating points results in large flow separations in the centrifugal compressor and eventually leads to surge. Furthermore, it causes vibratory stresses in the blading of the compressor. Thus, it becomes essential to devise techniques that can delay flow separation and hence increase the stability range of the centrifugal compressor by increasing the surge margin. The current work thus focuses on studying the effect on the flow instabilities inside the centrifugal compressor due to the addition of roughness patches on the impeller and the diffuser.

The instabilities at low mass flow rates essentially initiate as a result of the stall. Stall can be defined as a phenomenon, wherein the flow is separated from its path walls. A diffusing flow along a surface or wall might retard so severely that it can no longer follow the surface. In this case, the streamlines close to the wall will leave the wall and reverse flow regions develop from that point along the wall surface. In other words, momentum in the streamlines close to the wall is insufficient to overcome the adverse pressure gradient and viscous shear stress along the wall. When the viscous shear effect and the adverse pressure gradient force the streamlines to deviate from the surface, the flow is said to be stalled. Stage stall is said to occur when one or more of the elements in a compressor stage gets stalled. In this case, the overall pressure ratio vs. flow characteristic is no longer stable [1]. The subsequent literature gives a brief introduction to the phenomenon of stall and surge.

1-2 Compressor Stall and Surge

The compressor stall and surge is one of the most-significant criterion that defines the limit of operation of the machine. The current section of the chapter tries to introduce and elaborate upon compressor stall which forms a precursor to the surge. The aspect of the steady state and dynamic stall has been elaborated and presented in the following sections.

1-2-1 Steady Stall

The phenomenon of stall involves flow separation along the compressor wall. Stall occurs as a result of singular separation and/or three-dimensional separation. Singular separation can be defined as a phenomenon where the fluid flow is affected as a result of an adverse pressure gradient. As a consequence of the adverse pressure gradient, the fluid element close to the wall separates resulting in the formation of a recirculating fluid flow region (separation bubble) near the surface. The three-dimensional or ordinary separation is attributed to the presence of secondary flow. The secondary flow results as a result of the pressure gradient in cross-channel direction. If a secondary flow is present, it redirects the boundary layer flow such that it cannot have a positive through-flow component. In the case of centrifugal compressors, the ordinary separation occurs, for instance, in the vaneless diffuser where the streamlines in proximity of the wall do not have a positive radial component, but have a strong velocity component in the tangential direction. As a result, the dividing streamlines are directed back towards the tip of the impeller and a back-flow condition results.

Depending on the flow conditions and geometrical features of a compressor the separation can occur in the inducer, impeller, vaneless diffuser or the volute; which will be discussed in more detail below.

Inducer Stall and Recirculation

The velocity triangle at the impeller inlet is shown in the Fig.1-1. According to Japikse [1], at a given rotational speed as the mass flow rate is decreased, the inlet flow angle (β) increases thus causing an increase in the incidence angle. As the incidence angle increases, the flow is required to accelerate more around the leading edge. This causes a strong diffusion in the flow in order to bring surface streamlines into balance with adjacent streamlines. This strong diffusion causes the flow to separate from the surface at a high level of incidence.

Vaneless Diffuser Stall

The vaneless diffusers can be subjected to either singular or ordinary separation in addition to the rotating stall (1-2-2). Singular separation is rarely encountered while ordinary separation is very common in vaneless diffuser [1].

The velocity triangle at the diffuser is presented in Fig. 1-2. The performance of the vaneless diffuser is given by the following equation:

$$rV_t = \text{constant} \quad (1-1)$$

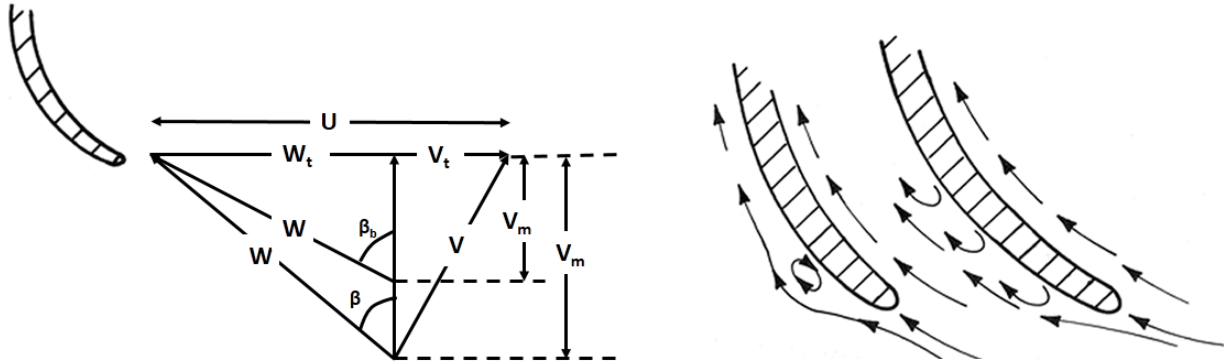


Figure 1-1: Inducer velocity triangle and inducer stall [1]

$$\rho \cdot V_m \cdot 2\pi r b = m \quad (1-2)$$

$$\tan \alpha = \frac{V_t}{V_m} \quad (1-3)$$

The above equations represent the conservation of mass and momentum through the vaneless diffuser. The equations also show that the flow angle in the vaneless diffuser depends on density and passage depth. Thus, assuming a constant density fluid the flow angle is constant at a given flow rate resulting in a logarithmic spiral path through the vaneless diffuser. The through-flow component of the flow tends to follow the log spiral closely. However, the flow streamlines close to the wall have low kinetic energy. As a consequence, they have a lower magnitude of the meridional component of the flow, while subjected to the same radial pressure gradient. Thus, they can no longer follow the constant flow angle characteristics. In this case, the flow separates. [1].

Impeller Stall

When the flow enters the impeller passage, boundary layer development begins at the impeller blades, shroud and hub surfaces. As the flow proceeds through the impeller passage, both the core flow and the boundary layers are subjected to a complex force field and a complex flow pattern develops [4]. As the flow turns from the axial to the radial direction within a compressors impeller, it experiences strong cross-passage force field or the Coriolis force field. Since the Coriolis force is a function of the rotational speed and the velocity of fluid element, it tends to separate the high-velocity and the low-velocity fluid elements. This results in a secondary flow around the core flow with the low momentum fluid collected in proximity of the shrouds' suction surface while, the high momentum fluid is accumulated close to the hub pressure surface [4]. Furthermore, the strong cross-channel Coriolis forces results in a

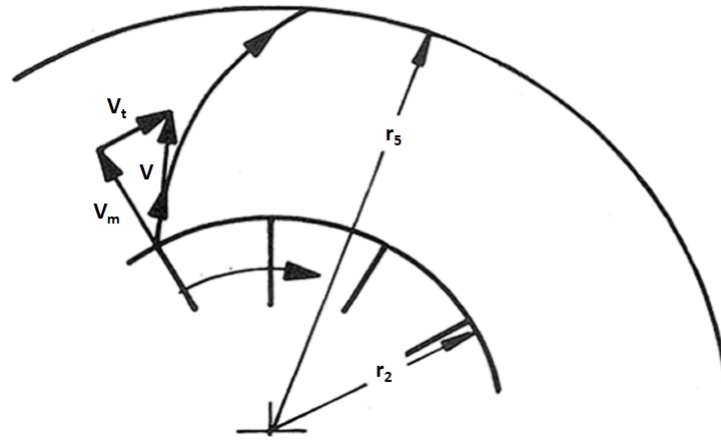


Figure 1-2: Diffuser velocity triangle [1]

skewed boundary layer. The skewed boundary layers are likely to separate in the passage [1]. Additionally, the core flow is affected by the tip clearance flows.

Volute Stall

The volute also forms a source of the stall in centrifugal compressors. The performance of the volute varies along a speed-line as the flow rate varies. The volute is designed so that the flow accelerates through it for the right portion of the compressor map [1]. However, as the mass-flow rate is reduced at a given operating speed, the flow conditions change. The flow becomes non-accelerating and diffusing with a further reduction in mass flow rate due to the increase in the tangential velocity [1]. Thus, the volute functions as a conical diffuser and might enter into a stall mode.

1-2-2 Dynamic Stall and Surge

With the reduction in the mass flow rate through the compressor, two types of unsteady flow phenomenon can be observed in a centrifugal compressor, namely dynamic stall and surge. Dynamic stall or rotating stall is characterized by periodic flow and pressure variations in one or more different components of the compressor [5]. Stationary stalled cells travel around the compressor annulus in a circumferential direction. The angular velocity of the disturbance propagation ranges from 20 % of the impeller rotational speed to a velocity larger than the impellers' angular velocity [6]. Rotating stall is frequently observed at the negative slope side of the compressor performance map. The rotating stall is observed most often at low rotational speeds. At high rotational speed, it triggers surge [4]. Dynamic stall results due to the destabilization of the impeller flow, diffuser flow or because of an unsteady interaction between the diffuser and impeller flow.

The most-common type of rotating stall in the case of a centrifugal compressor is observed in a vaneless diffuser. The literature review reveals various analytical and experimental approaches to investigate the phenomenon of rotating stall in the case of diffuser of a centrifugal

compressor. According to Jansen [5], the three-dimensional boundary layer associated with the diffuser explains the phenomenon of the rotating stall. A necessary (but not sufficient condition) for occurrence of the rotating stall in diffuser is the three-dimensional flow separation [5]. Similar theory is presented in the works of Senoo and Kinoshita [7], Fringe and Van den Braembussche [8]. On the other hand, Tsujimoto *et al.* [9] suggested the existence of a two-dimensional core flow instability at the instigation of rotating stall in a centrifugal compressor.

Another form of the unsteady flow behavior that results in a centrifugal compressor is known as surge. Surge consists of strong mass flow and pressure oscillations. It is a system phenomenon and involves periodic breakdown of the flow through the compressor with periods of complete backflow [1]. As a result, the average mass flow rate at a cross section changes with time. In addition to the compressor fluid dynamics, surge also depends on the dynamic properties of the system (throttle resistance, inlet and outlet ducting) in which the compressor operates [6]. Surge can be further classified as mild, classic, modified and deep surge [10]. In the case of mild and classic surge, no flow reversals occur. However, periodic pressure fluctuations are high for the classic surge whereas they are small for mild surge. Modified surge is a combination of the classic surge and rotating stall. The deep surge is a stronger version of the classic surge and involves flow reversals [10].

1-3 Flow Separation and Boundary Layer Transition

As pointed out in the previous section, one of the primary causes of flow instabilities in a centrifugal compressor is separation of flow along the walls of the compressor. This section of the chapter describes in detail about the basic phenomenon behind flow separation and boundary layer transition.

According to Simpson [11], the term separation refers to the entire process of "departure" or "breakaway" or "the breakdown" of the boundary layer flow. The basic phenomenon responsible for the separation of boundary layer is excessive momentum loss near the wall. This happens in a boundary layer trying to move downstream against an increasing pressure gradient, $\frac{dp}{dx} > 0$.

The change in state of boundary layer from laminar to turbulent is termed as boundary layer transition. The major factors affecting the transition process are adverse pressure gradient, surface roughness, and free stream turbulence [12]. According to Mayle [13], there are three important modes of transition namely: natural transition, bypass transition and separated flow transition. Natural transition occurs at low free stream turbulence level and begins with weak instability in the laminar boundary layer (Tollmien-Schlichting waves). These weak instabilities are amplified at various stages till the flow becomes fully turbulent. The second mode of transition or the bypass transition is seen in the flows involving high free stream turbulence levels. The third mode also referred as separated flow transition occurs when a laminar boundary layer separates under the influence of adverse pressure gradient. The flow separation can cause a transition in the free shear layer like flow close to the surface and subsequent reattachment [13]. A volume of recirculating fluid also known as Laminar separation bubble (LSB) develops between the separation and the reattachment point at the

surface [13]. This recirculating region of fluid might cause adverse effects such as an increase in drag, decrease of lift force, noise and vibrations [12].

1-4 Computational Fluid Dynamics and Transition Modeling

Over the years, significant progress has been made to develop turbulence models that allow to simulate fully turbulent engineering flows accurately. A large domain of models has been developed which can be employed for different applications. However, majority of the available turbulence models do not include capabilities to model laminar-turbulent transition accurately. The primary reason for this is that transition modeling does not provide the same gamut of CFD-compatible models as available for turbulent flows [14].

Currently, there are methodologies available for modeling and predicting transition in the industry. These are correlation-based models, low Reynolds number (Re) based models and models based on stability analysis [14]. The low-Re based models make use of wall damping terms in order to model the behavior of the viscous sublayer. These models do not require any wall functions [3]. To model transition, they rely on the diffusion of free stream turbulence into the boundary layer and interaction of this free stream turbulence with the model source term. Some of the low-Re number models have been capable of predicting the transition fairly accurately at reasonable Reynolds number. However, their applicability to predict transition is coincidental due to the similarities between the viscous sublayer and developing boundary layer where turbulence production is damped [15].

An alternate approach to predict transition is the e^n method. The model is based on the local linear stability theory and parallel flow assumption. It computes the growth of disturbance amplitudes from the boundary layer neutral point to the transition location [15]. One of the inherent problems with the e^n method is that n-factor does not represent the disturbance amplitude in the boundary layer, but instead is the amplification factor from an initial unknown amplitude. The initial amplitude of the disturbance is related to the external disturbance environment through unknown receptivity process. Thus, the n-factor is not universal at the transition onset and must be determined through calibration to wind tunnel or flight tests. Furthermore, e^n method does not predict transition accurately in case of separated flow transition. In this case, laminar solution is separated and exhibits unsteady vortex shedding. Thus, it is not possible in this case to compute local growth rates. Also, another drawback of this method is its inability to predict bypass transition and surface roughness induced transition [15].

The third methodology employed for transition modeling is the empirical correlation-based models. The empirical correlations provide a relation between the free stream turbulence intensity and transition Reynolds number based on the momentum thickness Reynolds number ($Re_{\theta t}$). In order to employ empirical correlations for transition onset, the laminar solution around the body of interest must be first determined. After this, the boundary layer quantities are then integrated to obtain the momentum thickness Reynolds number (Re_{θ}). The transition onset is thus assumed to occur when the local value of the momentum thickness exceeds the one predicted by the correlation. Once the transition onset location is estimated, a turbulence model is turned on, and the subsequent flow development is calculated [15].

In the current work a correlation based transition model ($\gamma - Re_{\theta}$) has been used. The

model is available within the commercial software package ANSYS CFX, which will be used to perform the current study and research in perspective. The model as documented in refs. [16] and [17], consists of two aspects. The first is a generic infrastructure that provides two transport equations which link the CFD codes to experimental correlations. The first transport equation is for intermittency, which is used to trigger the transition process. The second transport equation is solved for the transition onset momentum thickness Reynolds number. This second transport equation is an integral part of the model as it links the empirical correlation to onset criterion in the intermittency equation. The second integral aspect of the model are the empirical correlations.

1-5 Surface Roughness, Boundary Layer Transition and Applicability to Turbomachinery Flow

Surface roughness has a profound impact on the boundary layer transition. The existence of roughness causes an increase in the flow instability and accelerates the onset of transition. Boundary layer tripping using surface roughnesses is employed in various engineering applications. For instance, boundary layer tripping is desired in scramjet as well as heat exchanger design to enhance the mixing and heat transfer rates. Laminar separation on aerodynamic surfaces can be avoided by increasing the surface roughness to cause an early transition. Separation can occur from localized adverse pressure gradients and results in a reduction in aerodynamic efficiencies of these surfaces as a consequence of the increase in the pressure drag. In the situations, where the laminar separation is about to occur, tripping the boundary layer so that it remains attached is preferable. In the case of the separated flows, transition of laminar boundary layer is desired because of the ability of the turbulent boundary layer to remain attached as a result of the higher momentum as a consequence of the turbulent mixing [18]. In the view of Jonas *et al.* [19] the flow structure at rough surfaces assumes local flow separations. Wake regions composed of counter-rotating vortex pairs originating at the surface of roughness elements attached to the basic surface. These separations result in local pressure distributions, which cause a local form of drag acting on the surface together with the viscous wall shear stress [19]. It also results in a roughness sublayer. Vortices' that have a length scale proportional to the length scale of roughness elements are shed into the flow above the crest of the elements. At a distance, the roughness induced sublayer structure blends into the flow. Furthermore, the vortices' are suppressed by viscosity at low Reynolds number, and they accelerate the transition process with the increasing Reynolds number.

A lot of work has been done in investigating the effect of surface roughness on turbulent flows. However, the influence of roughness on transition has been primarily limited to the effect of isolated roughness elements in tripping the boundary layer.

The effect of surface roughness on the turbulent flow structure was closely studied by Nikuradse [20]. His pressure loss data obtained with sand roughened pipe walls revealed the dependencies of different flow regimes on different surface roughness and Reynolds number. In his work, Nikuradse defined a dimensionless parameter, $k^+ = \frac{k_s v_*}{\nu}$, based on the diameter of the sand grain (k_s), wall friction velocity (v_*) and dynamic viscosity (ν) [21]. For the value of this parameter greater than 70, the loss coefficient is only a function of k_s . Where as for values of k_s between 5 and 70, both Re and k^+ form important parameters [21]. Based on his results,

Nikuradsi [20] defined three flow regimes. In the Hydraulically smooth regime ($0 < k_s < 5$), size of the roughness is so small that it does not have a considerable impact on pressure loss. In the transition regime ($5 < k^+ < 70$), the resistance elements protrude out of the viscous sublayer and additional resistance is experienced due to the additional drag. In the completely rough regime $k^+ > 70$, all the roughness elements protrude outside the viscous sublayer and largest part of resistance to flow is in the form of a drag. Furthermore, Schlichting formulated the concept of equivalent sand grain roughness as a means of converting the roughness data and measurements corresponding to other flow profiles into a roughness profile equivalent to the roughness data used by Nikuradse [22]. Colman *et al.* [23] provided further corrections to the assumptions made by Schlichting in his work and correlations have been developed by Simpson [24].

The literature pertaining to influence of surface roughness on laminar to turbulent boundary layer is limited. Doenhoff and Horton [25] reported that in case of an aerofoil, distributed roughness at a specific location downstream the stagnation point resulted in an earlier transition. However, it was also apparent that a similar effect could also be achieved through small strips of roughness. Pinson and Wang [26] showed that the roughness height and not the roughness geometry is the primary parameter in case of the roughness induced effects. With the increase in the velocity, the earlier transition onset and heat transfer enhancement in case of a turbulent boundary layer are roughness dependent.

Zhang and Hudson [27] conducted a parametric study of roughness elements including roughness type size and location under steady and unsteady flow conditions on a flat plate with adverse pressure gradient. The boundary layer was subjected to the pressure distribution representative of an ultra high lift low-pressure turbine. In their work, they reported that the combined effect of the surface roughness and unsteady wakes can reduce the profile losses of ultra highly loaded LP turbine blades. For these blades, a large separation is formed due to high-pressure gradient and low wake passing frequency. There is an optimum height for roughness elements. These elements do not induce transition immediately after itself but only aids in hastening transition in the separated shear layer. In addition to this, they reported that the step type roughness elements more effective at inducing boundary layer transition as compared to wire-type roughness elements.

1-6 Research Questions

As introduced in the previous section, the operational range of the centrifugal compressors is limited at low mass flow rates by surge. The phenomenon of surge essentially stems from the flow instabilities in the form of separation and reversals that occur within the compressors flow domain. In the scope of this thesis, the aerodynamic phenomenon resulting in a reduction in stable operating range of the centrifugal compressor are identified and quantified. Furthermore, the following research topics will be addressed:

- Validation of transition.
- Validation of transition with surface roughness.
- Performance prediction of a smooth walled compressor.

- Effect of surface roughness on the flow instability in a centrifugal compressor.

These research questions will be addressed by performing steady state simulations on a commercial CFD tool ANSYS CFX.

1-7 Outline of the Thesis Report

Chapter 2 presents the theoretical background pertaining to turbulence modeling, boundary layer transition, numerical modeling of the transition and effect of surface roughness on flow fields. Brief overview is presented related to Reynolds averaged Navier-Stokes equation, the formulation of low Reynolds number $k-\omega$ SST turbulence model, the $\gamma-Re_\theta$ transition model and admissible surface roughness. **Chapter 3** discusses and validates the ability of the transition model formulation available in CFX by validating the results of various test cases, **Chapter 4** deals with the computational set up in ANSYS CFX to simulate the performance of the test compressor. Furthermore, it provides a brief description about the inception of flow instabilities in a centrifugal compressor. The report proceeds to **Chapter 5** where the effect of surface roughness on the flow instabilities in a centrifugal compressor is investigated. A parametric roughness study is presented in this chapter to gain further insights on the effect of roughness location and height. The report is completed with **Chapter 6** providing the conclusions and recommendations.

Theoretical Background

This chapter reviews the literature pertaining to turbulence modeling, boundary layer transition and influence of surface roughness on transition. Brief discussion of the turbulence modeling and the model ($k-\omega$ SST) is presented in section 2-1. Furthermore, a study of the phenomenon of laminar to turbulent transition and its aspect of numerical modeling is presented in section 2-2. Next, the effect of roughness on turbulent flow field is discussed in section 2-3. Finally, the chapter ends by a review of the influence of surface roughness on the laminar to turbulent transition in 2-4.

2-1 RANS Modeling

The motion of a fluid can be completely described in terms of its continuity and momentum equations. These equations collectively are referred as the Navier-Stokes equation. Neglecting the effects of body forces, frame rotation and denoting density, kinematic viscosity, pressure and velocity by ρ , ν , p , v respectively, the Navier-Stokes equation for an incompressible fluid is given by:

$$\frac{\partial u_i}{\partial x_i} = 0 \quad (2-1)$$

$$\frac{\partial u_i}{\partial t} + u_j \frac{\partial u_i}{\partial x_j} = -\frac{1}{\rho} \frac{\partial p}{\partial x_i} + \nu \frac{\partial^2 u_i}{\partial x_j^2} \quad (2-2)$$

The equation (2-1) represents the conservation of mass, while the equation (2-2) relates to the momentum conservation of the fluid volume. Despite the availability of sophisticated and powerful computational resources, the estimation and resolution of all the scales of turbulent flows is a challenging affair. The Reynolds-averaged Navier-Stokes equations or simply the RANS equation offer a solution to the above problem. The RANS equation is based on the concept of Reynolds decomposition, which involves the decomposition of an instantaneous

quantity into a mean and fluctuating component. Following the Reynolds decomposition the instantaneous velocity u and the instantaneous pressure p can be expressed as:

$$u_i = \bar{u}_i + u'_i \quad p = \bar{p} + p' \quad (2-3)$$

where, \bar{u}_i is the mean velocity, u'_i is the fluctuating velocity, \bar{p} is the mean pressure and p' is the pressure fluctuation. Substituting the above decomposition in the Navier Stokes equation (equations 2-1 and 2-2) results in the following equation:

$$\begin{aligned} \frac{\partial}{\partial x_i}(\bar{u}_i + u'_i) &= 0 \\ \frac{\partial}{\partial t}(\bar{u}_i + u'_i) + (\bar{u}_j + u'_j) \frac{\partial}{\partial x_j}(\bar{u}_i + u'_i) &= -\frac{1}{\rho} \frac{\partial}{\partial x_i}(\bar{p} + p') + \nu \frac{\partial^2}{\partial^2 x_j}(\bar{u}_i + u'_i) \end{aligned} \quad (2-4)$$

Applying the Reynolds decomposition followed by statistical averaging to equation 2-4, the above equation reduces to

$$\begin{aligned} \frac{\partial \bar{u}_i}{\partial x_i} &= 0 \\ \frac{\partial \bar{u}_i}{\partial t} + \bar{u}_j \frac{\partial \bar{u}_i}{\partial x_j} &= -\frac{1}{\rho} \frac{\partial \bar{p}}{\partial x_i} + \nu \frac{\partial^2 \bar{u}_i}{\partial^2 x_j} - \overline{\frac{\partial u'_i u'_j}{\partial x_j}} \end{aligned} \quad (2-5)$$

The above set of equations is referred as Reynolds-averaged Navier-Stokes Equation. The obtained equation is similar to the original Navier-Stokes equation, except for an additional last term. The extra term designates Reynolds stress. For a statistically three-dimensional flow, four independent equations govern the mean velocity field, the three components of the Reynolds equation and along with the mean continuity equation [28]. However, these four equations contain more than four unknowns. Apart from \bar{u} and \bar{p} , there are also the Reynolds stresses. Such set of equations with more unknowns than the equations are referred as unclosed. This formulates the closure problem of the Reynolds equations i.e, these equations cannot be solved unless the Reynolds stresses are somehow determined [28].

The Reynolds stress terms directly arise from the flow and the length scales of the perturbations, which are the typical scales we are dealing. Thus, it becomes impossible to assume a universal value for all the cases and thus they need to be modeled accurately [28]. In order to solve the problem, the turbulent viscosity hypothesis proposed by Boussinesq is used. The Boussinesq hypothesis relates the deviatoric Reynolds stress to the mean rate of flow.

$$\overline{u'_i u'_j} = \frac{2}{3} k - \nu_t \left(\frac{\partial \bar{u}_i}{\partial x_j} + \frac{\partial \bar{u}_j}{\partial x_i} \right) \quad (2-6)$$

where, ν_t is the turbulent viscosity or eddy viscosity and k is the kinetic energy of fluctuations.

The above equation (2-6) provides a closure to the Reynolds equations (2-5) provided that an appropriate specification of the turbulent viscosity (ν_t) is determined. Furthermore, the turbulent viscosity (ν_t) can be expressed as a function of the length scale (l^*) and velocity scale (u^*), according to the following expression

$$\nu_t = u^* l^* \quad (2-7)$$

Thus, to provide an estimate of the turbulence viscosity, the length scale and the velocity scale must be specified. Different turbulent models achieve this in different ways. For instance, in case of the mixing-length model, the length scale is defined on the basis of the geometry of the flow. Whereas, in case of the two-equation k - ϵ model, the length scale and velocity scale are related to the turbulence kinetic energy (k) and dissipation rate (ϵ) for which the transport equations are solved.

The k - ω -SST turbulence model is used for the current work. The model is described in detail in the subsequent section.

2-1-1 k - ω -SST Turbulence Model

The k - ω -SST as proposed by Menter [29] is a two-equation eddy viscosity model that effectively blends the robust formulation of k - ω model in the near-wall region with the far stream independence of k - ϵ model. To achieve this, the k - ϵ model is converted to a k - ω formulation. The standard k - ω model and the altered k - ϵ model are first multiplied by a blending function and then added together. The blending function takes a value of one in the near wall region, which switches k - ω formulation. Away from the wall, the value of the function is zero, which activates the k - ϵ formulation. Furthermore, in the low Reynolds number SST model the definition of turbulent viscosity is modified to account the turbulent shear stress transport.

The original k - ω model is given by:

$$\frac{D\rho k}{Dt} = \tau_{ij} \frac{\partial \bar{u}_i}{\partial x_j} - \beta^* \rho k \omega + \frac{\partial}{\partial x_j} \left[(\mu + \sigma_{k1} \mu_t) \frac{\partial k}{\partial x_j} \right] \quad (2-8)$$

$$\frac{D\rho \omega}{Dt} = \frac{\gamma_1}{\nu_t} \tau_{ij} \frac{\partial \bar{u}_i}{\partial x_j} - \beta_1 \rho \omega^2 + \frac{\partial}{\partial x_j} \left[(\mu + \sigma_{\omega 1} \mu_t) \frac{\partial \omega}{\partial x_j} \right] \quad (2-9)$$

The modified k - ϵ model is given by:

$$\frac{D\rho k}{Dt} = \tau_{ij} \frac{\partial \bar{u}_i}{\partial x_j} - \beta^* \rho k \omega + \frac{\partial}{\partial x_j} \left[(\mu + \sigma_{k2} \mu_t) \frac{\partial k}{\partial x_j} \right] \quad (2-10)$$

$$\frac{D\rho \omega}{Dt} = \frac{\gamma_2}{\nu_t} \tau_{ij} \frac{\partial \bar{u}_i}{\partial x_j} - \beta_2 \rho \omega^2 + \frac{\partial}{\partial x_j} \left[(\mu + \sigma_{\omega 2} \mu_t) \frac{\partial \omega}{\partial x_j} \right] + 2\rho \sigma_{\omega 2} \frac{1}{\omega} \frac{\partial k}{\partial x_j} \frac{\partial \omega}{\partial t} \quad (2-11)$$

In order to obtain the shear stress formulation, the transport equations corresponding to the original k - ω formulation, (2-8) and (2-9), are multiplied by a blending function F_1 , while the equation (2-10) and (2-11) are multiplied by $(1-F_1)$ and the corresponding equations are summed up.

The new model obtained as a consequence of above transformation is represented by the following set of equations:

$$\frac{D\rho k}{Dt} = \tau_{ij} \frac{\partial \bar{u}_i}{\partial x_j} - \beta^* k \rho \omega + \frac{\partial}{\partial x_j} \left[(\mu + \sigma_k \mu_t) \frac{\partial k}{\partial x_j} \right] \quad (2-12)$$

$$\frac{D\rho\omega}{Dt} = \frac{\gamma}{\nu_t} \tau_{ij} \frac{\partial \bar{u}_i}{\partial x_j} - \beta\rho\omega^2 + \frac{\partial}{\partial x_j} \left[(\mu + \sigma_\omega \mu_t) \frac{\partial \omega}{\partial x_j} \right] + 2\rho(1 - F_1)\sigma_\omega \frac{1}{\omega} \frac{\partial k}{\partial x_j} \frac{\partial \omega}{\partial x_j} \quad (2-13)$$

Any constant, ϕ is a blend of inner and outer constants, and is given by $\phi = F_1\phi_1 + (1 - F_2)\phi_2$. Furthermore, the turbulent eddy viscosity for the model is computed from

$$\nu_t = \frac{a_1 k}{\max(a_1 \omega, \Omega F_2)} \quad (2-14)$$

with a_1 being a constant, Ω being the absolute vorticity and F_2 is a function that takes a value of zero for the free shear flows and one for boundary layer flows.

The constants used in the k - ω -SST model are:

Inner constants (SST inner)

$$\beta^* = \frac{9}{100}, \sigma_{\omega 1} = 0.5, \beta_1 = 0.0750, a_1 = 0.31, \sigma_{k1} = 0.85, k = 0.41$$

Outer constants (standard k - ϵ)

$$\beta^* = \frac{9}{100}, \sigma_{\omega 2} = 0.856, \beta_2 = 0.0828, \sigma_{k2} = 1, k = 0.41$$

In addition to the above constants, the following auxiliary relations are used in the model formulation:

$$F_1 = \tanh \left\{ \left[\min \left[\max \left(\frac{\sqrt{k}}{\beta^* \omega y}, \frac{500\nu}{y^2 \omega}, \frac{4\sigma_{\omega 2} k}{CD_{k\omega} y^2} \right) \right]^4 \right] \right\} \quad (2-15)$$

$$CD_{k\omega} = \max \left(2\rho\sigma_{\omega 2} \frac{1}{\omega} \frac{\partial k}{\partial x_j} \frac{\partial \omega}{\partial x_j}, 10^{-20} \right) \quad (2-16)$$

$$F_2 = \tanh \left\{ \left[\max \left(\frac{2\sqrt{k}}{\beta^* \omega y}, \frac{500\nu}{y^2 \omega} \right) \right]^2 \right\} \quad (2-17)$$

$$\gamma_1 = \frac{\beta_1}{\beta^*} - \frac{\sigma_{\omega 1} k^2}{\sqrt{\beta^*}} \quad (2-18)$$

$$\gamma_2 = \frac{\beta_2}{\beta^*} - \frac{\sigma_{\omega 2} k^2}{\sqrt{\beta^*}} \quad (2-19)$$

2-2 Boundary Layer Transition and Transition Modeling

The prediction of boundary layer transition is an aspect in the development of computational fluid dynamics [14]. Transition can be defined as the change in state of a laminar boundary layer to turbulent. As mentioned in section 1-3, boundary layer flow over different objects may transition through different mechanisms in different applications. Despite the availability of a gamut of the turbulence models that allow a precise simulation of fully turbulent flows,

not many CFD compatible models are available to predict the aspect of laminar to turbulent transition.

Transitional boundary layer flows are important in many applications of engineering interests, such as turbine blades, aircraft wings, ship hulls, etc. Thus, modeling of transitional flows becomes a critical and integral aspect of computational fluid dynamics. The $\gamma-Re_{\theta t}$ transition model formulated by Menter *et al.* [14] provides a generic infrastructure that allows the coupling of the general purpose CFD with experimental transition data. A detailed description about the model is provided in the subsequent literature.

2-2-1 $\gamma-Re_{\theta t}$ Transition Model

The transition model as formulated by Menter *et al.* [14] consists of two components. The first is a universal framework provided by two transport equations that allow experimental data to be linked with the CFD code. The second integral component consists of the correlations. The model formulation involves two transport equations: an equation for intermittency (γ) and a second transport equation which is solved in terms of transition onset momentum-thickness Reynolds number ($\overline{Re_{\theta t}}$). In this work, the transport equation formulation is described in five parts. First part deals with the description about the intermittency transport equation. The second part pertains to the transport equation for the transition onset momentum thickness Reynolds number. The part section explains the modification that is used to improve the separated flow transition prediction. The fourth part gives a brief overview of the correlations that are employed along with the model. Lastly, the fifth part provides a link between the transition model and SST model.

Transport equation for intermittency

The transport equation for intermittency is used to trigger the transition locally. In the current model formulation, the intermittency function is coupled with $k-\omega$ SST model [14]. The transport equation essentially is used to activate the production term of turbulent kinetic energy downstream of the transition point in the boundary layer.

The intermittency equation is formulated as follows:

$$\frac{\partial}{\partial t}(\rho\gamma) + \frac{\partial}{\partial x_j}(\rho\bar{u}_j\gamma) = P_\gamma - E_\gamma + \frac{\partial}{\partial x_j} \left[\left(\mu + \frac{\mu_t}{\sigma_f} \right) \frac{\partial \gamma}{\partial x_j} \right] \quad (2-20)$$

The following equation describes the source term for transition:

$$P_{\gamma 1} = F_{length} \cdot c_{a1} \rho S \cdot \sqrt{\gamma F_{onset}} \cdot (1 - \gamma) \quad (2-21)$$

where, S is the strain rate magnitude. The transition source term is devised to be zero in the laminar boundary layer, upstream of the transition point and is active wherever the value of local strain rate Reynolds number exceeds the local transition onset criterion. The magnitude of the source term is controlled by transition length function i.e. F_{length} . This term governs the length of the transition region. The source term limits the value of intermittency, so that it does not exceed unity.

The F_{onset} function is used to trigger the intermittency production in the equation (2-21). This function is designed to change from the value of zero in the laminar boundary layer to a value of one downstream of the transition onset location. F_{onset} is a function of the turbulent Reynolds number (Re_T) and the local strain rate Reynolds number and is expressed as:

$$F_{onset1} = \frac{Re_v}{2.193Re_{\theta c}} \quad (2-22)$$

$$F_{onset2} = \min(\max(F_{onset1}, F_{onset1}^4), 2.0) \quad (2-23)$$

$$F_{onset3} = \max\left(1 - \left(\frac{Re_T}{2.5}\right)^3, 0\right) \quad (2-24)$$

$$F_{onset} = \max(F_{onset2} - F_{onset3}, 0) \quad (2-25)$$

where, $Re_v = \frac{\rho y^2 S}{\mu}$ and $Re_T = \frac{\rho k}{\mu \omega}$

$Re_{\theta c}$ in the equation (2-22) is defined as the critical Reynolds number where the intermittency first increases in the boundary layer. This happens upstream of the transition Reynolds number ($Re_{\theta t}$). There is a delay because turbulence must increase to a substantial level before laminar profile shows a change. Thus, $Re_{\theta c}$ can be considered as a location where turbulence starts to grow, while $Re_{\theta t}$ can be considered as the location where a deviation from the laminar velocity profile occurs. The relation between these two is obtained from empirical correlations where, $Re_{\theta c} = f(\overline{Re_{\theta t}})$. $\overline{Re_{\theta t}}$ is obtained from the transport equation (2-2).

Furthermore, the destruction/relaminarization term (E_γ) in equation (2-20) acts as a sink term. The term ensures that the intermittency remains close to zero in the laminar boundary layer and also enables the model to predict relaminarization. The term is defined by the following equation:

$$E_\gamma = \rho c_{a2} \Omega \gamma \cdot F_{turb} \cdot (\gamma c_{e2} - 1) \quad (2-26)$$

where, Ω is the vorticity magnitude, c_{a2} is a constant that controls the strength of the destruction term and ensures that the entire term is smaller than the transition source term. The constant c_{e2} controls the lower limit of intermittency where the term changes sign [14].

In order to disable the destruction/relaminarization source term in-case of a fully turbulent regime, F_{turb} is used. This term is defined as :

$$F_{turb} = e^{-\left(\frac{Re_T}{4}\right)^4} \quad (2-27)$$

For intermittency (γ), the boundary condition at the wall is zero normal flux. At the inlet, γ is assigned a value 1. The constants for intermittency equations are:

$$c_{a1}=2.0; \quad c_{e2}=50; \quad c_{a2}=0.06; \quad \sigma_f=1.0;$$

The subsequent section describes the formulation of the transportation equation for the transition momentum thickness Reynolds number used in the transition model formulation. The equation forms an integral part of the model as it ties the empirical correlations to the onset criterion defined in the intermittency equation.

Transport equation for transition onset momentum thickness Reynolds number

The second transport equation in the model formulation is solved in terms of the transition onset momentum thickness Reynolds number ($Re_{\theta t}$). This equation is required to capture the non-local influence of turbulence intensity, which changes as a consequence of decay of turbulent kinetic energy in the free stream and also due to the changes in free stream velocity outside the boundary layer [14].

The transport equation for the transition momentum thickness Reynolds number is given by:

$$\frac{\partial}{\partial t}(\rho \overline{Re_{\theta t}}) + \frac{\partial}{\partial x_j}(\rho \bar{u}_j \overline{Re_{\theta t}}) = P_{\theta t} + \frac{\partial}{\partial x_j} \left[\sigma_{\theta t} (\mu + \mu_t) \frac{\partial \overline{Re_{\theta t}}}{\partial x_j} \right] \quad (2-28)$$

where, $P_{\theta t}$ is the production term and is defined by the equation:

$$P_{\theta t} = c_{\theta t} \cdot \frac{\rho}{t} \cdot (Re_{\theta t} - \overline{Re_{\theta t}}) \cdot (1 - F_{\theta t}) \quad (2-29)$$

where $t = \frac{500\mu}{\rho \bar{u}^2}$, is a time scale. The blending function $F_{\theta t}$ in the above equation is used to deactivate the production term in the boundary layer. The blending function is assigned a value of one in the boundary layer and zero in the free stream.

The production term is designed to force the transported scalar ($\overline{Re_{\theta t}}$) to match the local value of $Re_{\theta t}$ outside the boundary layer. The local value of $Re_{\theta t}$ is computed from empirical correlation [14].

The blending function ($F_{\theta t}$) is given by the following set of equation

$$F_{\theta t} = \min \left(\max \left(F_{wake} \cdot e^{-\left(\frac{y}{\delta}\right)^4}, 1.0 - \left(\frac{\gamma - \frac{1}{C_{e2}}}{1 - \frac{1}{C_{e2}}} \right)^2 \right), 1.0 \right) \quad (2-30)$$

$$\theta_{BL} = \frac{\overline{Re_{\theta t}} \mu}{\rho \bar{u}} \quad \delta_{BL} = \frac{15}{2} \theta_{BL} \quad \delta = \frac{50\omega y}{\bar{u}} \delta_{BL} \quad (2-31)$$

$$Re_{\omega} = \frac{\rho \omega y^2}{\mu} \quad (2-32)$$

$$F_{wake} = e^{-\left(\frac{Re_{\omega}}{10^{-5}}\right)^2} \quad (2-33)$$

The function F_{wake} is used to ensure that the blending function is not activated in the wake regions of a blade or an aerofoil. $c_{\theta t}$ and $\sigma_{\theta t}$ are the model constants, where $c_{\theta t} = 0.03$ controls the magnitude of source term and $\sigma_{\theta t} = 2.0$ controls the diffusion coefficient.

Separated Flow Prediction

For the laminar boundary layer separation, the model formulation discussed above predicts the turbulent reattachment at a downstream location. In order to improve this inaccuracy, a modification is proposed by to the transition model that allows turbulent kinetic energy to grow rapidly once the laminar boundary layer separates [14]. The modification has negligible effect on the prediction for attached transition or fully turbulent flow. The modification is incorporated into the blending function, $F_{\theta t}$ from the transport equation for momentum thickness Reynolds number (2-28). The following modification is introduced into the model,

$$\gamma_{sep} = \min \left(s_1 \max \left[0, \left(\frac{Re_\nu}{3.235 Re_{\theta c}} \right) - 1 \right] F_{reattach}, 2 \right) F_{\theta t} \quad (2-34)$$

$$F_{reattach} = e^{-\left(\frac{Re_T}{20}\right)^4} \quad (2-35)$$

$$\gamma_{eff} = \max(\gamma, \gamma_{sep}) \quad (2-36)$$

where, $s_1 = 2$

The basic point behind the above formulation is to allow the local intermittancy value to exceed above one whenever laminar boundary layer separation occurs. This causes a sudden increment in the production of turbulent kinetic energy (k) which in turn affects earlier transition. As seen in equation (2-34), this is achieved when the strain rate Reynolds number (Re_ν) exceeds the critical momentum thickness Reynolds number ($Re_{\theta c}$).

In the modified equation (2-34) for separated flow prediction, the constant s_1 controls the size of the separation bubble. Furthermore, once the viscosity ratio is large enough to cause reattachment, the function $F_{reattach}$ deactivates the modification.

Model Correlations

In the γ - $Re_{\theta t}$ transition model formulation, three empirical correlations are defined for $Re_{\theta t}$, F_{length} and $Re_{\theta c}$. $Re_{\theta t}$ is used in equation 2-2 and establishes the transition onset. While F_{length} is used in equation (2-2) and defines the length of the transition region, $Re_{\theta c}$ forms the point where the transition model is activated. F_{length} is also a function of $\overline{Re}_{\theta t}$ and is given by the following correlation:

$$F_{length} = \begin{cases} 398.189 \cdot 10^{-1} + (-119.270 \cdot 10^{-4})\overline{Re}_{\theta t} + (-132.567 \cdot 10^{-6})\overline{Re}_{\theta t}^2, & \overline{Re}_{\theta t} < 400 \\ 263.404 + (-123.939 \cdot 10^{-2})\overline{Re}_{\theta t} + (194.548 \cdot 10^{-5})\overline{Re}_{\theta t}^2 \\ + (-101.695 \cdot 10^{-8})\overline{Re}_{\theta t}^3, & 400 \leq \overline{Re}_{\theta t} < 596 \\ 0.5 - (\overline{Re}_{\theta t} - 596.00) \cdot 3.0 \cdot 10^{-4}, & 596 \leq \overline{Re}_{\theta t} < 1200 \\ 0.3188, & \overline{Re}_{\theta t} \geq 1200 \end{cases}$$

As mentioned in Subsection (2-2-1), $Re_{\theta c}$ is a function of transition momentum thickness Reynolds number ($\overline{Re}_{\theta t}$). The exact relation between the two is given by the following empirical correlation:

$$Re_{\theta c} = \begin{cases} (-369.035 \cdot 10^{-2})\overline{Re}_{\theta t} + (120.656 \cdot 10^{-4})\overline{Re}_{\theta t} + (868.230 \cdot 10^{-6})\overline{Re}_{\theta t}^2 \\ + (-696.506 \cdot 10^{-9})\overline{Re}_{\theta t}^3 + (174.105 \cdot 10^{-12})\overline{Re}_{\theta t}^4, & \overline{Re}_{\theta t} \leq 1870 \\ \overline{Re}_{\theta t} - (593.11 + (\overline{Re}_{\theta t} - 1870) \cdot 0.482), & \overline{Re}_{\theta t} > 1870 \end{cases}$$

Lastly, $Re_{\theta t}$ is also a function of the turbulence intensity (Tu), Thwaite's pressure gradient coefficient λ_{θ} and flow acceleration parameter (K) [16]. The following empirical correlation defines the relation between these quantities:

$Re_{\theta t} = 803.73[Tu + 0.6067]^{-1.027}F(\lambda_{\theta}, K)$ where,

$$F(\lambda_{\theta}, K) = \begin{cases} 1 - (-10.32\lambda_{\theta} - 89.47\lambda_{\theta}^2 - 265.51\lambda_{\theta}^3)e^{(-Tu/3.0)}, & \lambda_{\theta} \leq 0 \\ 1 + (0.0962(K10^6) + 0.148(K10^6)^2 + 0.0141(K10^6)^3) \\ \cdot (1 - e^{(-Tu/1.5)}) + 0.556(1 - e^{(-23.9\lambda_{\theta})})e^{(-Tu/1.5)}, & \lambda_{\theta} > 0 \end{cases}$$

where, Tu is the local turbulence intensity and is defined as $Tu = 100\frac{\sqrt{2k/3}}{U}$ and λ_{θ} is the pressure gradient coefficient and is given as $\lambda_{\theta} = \frac{\rho\theta}{\mu} \frac{dU}{ds}$.

Coupling with the SST model

The transition model is coupled to the SST turbulence model by making use of the effective intermittency defined in equation 2-2-1. The production and dissipation terms in the k equation are modified as follows:

$$\overline{P}_k = \gamma_{eff}P_k \quad (2-37)$$

$$\overline{D}_k = \min(\max(\gamma_{eff}, 0.1), 1.0)D_k \quad (2-38)$$

where P_k and D_k are the production and destruction terms from the turbulent kinetic energy equation in the original SST turbulence model and γ_{eff} is the effective intermittency obtained from the transition formulation.

Another modification incorporated into the SST turbulence model includes a change in the blending function F_1 . The blending function F_1 is redefined such that it always remains equal to 1 in laminar boundary layer. The modified blending function is given as:

$$R_y = \frac{\rho y \sqrt{k}}{\mu} \quad (2-39)$$

$$F_3 = e^{-\left(\frac{R_y}{120}\right)^8} \quad (2-40)$$

$$F_1 = \max(F_{1,orig}, F_3) \quad (2-41)$$

where, $F_{1,orig}$ is the original blending function employed in the SST model.

2-3 Effect of Surface Roughness on Turbulent Flow Fields

The wall bounded flow is considered to be composed of an inner layer and an outer layer. The inner layer is defined as the region where the mean velocity profile is determined by the viscous scales and is independent of the flow length scale and bulk velocity. In case of a wall bounded channel flow the viscous scales are defined as- friction Reynolds number, $Re_\tau = \frac{u_\tau \delta}{\nu}$ and viscous length scale $\delta_v = \frac{\nu}{u_\tau}$. In case of the outer layer, the direct effect of the viscosity on the mean velocity profile is assumed to be negligible.

In general, for near wall turbulent flow theories, postulate an velocity profile characterized by a overlap region where the mean flow is given by [30]:

$$u^+ = \frac{1}{k} \ln(y^+) + B \quad (2-42)$$

where $u^+ = \bar{u}/u_\tau$, $y_+ = y/\delta_v$ and B is a constant.

However, in presence of roughness, particularly when the scale (s) of the roughness element is large compared to the viscous scale δ_v , the local Reynolds number of the flow over the roughness elements is large. The transfer of momentum from the fluid to the wall is accomplished by drag on roughness elements, which at high Reynolds number is predominantly due to pressure forces rather than viscous stresses [28]. In such cases the velocity profile in the overlap region is modified as;

$$u^+ = \frac{1}{k} \ln\left(\frac{y}{s}\right) + B\left(\frac{s}{\delta_v}\right) \quad (2-43)$$

In case of a fully rough wall bounded pipe flow the constant B takes a value of 8.5.

The difference between the mean velocity profile on a smooth surface and rough surface is given by the following equation [30]:

$$\Delta u^+ = \frac{1}{k} \ln\left(\frac{s}{\delta_v}\right) - 3.5 \quad (2-44)$$

Δu^+ represents the shift in the velocity profile as shown in figure 2-1.

Furthermore, in case of a boundary layer the mean velocity profile is given by the equation:

$$u^+ = \frac{1}{k} \ln y^+ + B - \Delta u^+ \frac{2\pi}{k} w\left(\frac{y}{\delta}\right) \quad (2-45)$$

The above equation consists of the overlap region profile, the roughness shift Δu^+ and the wake function $w(y/\delta)$. The parameter π in the equation (2-45) is defined as the wake strength parameter and its value is flow dependent. While δ in the above equation is the boundary layer thickness. The mean velocity profile can be more conveniently described in terms of its deviation from the value at the edge of the boundary layer, i.e at $y = \delta$,

$$u_e^+ - u^+ = \frac{2\pi}{k} \left[w(1) - w\left(\frac{y}{\delta}\right) \right] - \frac{1}{k} \ln\left(\frac{y}{\delta}\right) \quad (2-46)$$

The mean velocity defect is dependent on two parameters for a given wake function- wake strength parameter (π) and the friction velocity (u_τ). Both these parameters are influenced by the surface roughness.

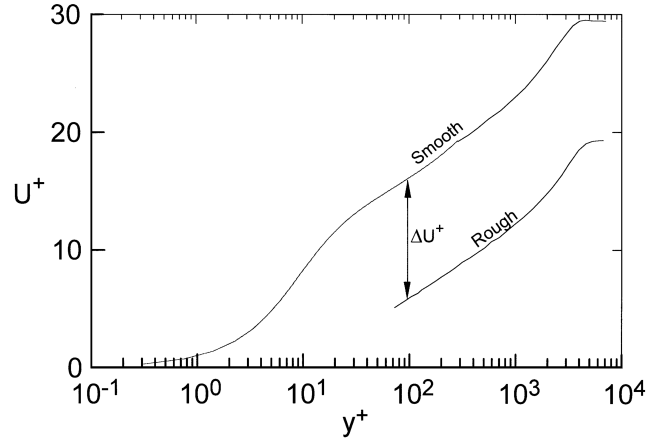


Figure 2-1: Typical mean velocity distributions, normalized using wall variables, over smooth and rough walls [2]

2-4 Admissible Roughness

The admissible roughness can be defined as the maximum height of the individual roughness elements which causes no increase in the drag as compared to a smooth wall [22]. As mentioned in the previous chapter, in case of turbulent boundary layers, surface roughness has no effect and the wall can be considered as hydraulically smooth, if the maximum height of the roughness elements lies within the laminar sublayer. In case of a pipe flow the value of the non dimensional parameter determines whether the wall is hydraulically smooth. In general, if the non dimensional parameter, $k^+ = \frac{\nu_* k_s}{\nu} < 5$, the wall can be considered as hydraulically smooth.

The above correlations can also be considered for a flat plate. For a flat plate however, the following correlation can be used to estimate the admissible value of surface roughness [22]:

$$k_{adm} \leq 100 \frac{\nu}{U_\infty} \quad (2-47)$$

where U_∞ is the free stream velocity.

The above equation provides one value for the admissible roughness for the whole plate. But, as the boundary layer thickness is smaller near the leading edge, the admissible value of the roughness should be smaller near the leading edge as compared to the trailing edge. This is taken into account by modifying the above equation (2-47) and introducing the local skin friction coefficient (c'_f). The modified equation is given as :

$$\frac{U_\infty k_{adm}}{\nu} < \frac{7}{\sqrt{c'_f}} \quad (2-48)$$

However, for practical applications the admissible value of roughness is directly related to the length of the body (l), under consideration [22]. To achieve this the equation (2-47) is written as:

$$k_{adm} \leq l \frac{100}{Re_l} \quad (2-49)$$

where, $R_l = \frac{U_\infty l}{\nu}$

The height of the roughness element that causes a transition in a laminar boundary layer is called critical height or critical roughness [22]. Surface roughness affects the resistance offered by the wall by causing the transition point to move upstream. This causes the drag to increase or decrease depending upon the shape of the body under consideration. In general, the drag may be increased by such a shift in the transition point when the drag is due to the skin friction, while it may be decreased when the drag of the body is due to form drag [22]

The critical value of roughness is defined by [51]:

$$\frac{v_* k_{crit}}{\nu} = 15 \quad (2-50)$$

Validation Cases

In the current chapter, the ability of the transition model available in ANSYS CFX to predict onset of the transition is validated for different 2D test cases and their results have been elaborated. The first test case involves modeling of flow over an adiabatic flat plate [31]. This is followed validating the results on flow over a flat plate with a distributed surface roughness [32] and a plate with imposed pressure gradient [27]. The above cases are performed in order to understand the implementation of the transition model and its ability to capture roughness induced transition. Finally, a turbo-machinery test case has been evaluated wherein the variation of heat transfer coefficient and skin friction coefficient over a VKI transonic guide vane [3,33] has been modeled and validated.

3-1 Flat Plate

In order to investigate the capability of the transition model available in ANSYS CFX, three test cases have been simulated for the flat plate study. The first test case corresponds to the flow over a smooth flat plate. The second test case involves the study of flow over a roughened flat plate. This study has been carried out to investigate the capability of the commercial CFD software to capture the effects of surface roughness on boundary layer transition. Finally, the loss coefficients have been evaluated for the flow over a flat plate with imposed pressure gradient and surface trips.

3-1-1 Smooth Flat Plate

The purpose of this test case is to compare the prediction of the transition ($\gamma - Re_\theta$) model formulation available in ANSYS CFX with the experimental results available for subsonic flow over a smooth flat plate. The flow conditions compare with the test case T3A, documented by Savill [31]. The boundary conditions for the test case are documented in Appendix A.

The computational grid is provided by Dr. Rene Pecnik and comprises of 5120 control volumes divided by a H-type grid which ensures a resolution of $y^+ < 0.3$ at the walls [3]. The results

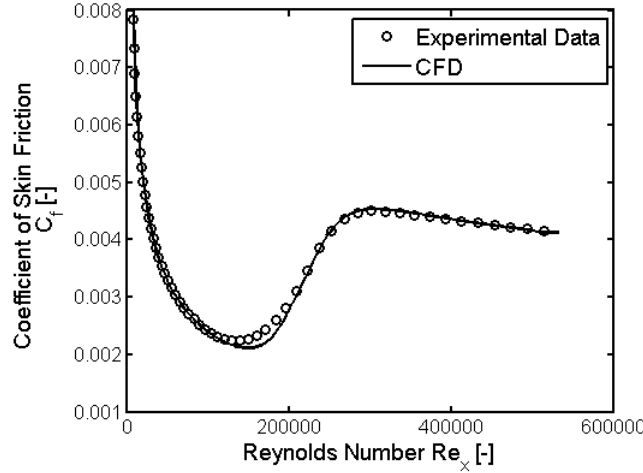


Figure 3-1: Variation of skin friction coefficient with Reynolds number for a smooth flat plate

obtained are presented in terms of the distribution of the skin friction coefficient c_f over the plate surface as depicted in Fig. 3-1. The skin friction coefficient is defined as

$$C_f = \frac{\tau_w}{0.5 * \rho_\infty * U_\infty^2} \quad (3-1)$$

where $\tau_w = \mu \frac{dU}{dy}$ is the wall shear stress, U_∞ and ρ_∞ are the freestream density and velocity, respectively.

The figure 3-1 depicts a sudden increase in the skin friction coefficient for a certain range of Reynolds number ($Re_x=150000$ to 270000). This corresponds to the transition from laminar flow regime. Furthermore, the results obtained from CFD solver are in a close agreement with the experiments which justifies the capability of the model to predict transition onset.

3-1-2 Roughened Flat Plate

In the present section, the results of a two dimensional flow over a roughened flat plate are presented. The motivation behind this test was to determine the capability of the transition model available in CFX to model roughness induced transition.

The test case corresponds to the work of Dassler *et.al* [32]. The computational domain consists of 5120 elements and provides an average $y^+ \approx 0.95$ at the wall. To validate the case, a sand grain roughness height of 30 microns has been applied to the flat plate. The corresponding flow conditions and boundary condition are documented in Appendix A.

In their, work Dassler *et.al* [32] have equivalent surface roughness (k_s) as the measure of the roughness at the surface. However, since the transition model formulation in CFX also requires the specification of the geometric roughness height the following correlation as mentioned in their work [32] has been used:

$$k_s = 4.433k \quad (3-2)$$

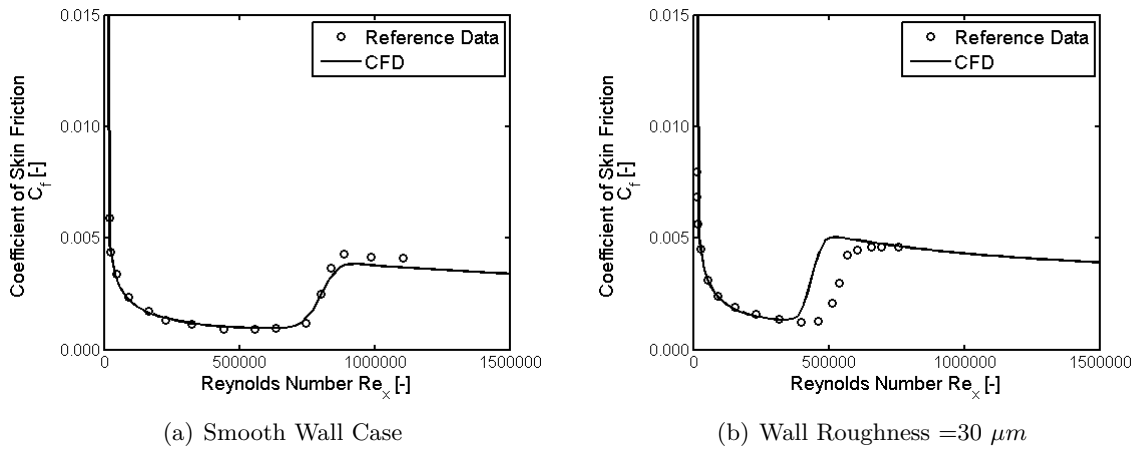


Figure 3-2: Variation of skin friction coefficient with Reynolds Number for a rough flat plate

Fig.3-2 shows the comparison between the skin friction coefficient obtained from the current simulations and the simulation results documented in the work of Dassler *et.al* [32]. It can be seen that the presence of roughness causes a shift in the transition location. The transition onset location shifts from $Re_x=750000$ to $Re_x=385000$. The simulations carried out in the current work agree reasonably well for the smooth case, as depicted in Fig. 3-2(b). However, in the case of the roughened flat (Fig. 3-2(a)) the simulations predict an early transition and reattachment as compared with the baseline reference case. This deviation can be attributed to the approximate correlation used to relate the equivalent surface roughness height to the geometric roughness height for the roughness elements. It can be inferred that the presence of surface roughness results in an earlier transition.

The results obtained in this section are in agreement with the simulation results of the reference case [32] and shows the influence of the surface roughness to cause the transition from laminar to turbulent flow regime at a lower Reynolds Number. Thus, this gives a validation to the ability of the model in CFX to predict roughness induced transition.

3-1-3 Flat Plat with Imposed Pressure Gradient

In the current test case, the effect of surface trips on the boundary layer development on an ultra-high-lift low pressure LP turbine blade is considered. The objective of the study is to model the capability of the CFD solver to predict transition under the combined effect of the surface roughness and adverse pressure gradients encountered in typical turbomachinery applications. The parametric study is conducted on a flat plate with the same surface pressure distribution as encountered in case of a LP turbine blade. For this case, the experimental results of Zhang and Hodson [27] have been validated.

To obtain the same surface distributions on the flat plate as encountered on the suction side of the LP turbine blade, the geometry for the upper-wall of the simulation domain is obtained using the experimental results of the inviscid coefficient of pressure distribution over the test plate. This is done using the Bernoulli's equation for incompressible fluid. The computational

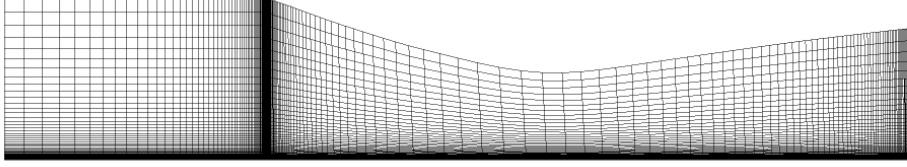


Figure 3-3: Computational domain for flat plate with imposed pressure gradient

Table 3-1: Surface trip parameters

S No	Roughness Height k(mm)	Normalized Height k/S_O (%)
1	1.20	0.24
2	0.81	0.86
3	0.74	0.15
4	0.68	0.14
5	0.61	0.12

domain consists of 18000 elements and the domain for the current test case is presented in Fig. 3-3 .

Fig.3-4 shows the comparison between the experiments and simulated coefficient of pressure (C_p) distribution for the in-viscid and the turbulent case. It can be seen that the simulated results for the surface distribution of the coefficient of pressure agrees reasonably well with the experimental results. This validates the computed domain geometry.

C_p is defined by the following equation:

$$C_p = \frac{P_{01} - P_s}{P_{01} - P_{s2}} \quad (3-3)$$

where P_{01} is the inlet total pressure, P_{s2} is the exit static pressure and P_s is the measured static pressure. The roughness height directly affects the boundary layer development and therefore the profile loss. To study the effects of the roughness heights on the profile loss, different roughness magnitudes have been considered at 50% of the plate length. Table 3-1 summarizes the parameters of the surface trips used in the parametric study on the flat plate.

The profile loss coefficient (ϵ) is defined as:

$$\epsilon = \frac{2\theta}{s \cdot \cos(\alpha_2)} \quad (3-4)$$

where θ is the trailing edge momentum thickness, s is the equivalent pitch of pressure distribution under investigation and α_2 is the exit flow angle and takes a value of 63.2° . The parameters associated with the test case are documented in Appendix A.

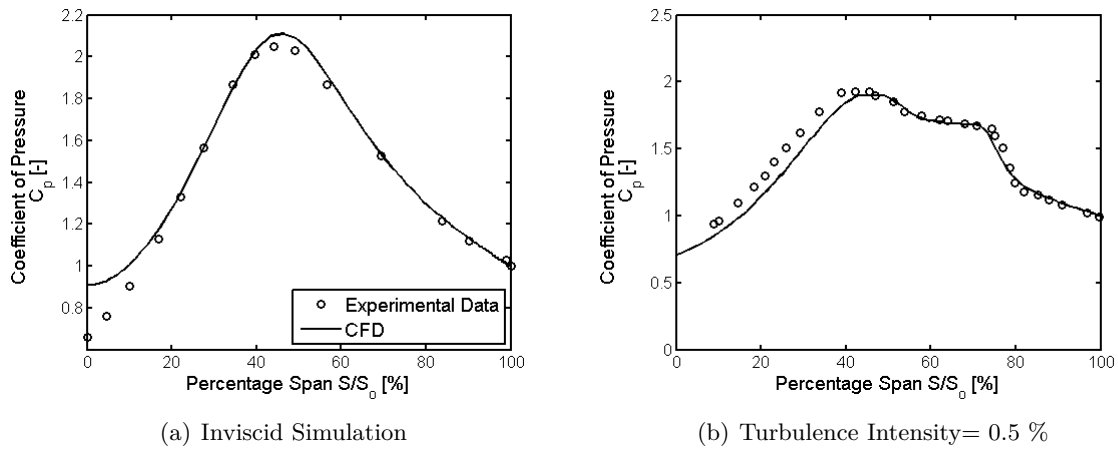


Figure 3-4: Comparison of surface static pressure distribution carried out to validate the computed domain geometry

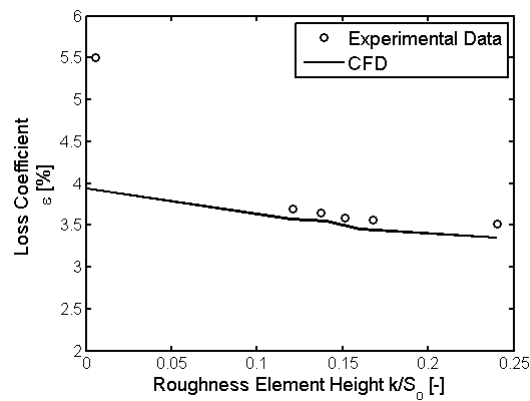


Figure 3-5: Effect of trip height on losses at $Tu=0.5\%$

The effect of surface trip height on the profile losses at $Re=174000$ and $Tu=0.5\%$ is shown in Fig. 3-5. It can be seen that the experimental data and the simulated results agree reasonably well for the rough regime. However, for the smooth case, the CFD simulations under-predict the loss coefficient. As a result of the separation bubble, the loss coefficients are higher in the smooth case. The addition of the surface trips reduces the profile loss. Furthermore, the losses continue to decrease as the heights of the surface elements increases. Fig. 3-6 presents the variation of C_p along the blade surface. As a result of the adverse pressure gradient, the boundary layer separates at a plate length of 0.35 mm for the smooth case and reattaches at a length of 0.39 mm. The addition of the surface roughness causes the transition location to shift upstream and also causes an early reattachment.

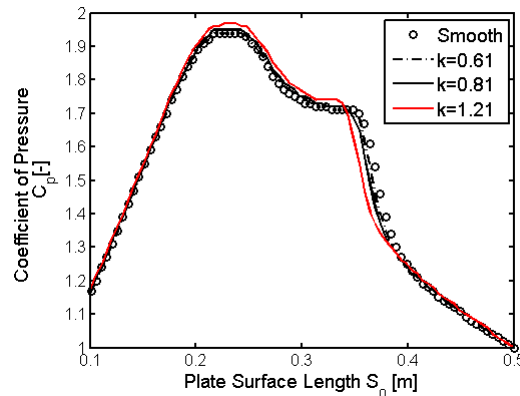


Figure 3-6: Coefficient of pressure distribution along the plate length

3-2 Von Karman Institute Transonic Turbine Guide Vane

In this test case, computational aero-thermal validation of flow characteristics around a highly loaded transonic turbine nozzle guide vane has been performed. The experimental data for the validation corresponds to the measurements made by Arts [33] in the compression tube facility. The experimental work involved the detailed analysis of the effect of free-stream Mach and Reynolds numbers as well as turbulence intensity on the aerodynamic and heat transfer over the turbine blade.

For the current computational analysis a finite volume method based fluid flow solver ANSYS CFX has been used. The computational domain for the current work has been provided by Dr. Rene Pecnik. The domain consists of 50728 elements and provides a resolution of $y_+ < 1$ at the first cell row close to the blade surface [3]. The important geometric parameters of the turbine cascade are summarized in the table 3-2. Fig. 3-7 shows the computational mesh along with the imposed boundary condition used for the numerical simulations of the VKI turbine blade. Pressure inlet boundary condition is imposed to define the fluid pressure at the inlet to the flow domain. The total pressure and total temperature is specified in accordance with the experimental data of Arts [33] to satisfy the flow calculations. At the outlet boundary condition, static pressure value is specified in accordance to the experimental case to represent the pressure outlet boundary condition. The suction and pressure surfaces are specified as isothermal wall. Furthermore, the pitch-wise boundary ends are imposed as periodic boundaries. Lastly, upper and lower side boundaries in the normal-wise direction have been specified as free slip walls.

The numerical simulations have been performed for two different flow cases corresponding to two different outlet- Reynolds number and Mach number. The corresponding flow conditions for the two test cases, namely MUR-235 and MUR-241, are documented in the table 3-3. Furthermore, the boundary conditions for the two test cases have been presented in Appendix A . For the current case in perspective, transitional model formulation in ANSYS CFX has been used.

The test case has been validated by comparing the heat transfer coefficient along the normalized curvilinear coordinates of the turbine blade obtained by the numerical simulations with the experimental data. The reference temperature for the simulation is prescribed as 420 K,

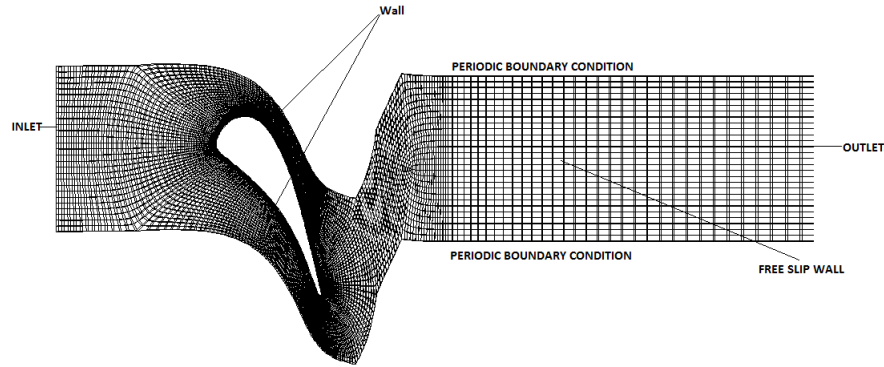


Figure 3-7: Computational mesh for VKI turbine guide vane

Table 3-2: VKI transonic blade geometric parameters

S No	Blade Geometric Parameter	Value
1	Blade Chord	12.5 mm
2	Inlet Flow Angle	37.3° [-]
3	Stagger Angle	59.3° [-]
4	Pitch to Chord	0.850 mm

corresponding to the value used by Arts [33] in the experiments while the blade surface is assumed to have a constant temperature of 298 K. The heat transfer coefficient (h) has been modeled as

$$h = \frac{q_w}{T_\infty - T_w} \quad (3-5)$$

where q_w is the wall heat flux, T_∞ is the reference fluid temperature and T_w is the prescribed wall temperature.

Figs. 3-8(a) and 3-8(b) show the distribution of the heat transfer coefficient along the normalized curvilinear coordinates for the VKI-MUR 235 and VKI-MUR 241 cases respectively. In the figures, the positive values of s/c correspond to the suction side while the negative

Table 3-3: Data pertaining to the VKI turbine guide vane test cases. $M_{is,out}$ and $Re_{c,out}$ are the outlet Reynolds number and Mach number based on the blades chord. Re_M is the Reynolds number based on the velocity and mesh spacing of the turbulence grid in the experimental arrangement, used to obtain specific dissipation rate ω [3]

Case	Tu[%]	$M_{is,out}$	$Re_{c,out}$	Re_M
MUR-235	6.0	0.927	1.15e6	61700
MUR-241	6.0	1.089	2.11e6	61700

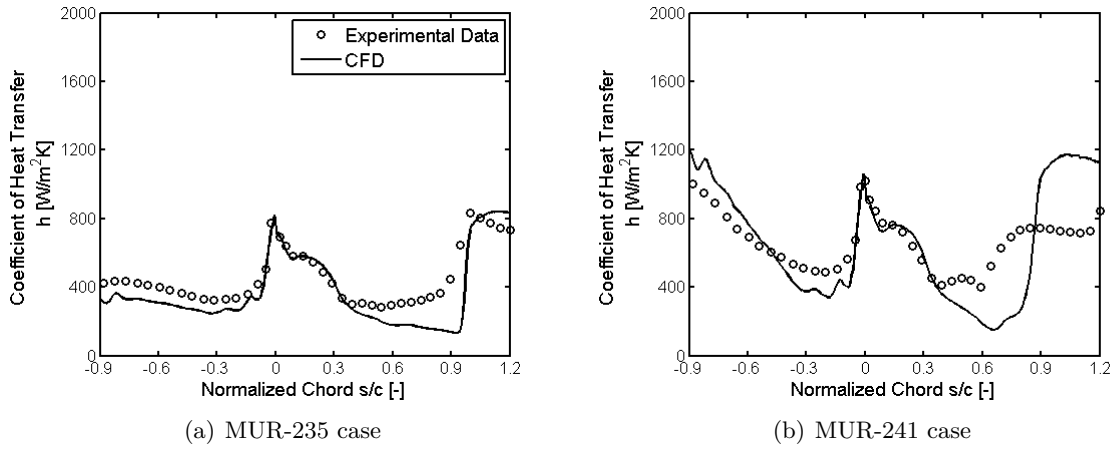


Figure 3-8: Distribution of heat transfer coefficient over the VKI blade profile.

values correspond to the pressure side of the blade. Both the experimental data and numerical simulation predict no transition at the pressure side of the blade. This is evident as a smooth variation in the heat transfer distribution can be observed along the curvilinear coordinates of the pressure side. While, for the suction side the experimental data reveals flow transition. The increase in the heat transfer coefficient at s/c 0.8 and 0.6 for MUR-235 and MUR-241 cases respectively shows the onset of laminar to turbulent transition at the suction side of the investigated blade. The computational model as seen in Fig. 3-8(a) and 3-8(b) predicts the transition over the suction side. However, there is a significant difference between the experimental transition location and computed transition location. This is attributed to the fact that in the $\gamma - Re_{\theta t}$ model the experimental correlations that affect the transition prediction and modeling are based on the experiments conducted over an incompressible flat plate. Furthermore, it can be observed that the numerical simulations under-predict the heat transfer coefficient along the suction side and the pressure side of the turbine blade.

The value of skin friction coefficient along the blade surface has been compared with the numerical results conducted by Raspopov [3]. Figs. 3-9(a) and 3-9(b) show the variation of the skin friction coefficient along the pressure side and suction side of the turbine blade for the two considered cases. The results obtained from the current simulations overpredict the skin friction as compared to the reference data for the MUR-235 case while an appreciable agreement is observed in case of the MUR-241 case. However, for both the cases the current simulations predict a delayed transition close to the trailing edge of the blade.

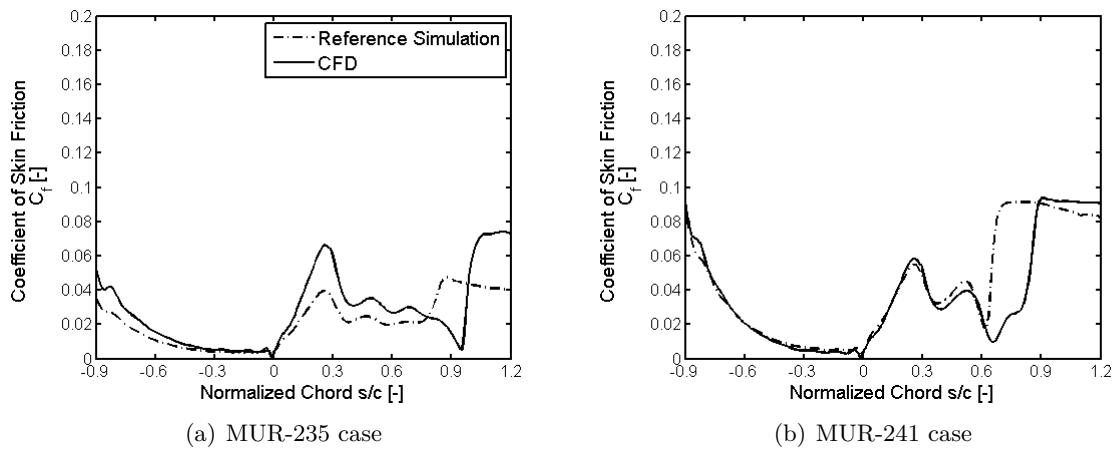


Figure 3-9: Skin friction distribution over the VKI blade profile.

Compressor Performance Evaluation

The previous chapter provides a validation to the ability of the transition model formulation available in CFX to accurately predict and model the transition onset. The current chapter presents the numerical study performed on the centrifugal compressor. The compressor has been adopted by the turbocharger developed by Mitsubishi Turbocharger and Engine Europe B.V. Steady state simulations have been performed using ANSYS CFX to approximate the unsteady flow field and the performance of the test compressor. The test compressor has been simulated in accordance with a defined set of procedures and detailed evaluation of the flow field, and performance has been made. The current analysis allowed to gain further insights about the compressor flow structure, performance and loss mechanisms. The chapter provides a detailed methodology employed for the compressor simulation and describes the outcome of the analysis.

Firstly, in Section 4-1, the geometric specification of the test compressor is provided. The compressor pre-processing and computational framework is described further in Section 4-2. Next, detailed performance analysis of the test compressor is presented in Section 4-3. Finally, the last Section 4-5, provides an overview of the phenomenon of flow instability evolution within the centrifugal compressor.

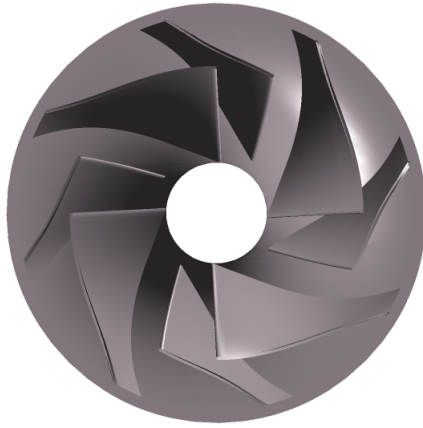
4-1 Compressor Specification

The test compressor for the current work is provided by Mitsubishi Turbocharger and Engine Europe B.V.(MTEE). The basic geometric parameters of the compressor are documented in Table A-1

The modeled compressor consists of a total of 8 blades (4 splitter blades and 4 main blades). The blades are leaned and have sufficient backsweep in the direction of impeller rotation. A vaneless diffuser with a front pinch forms an integral part of the compressor domain. An overhung volute with a 90⁰ bend at the outlet finally receives the flow and completes the compression stage.

Table 4-1: Compressor specification

S No	Compressor Domain	Parameter	Dimension
1	Impeller	Tip radius, r_2	20 mm.
		Inlet shroud radius, r_{1s}	12.5 mm
		Backsweep angle, β_{2B}	40°
2	Diffuser	Outlet Radius, r_5	12.5 mm
2	Volute	Outer diameter, d_7	38.4 mm



(a) Front view



(b) Side view

Figure 4-1: The modeled impeller geometry for the computational fluid dynamic analysis

4-2 Preprocessing and CFD Setup

In order to obtain a CFD model for the test compressor, a sequential procedure is adopted. This section presents the methodology adopted for development of a robust model for the numerical simulations. The model development involves steps such as the geometric parametrization, grid processing and solver setup. A detailed description of all the steps employed for the development of a robust model is presented in the subsequent literature.

4-2-1 Geometric Parametrization

The preliminary step in pre-processing is to obtain a precise geometric model of the compressor. For the current compressor under investigation, the compressor geometric data available in the casting and machine drawings have been transformed into a computer compatible 3D model using the modeling tool ANSYS Bladegen. The tool allows rapid definition of radial blade rows and renders an essential link between the blade design and advanced simulations (Fig.4-1).

For the current work, the inlet duct, the impeller and the vaneless diffuser have been modeled as a single domain. Only a single blade passage has been modeled for the impeller by

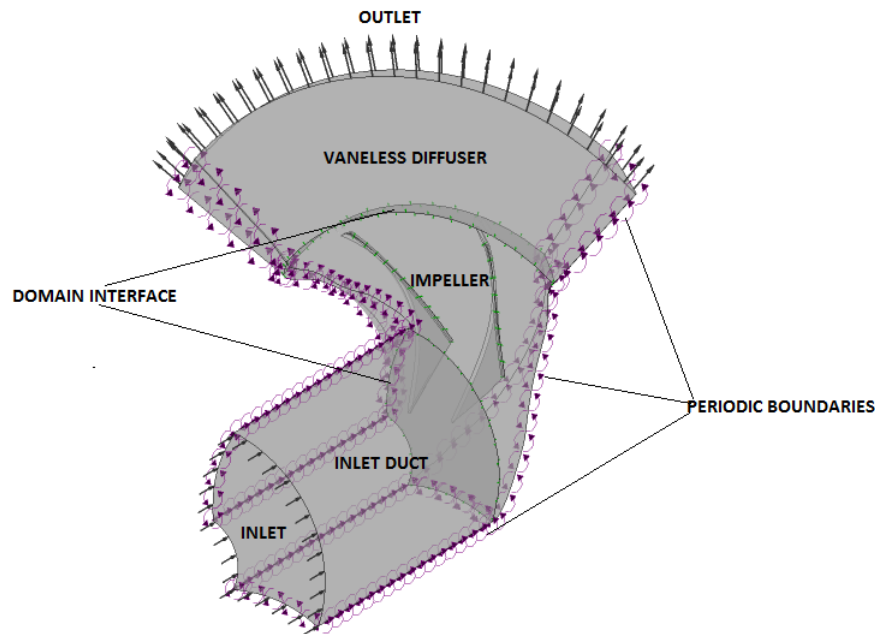


Figure 4-2: Computational domain for the test compressor

considering a rotational symmetry around the blade passages. This is done to reduce the computational effort required for the simulations. Furthermore, appropriate interfaces have been defined between the rotating and stationary parts of the domain. The single passage fluid domain is represented in figure 4-2. The fluid enters the domain through the inlet duct and leaves the domain through the vaneless diffuser. The impeller domain has been modeled as a meridional curve with the help of coordinates as obtained from the drawings. The curve represents surface of revolution. The impeller blades are modeled by defining the wrap angle and thickness curves along the stream-wise direction. The angle and thickness curves have been obtained from the part drawings of the impeller blade provided by MTEE. In the current work, constant blade thickness has been used. The value at the midspan has been used as the average thickness value for the impeller blades. Furthermore, to reduce the computational expense the volute has not been included in the computational domain. In order to incorporate the effects of volute, a meanline code has been developed.

4-2-2 Computational Mesh and Numerical setup

Fig. 4-3(b) presents the structured grid of the impeller domain having a main blade and a splitter blade. ANSYS TurboGrid has been used to obtain the mesh for the entire fluid domain, i.e., inlet duct, impeller and diffuser. Turbogrid is a turbomachinery mesh creation tool that allows the creation of high-quality hexahedral meshes. A structured mesh has been used for the impeller and diffuser passages. An O type mesh has been employed near the leading edge of the impeller blade whereas, an H type mesh has been adopted in the other parts of the passages. In order to resolve the viscous sublayer, a very fine mesh has been maintained near the walls by providing a sufficient number of nodes in the boundary layer region. Thus, an overall $y^+ \approx 1$ has been achieved at the walls. Furthermore, the tip clearance

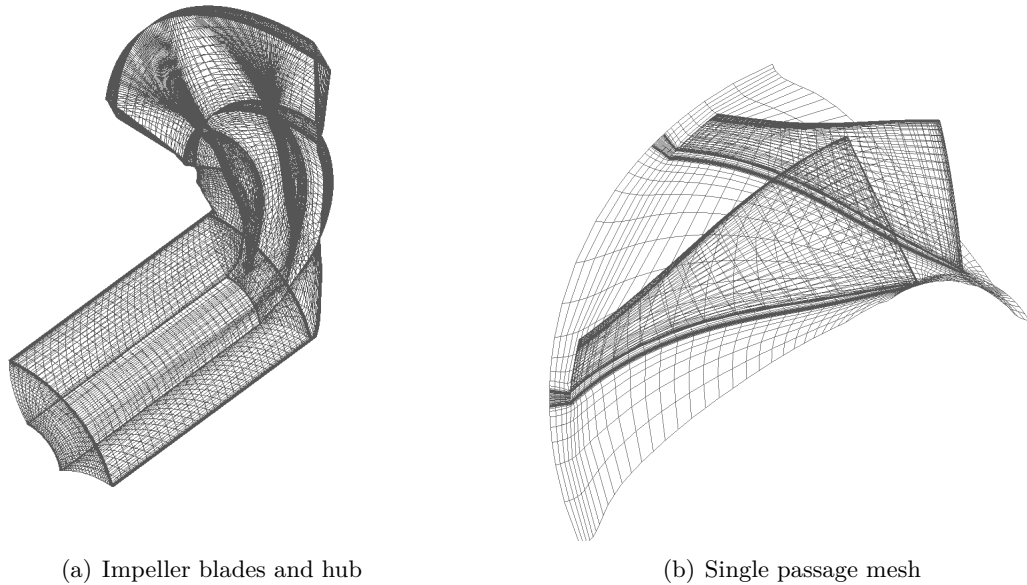


Figure 4-3: The mesh for computational fluid dynamic analysis

of $1mm$ has been incorporated by trimming the blade shroud profile in turbo grid. An H type grid has been used in the impeller blade tip clearance with no hexahedral elements.

In order to ensure that the solutions do not vary with grid size, a grid independence study has been conducted using three computational grid sizes 0.2 million, 0.4 million and 0.8 million for the entire compressor domain. To study the effect of grid on the solution, the pressure ratio and compression efficiency at the peak efficiency operating point of 220000 rpm have been compared for the three grid sizes. The variation in pressure ratio and efficiency has been found to be 0.10% and 0.125 % for the medium grid (0.4 million) and the fine grid (0.8 million) respectively, in comparison to the coarse grid(0.2 million). Thus, the medium grid size of 0.4 million elements was deemed sufficient for further modeling due to the marginal variation in the monitored properties with increasing grid size.

To model the compressor performance, steady state analysis has been carried out in ANSYS CFX. ANSYS CFX is a commercial CFD tool that solves 3D Reynolds averaged Navier-Stokes equations using finite volume discretization in stationary or rotating frames. Furthermore, of the available turbulence models in ANSYS CFX, $k - \omega$ SST model has been used. The details about the model can be obtained from section 2-1-1 of the report.

4-2-3 Boundary Conditions

The compressor as shown in Fig. 4-2 has been simulated as a single passage fluid domain. This is done to save the computational effort required to simulate the complete compressor. Periodic boundary conditions are specified at the symmetric surfaces of the single passage domain. The interfaces between the impeller, diffuser and inlet have been specified as mixing plane or stage. In a mixing plane approach, each fluid domain is treated as a steady state problem. The flow field data from adjacent zones are passed as boundary conditions that are spatially averaged at the mixing plane interface [34]. The impeller shroud has been defined as

counter-rotating wall to allow simulation of the relative motion between the rotating impeller and stationary shroud.

At the inlet boundary, total pressure of 1 atm and total temperature of 293.15K has been specified in accordance with the ambient conditions used by MTEE. A medium turbulence intensity of 5% is specified at the inlet. According to Javed *et al.* [35], variation of turbulence intensity from 1- 10% does not cause a significant variation in the impeller performance.

The outlet boundary of the compressor is specified as mass flow outlet or static pressure depending on operating region of the speed line. Near the choke limit, where a small change in flow rate represents a considerable change in pressure, static pressure is specified at the outlet. For the rest of the operating regions over the speedline, mass flow is specified at the outlet boundary. Furthermore, in order to simulate the choke point the static pressure is consistently reduced till the mass flow at the outlet no longer varies with the reduction in static pressure.

4-3 Compressor Performance Analysis

This section of the chapter deals with predicting the compressor performance over a given operating speed line and validation of simulation results with the experimental test performance map. The section begins by introducing the fundamental equations that form the basis of developing a performance model for the compressor volute. Subsequently, the steady state analysis results for the test compressor has been discussed and elaborated in terms of the compressor performance maps.

4-3-1 Volute Performance Model

In order to model the performance of the compressor, a one-dimensional modeling scheme reported by Japikse [4] has been employed. The model is based on area ratio which is given as :

$$A.R = A_7/A_5 = (\pi/4)D_7^2/2\pi r_5 b_5 \quad (4-1)$$

where A_5 and A_7 are the areas at the inlet and exit section of the volute respectively. The flow is considered as incompressible for the model and a simplified relation for the inlet and exit velocity at the scroll is given by the following equations:

$$V_5 = (Q/A_5)(1 + \lambda^2)^{0.5} \quad (4-2)$$

$$V_7 = (Q/A_7) \quad (4-3)$$

$$\lambda = V_{t5}/V_{m5} \quad (4-4)$$

where V is the absolute velocity, Q is the volumetric flow rate, V_m is the meridional velocity and V_t is the tangential flow velocity.

The losses within the volute scroll can be estimated by very simple models. Firstly, it is assumed that the meridional component of kinetic energy entering the scroll is completely lost. Thus, the loss component can be evaluated as:

$$\begin{aligned}
K_m &= \frac{\Delta p_{o, meridional}}{0.5\rho V_5^2} \\
&= \frac{0.5\rho V_{m5}^2}{0.5\rho V_5^2} \\
K_m &= \frac{1}{1 + \lambda^2} F_1
\end{aligned} \tag{4-5}$$

The above equation represents a reasonable modeling assumption, but may be erroneous if some of the meridional velocity can be used in the downstream element for flow stabilization at the volute exit. In order to take this into account the correction term F_1 is introduced [4].

The second loss component due to the tangential velocity can be modeled with two assumptions. If the core flow accelerates ($V_{t5} < V_{t7}$), then it is valid to assume that no loss occurs. On the other hand, if tangential flow decelerates in the volute ($V_{t5} > V_{t7}$), then the flow diffuses and it can be assumed that the pressure loss is equivalent to the sudden pressure loss in a sudden expansion mixing process [4]. The above loss is modeled as:

$$\begin{aligned}
K_t &= \frac{\Delta p_{o, expansion}}{0.5\rho V_5^2} \\
&= \frac{0.5\rho V_{t5}^2 (1 - A_5/A_7)^2}{0.5\rho V_5^2} \\
K_t &= \frac{(\lambda - 1/A.R)^2}{1 + \lambda^2}
\end{aligned} \tag{4-6}$$

A modification is applied to the equation(4-6) to account for the vortex diffusion. The modified equation is given by:

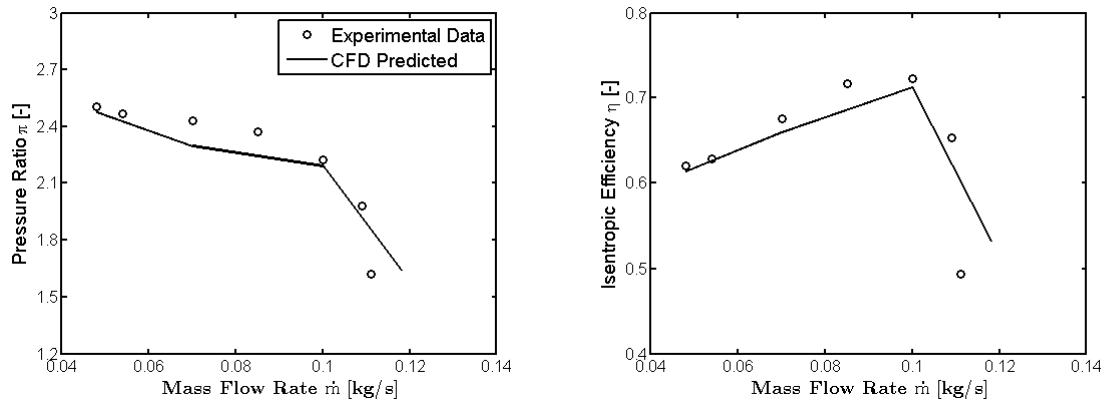
$$K_t = F_2 \left(\frac{r_5}{r_6}\right)^2 \frac{(\lambda - 1/A.R)^2}{1 + \lambda^2} \tag{4-7}$$

where r_5 and r_6 are the diffuser inlet and return bend exit radius.

The pressure loss recovery coefficient is given by:

$$C_p = \begin{cases} \frac{2(\lambda - 1/A.R)}{A.R(1 + \lambda^2)} & \text{for } \lambda A.R > 1 \text{ (Flow Diffuses)} \\ \frac{\lambda^2 - 1/A.R^2}{1 + \lambda^2} & \text{for } \lambda A.R < 1 \text{ (Flow Accelerates)} \end{cases} \tag{4-8}$$

A detailed Matlab code is documented in Appendix B, based on the above equations, to model the performance of the compressor volute. The subsequent subsection describes the results obtained as a consequence of the steady state simulations and the volute performance code. These simulations are necessary to validate the computational model with the experimental results prior to performing further analysis.



(a) Variation of Pressure Ratio over a speed line (b) Variation of isentropic efficiency over a speed line

Figure 4-4: Comparison of the experimental and simulated performance curves for the test compressor

4-3-2 Performance Curves

A steady state simulation of the test compressor has been performed at different operating points at the 220,000 rpm operating speed line to evaluate the performance of the compressor. The results have been compared with the experimental data available from the test maps. Since the test compressors computational domain consists only of the impeller and vaneless diffuser, a meanline code has been incorporated to predict the performance variation as a result of volute. This is done in order to make realistic comparisons with the available test data. The test data is obtained for the complete compressor with the fluid properties evaluated at the compressor inlet and outlet.

The comparison between the simulated performance and test data has been made in terms of compressor pressure ratio and isentropic efficiency. The overall compressor performance for both the smooth case and the rough case, in terms of the speed lines representing the experimental data and simulated results, is depicted Fig. 4-4. A reasonable agreement is observed between the simulated performance and the test results. The numerical computations predict the trend of pressure ratio reasonably for the simulated speed line. A kink is observed at the low mass flow rates. This discrepancy in the pressure ratio prediction at low mass flow rates can be attributed to the onset of rotating stall. The rotating stall is an unsteady phenomenon and cannot be accurately accounted by steady state simulations. Furthermore, at the low mass flow rate, a very small deviation in the pressure ratio is observed when compared with experimental results. On the other hand, the simulations predict the choking condition but the lowest pressure ratio is observed at a higher mass flow by the CFD computations.

As seen in Fig. 4-4, the simulations also capture the trend of the isentropic efficiency fairly well. In this case also they predict the choking condition at a higher flow rate as compared to the experiments.

It can thus be concluded from the current analysis that the CFD setup and simulation are capable of predicting the characteristic curves of the compressor performance, despite some deviations observed near the low flow rate region and choke point. This deviation can be

attributed to the limitations of the turbulence model and the mixing frame approach applied at the interfaces.

4-4 Impeller Flow Field Analysis

The Fig. 4-5 shows the contours of the meridional velocity, relative Mach number and static entropy contours at various streamwise locations along the compressor impeller blades. All the results have been documented for the best efficiency case which corresponds to a mass flow rate of 100 g/s at the rotational speed of 20000 rpm.

The relative Mach number contours are presented in Fig. 4-5(a). It can be observed from the figure that at the suction side of the main blade leading edge, a region of supersonic Mach number exists. The high relative Mach number region extends both along the circumferential direction and the spanwise direction. The existence of this region can be attributed to the high relative mass flow rate, which in turn results in high meridional velocity. As a result, the relative flow angle is lower than the blade angle. This results in a positive incidence angle which causes the flow to accelerate [36]. This region of high relative Mach number is followed by an area of low relative Mach number, which increases in the both streamwise and spanwise direction. It can be observed that the relative Mach number decreases along the blade passages. Near the impeller outlet, a low Mach number region can be observed near the shroud. This region can be attributed to a reduction in the flow velocities as a consequence of the tip leakage flows.

Fig. 4-5(b) presents the meridional velocity contours at different streamwise location along the compressor impeller. The meridional velocity is the absolute velocity component that represents mass flow rate through continuity equations [36]. The variation of the meridional velocity across the impeller also follows a similar trend as that of relative Mach number. A low-velocity area develops on the shroud near the suction surfaces of both the main blade and splitter blade. The largest magnitude of the meridional velocity is observed near the hub of the impeller domain. At the trailing edge, a substantial region near the shroud can be observed to have a low meridional velocity.

As a result of the secondary flows and wake development, losses are expected in the impeller domain. The figure 4-5(c) presents the contours of entropy generation in the blade passage. It can be observed from the figure that the loss production along the blade passage is concentrated near the impeller shroud. The largest loss region is located near the trailing edge shroud. This can be attributed to large tip leakage flows which significantly affects the main core flow.

In order to further analyse the flow field near the impeller shroud, the relative Mach number contour at a location close to the impeller shroud have been shown in Fig. 4-6. It is evident from the figure that close to the main blade leading edge, where a high-velocity region develops near the suction side, the relative Mach number is supersonic. Also, high Mach number can be observed close to the leading edge of the splitter blade. However, a decrease in the relative Mach number can be observed in the streamwise direction. In the case of both main blade and splitter blades, a low-velocity wake region develops further downstream.

The subsequent section deals with analyzing the changes in the centrifugal compressors flow structure as a result of a reduction in the mass flow parameter at different operating points

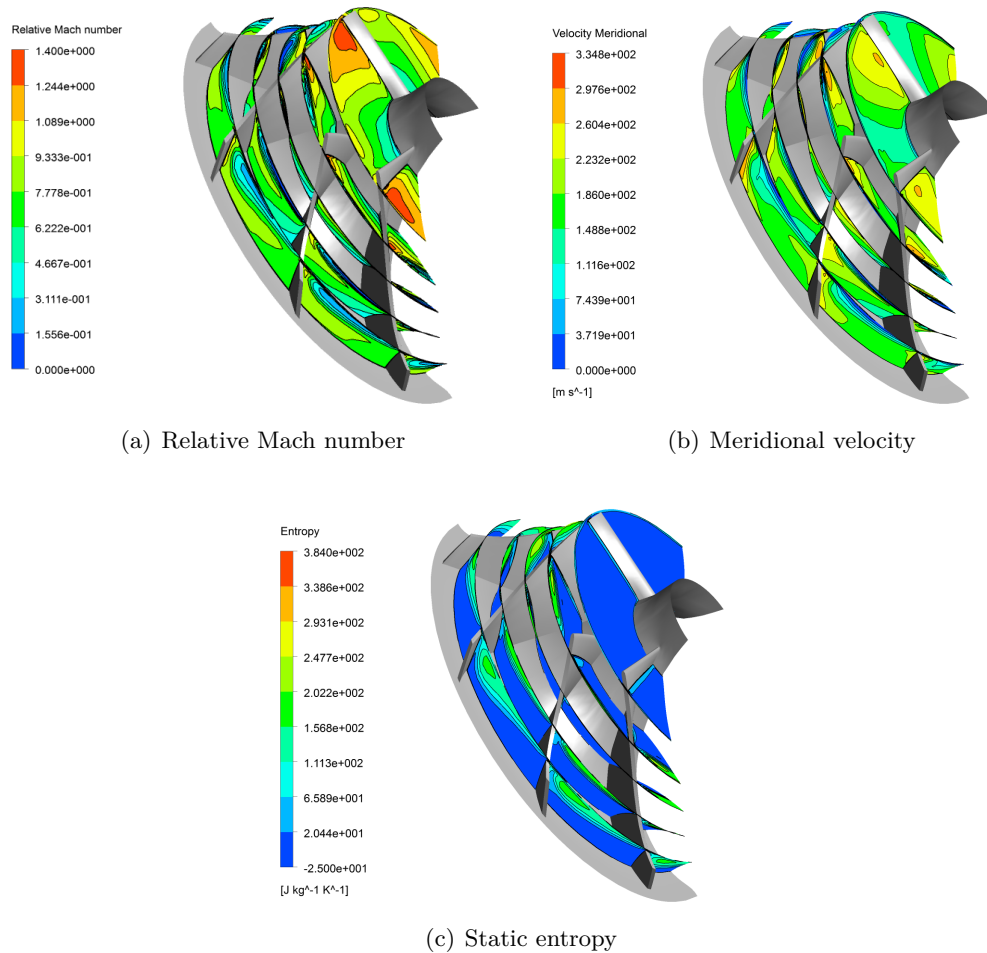


Figure 4-5: Relative Mach number, meridional velocity and static entropy contours at different streamwise direction at the best efficiency point

along a speedline. The analysis has been presented by analyzing the changes in the flow structure within the impeller and diffuser.

4-5 Flow Phenomenon Responsible for Surge

In order to evaluate the performance of the compressor over a speedline, different operating points ranging between the choke and the surge margin of the compressor have been simulated as described in section 4-3. The current section deals with gaining greater insight into the change in associated flow behavior as the mass flow is reduced within the centrifugal compressor. The simulations at low mass flow rates explain the details of the phenomenon responsible for the onset of the unstable compressor operations. The unstable flow regions such as separation zones, inlet recirculation regions and other unstable flow phenomena which cause the onset of surge have been identified and their growth with lower mass flow rates is observed.

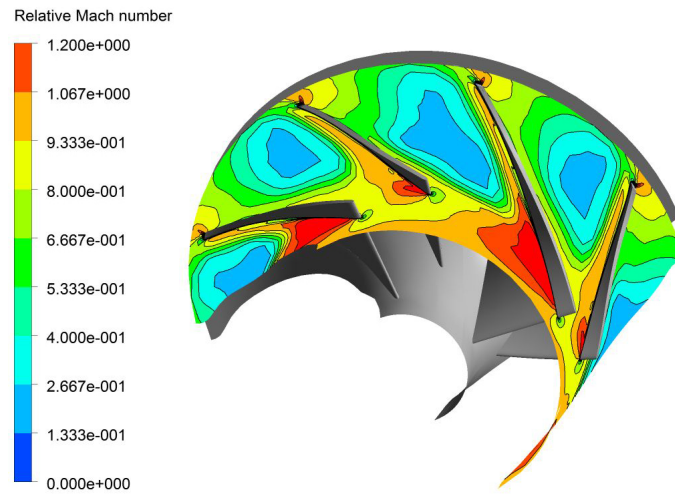


Figure 4-6: Relative Mach number contour at a section located at 80% of impeller spanwise direction

4-5-1 Inlet Recirculation Region

The inlet recirculation zone in a centrifugal compressor is a stationary phenomenon. The inlet recirculation region is formed at the radial machines inlet with a pressure growth at outlet [37]. In the view of Breugelmans and Sen [38], the inlet recirculation region forms the first sign of unstable operation. Fig. 4-7 depicts the growth of the inlet recirculation region in the test compressor with the mass flow rate in terms of the velocity vectors along the meridional plane. According to Chodkiewicz *et al.* [37], the inlet recirculation effects the compressors operating conditions and may not be equivalent to the appearance of surge. However, in case of high-pressure ratio compressors, it might cause an intensive surge. It can be seen that the inlet recirculation region develops even at high mass flow rates (4-7(b)). As the flow rate is further reduced the recirculation region grows and effects a substantial portion of the flow field near the impeller shroud as depicted in Figs. 4-7(c) and 4-7(d).

4-5-2 Flow Separation within the Impeller

As mentioned in Chapter 1, the flow separation effects the stable operation of the compressor. The flow field within a centrifugal compressor is a complex viscous three-dimensional flow wherein the curvature and rotational effects result in the development of non uniform flow. The effect of mass flow reduction through the centrifugal compressor on the flow field within the compressor is presented in terms of the velocity contours along a midplane of the impeller section in Fig. 4-8. The operation of a centrifugal compressor at lower flow rates causes the flow to separate near the trailing edge and along the suction side of the impeller and splitter blades. This flow separation causes development of low energy wake region or separation bubble. The flow separation in this region results from the combined effect of the secondary flows (Fig. 4-9) and adverse pressure gradients. The Fig. 4-9 shows that at low mass flow

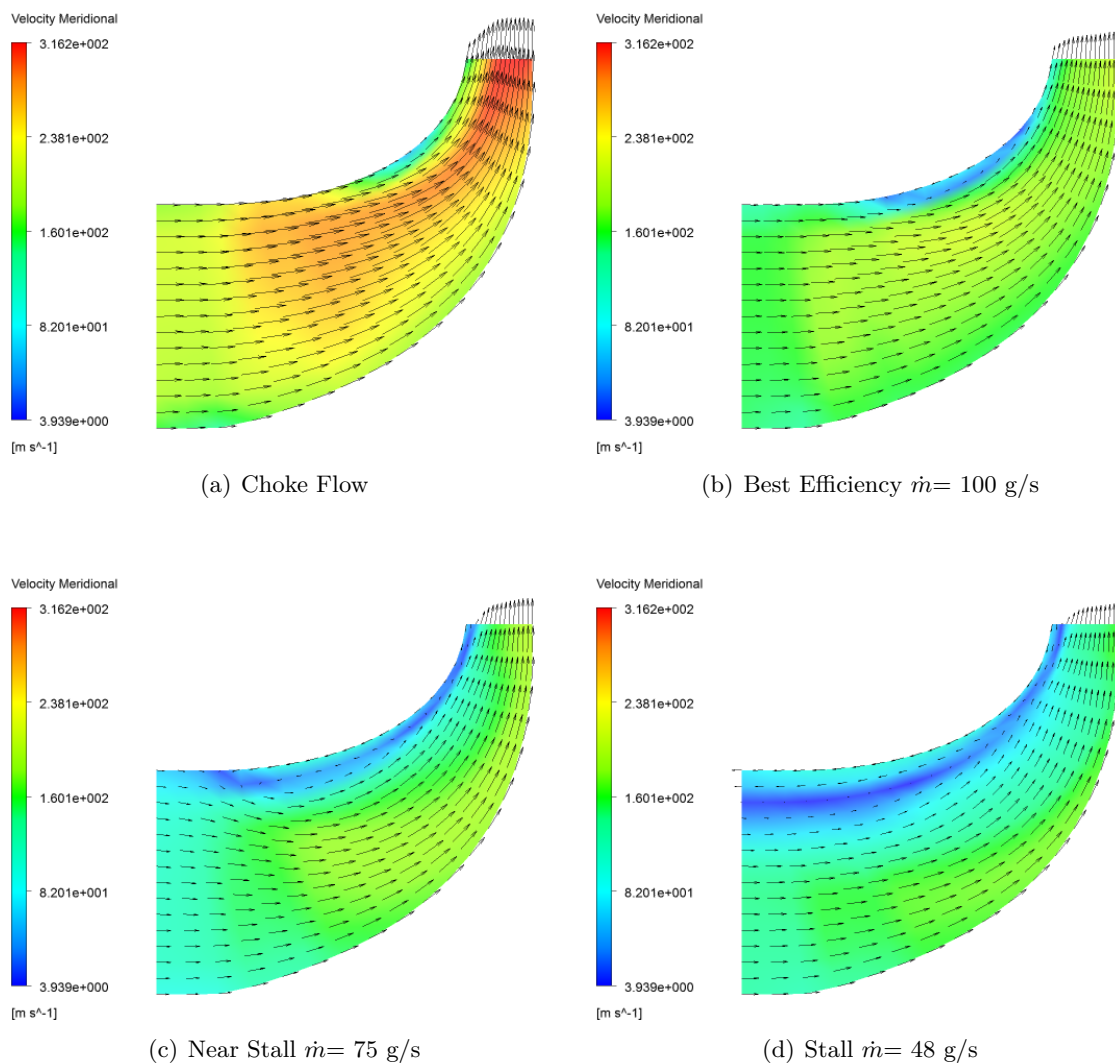


Figure 4-7: Meridional velocity contours at the diffuser midplane for different flow rates

rates, large secondary flow exists near the impeller shroud which affects the core flow. The development of the secondary flow provides an indication regarding the onset of unstable compressor operation.

4-5-3 Flow Separation within the Vaneless Diffuser

The flow separation within the centrifugal compressor forms a critical issue that affects the stable operation. Rotating stall in diffusers is caused in most cases by reverse flow based on three dimensional separation of boundary layer [39]. The separation in the vaneless diffuser essentially occurs at low mass flow rates. This is because the flow in a vaneless diffuser is skewed and at low mass flow rates, a local reverse flow region occurs. This is a precursor for Rotating stall [39]. The experimental analysis performed by Kinoshita and Senoo [7],

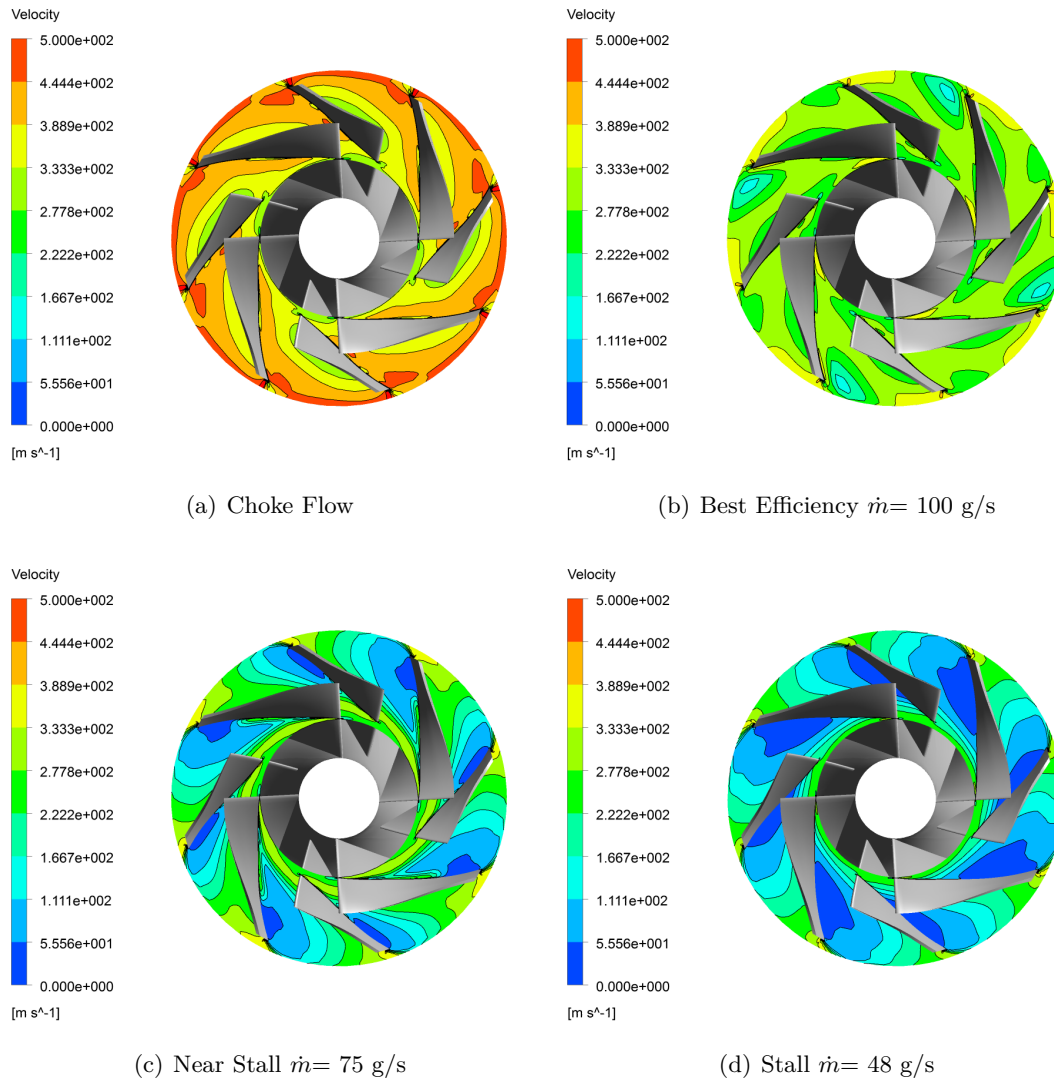


Figure 4-8: Relative velocity contours at the midspan of the impeller domain

Abdelhamid [40], Jaatien- Vaari [41] reveals that at low flow rates the efficiency of compression system decreases because of flow separation and rotating stall inception, while at higher flow rates, the compressor stage has a wider operating range and higher polytropic efficiency.

Fig.4-10 describes the evolution of the separation in a vaneless diffuser as a consequence of the reduction in the flow rate from the choke to stall in terms of the contours of the meridional velocity. It is observed that as the mass flow reduces, the separation and reversals at the diffuser increase. The flow at the diffuser shroud separates and reverses back into the impeller at the low mass flow operating points. Near the operating point close to the stall, it can be observed that flow reversal occurs across the entire diffuser shroud(Fig. 4-10(c) & 4-10(d)). Thus, it can be concluded that at low flow rates, the flow instabilities in the diffuser may form an essential cause of the unstable compressor operation.

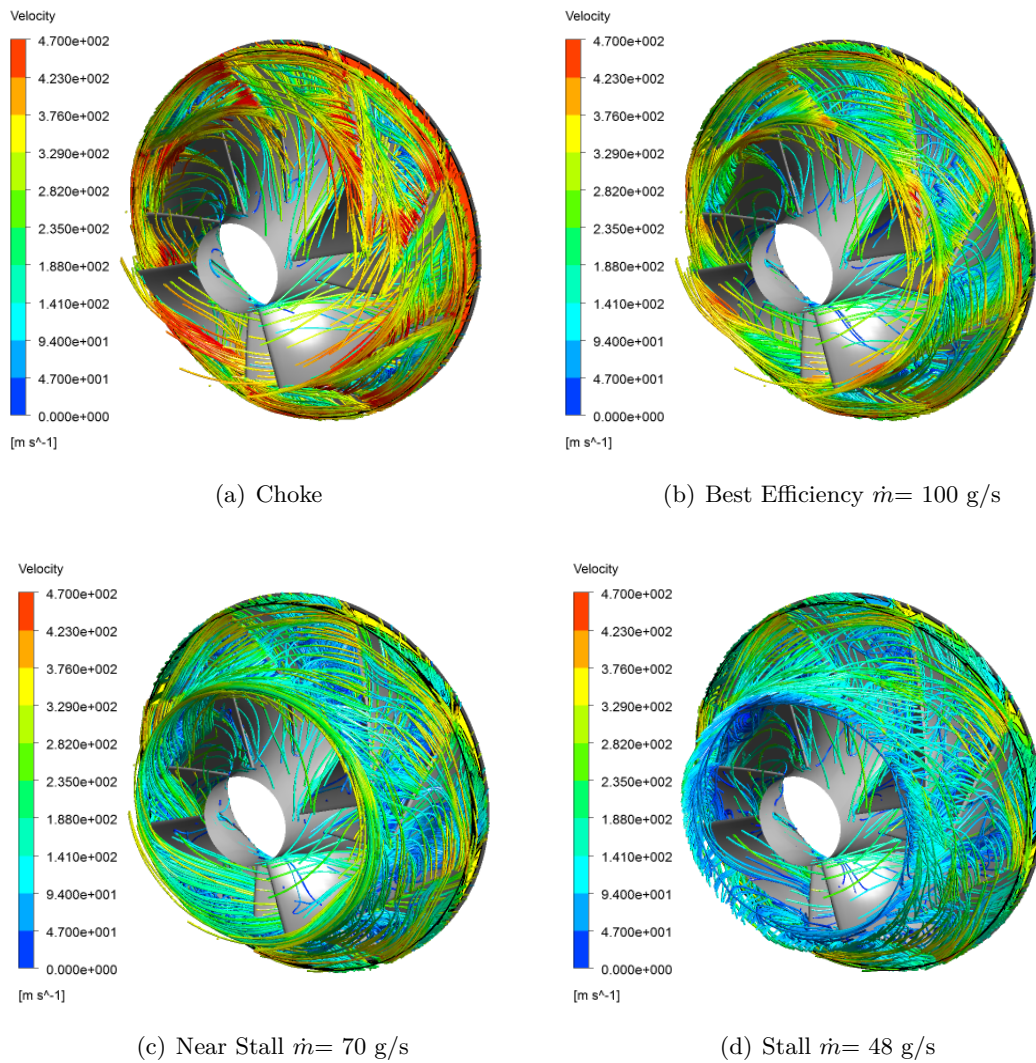


Figure 4-9: Relative velocity streamlines depicting the secondary flow structure at different operating points

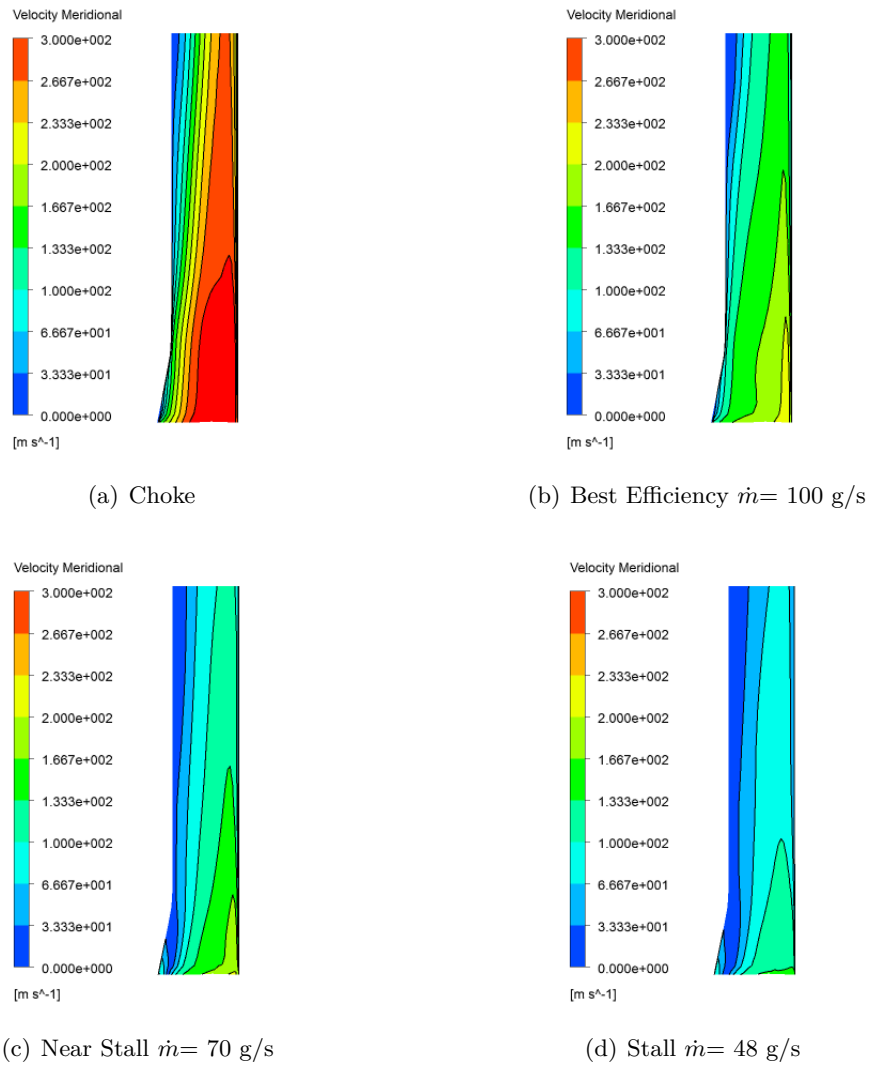


Figure 4-10: Meridional velocity contours at the diffuser mid-plane for different flow rates

Roughness Application and Evaluation

The previous chapter highlights the CFD modeling applied to the test case centrifugal compressor to predict its performance. In addition to that, it describes the evolution of the flow instabilities within the compressor with reduction in the mass flow rate. The current chapter presents a parametric study on the effect of the roughness height and location on the flow instabilities in the centrifugal compressor. The surface roughness has been introduced on the compressor impeller and diffuser. In order to study the effect of roughness on the flow behavior, simulations have been carried out at a flow rate lower than the stall point flow rate as predicted by the test map. Firstly, the study has been carried out by analyzing the effect of the predefined wall roughness applied on the impeller and diffuser domain. Lastly, localized roughness strips have been modeled on the impeller blade and diffuser, and their effects on the flow field have been studied.

5-1 Wall Roughness Analysis

The current section of the chapter deals with analyzing the effect of increasing the roughness at the impeller blades, inlet shroud, impeller and diffuser shroud on the flow field within the compressor. The rationale behind choosing the above locations in the compressor can be obtained from chapter 4. It can be observed from Fig 4-7 to 4-10 that at low mass flow rates, considerable flow reversals prevail near the diffuser shroud. Furthermore, the flow field also separates near the blades trailing edge. Lastly, an increase in the surface roughness at inlet shroud is considered to reduce the extent of inlet recirculation that affects the inlet duct of the compressor.

Table 5-1 documents the magnitude of the surface roughness applied to the compressor walls. In order to relate the geometric roughness height to the equivalent roughness, the following correlation as defined in the work of Simon and Bulskamper [42], has been used:

$$k_s = 2R_a \tag{5-1}$$

Table 5-1: Magnitudes of considered roughness elements

S No	Geometric Roughness Height $k(\mu m)$
1	50
2	100
3	200

where R_a is the centerline average roughness value.

It has been assumed that the geometric roughness height (k) is defined by centerline average roughness value.

The effect of the engineered roughness on the flow structure has been studied separately for the diffuser and the impeller. The following sections provide the results pertaining to the analysis. To begin with, the effect of additional roughness on the flow through the vaneless diffuser is elaborated. Next, a brief discussion about the effect on the impeller flow field and reversals.

5-1-1 Effect of Surface Roughness on Diffuser Flow Field

Fig. 5-1 shows the streamlines along the meridional plane of the diffuser. The influence of different magnitudes of roughness on flow reversals in the centrifugal compressor has been highlighted in the figure. It also shows a comparison of the smooth case with the roughened case. For all the cases studied, it can be seen that a region of reversed flow exists at the diffuser inlet in proximity of the shroud. The existence of these flow reversals can be attributed the fact that the flow at the diffuser inlet is highly unsteady and viscous [36]. At the impeller outlet, a complex flow field exists and strong fluctuations in the velocity and flow angle are observed [36]. It is believed that a jet-wake pattern exists at the impeller outlet. The jet flow structure exists at the blade pressure side and is considered almost loss-free whereas the wake forms the region of low flow velocity [43]. The wake carries losses, turbulence and accumulates near the shroud or suction side edge [36]. This explains the existence of the region of reversed flow at the inlet of the diffuser.

It can be seen that in case of the smooth-walled compressor, a reversed flow region exists along the entire shroud wall. In addition, a flow reversal can be observed at the hub near the diffuser exit. The addition of surface roughness has a considerable effect on the diffusers flow field. The increase in roughness causes a reduction in reversals at the diffuser inlet. The most prominent effect in this case is observed with the roughness magnitudes of $200 \mu m$ and $100 \mu m$. The increase of roughness also causes an early reattachment of the flow and therefore causes a reduction in the flow reversals along the diffuser shroud. Figs. 5-1(b), 5-1(c) and 5-1(d) show the effect of increased roughness on the flow reversal at the diffuser. The increased roughness height also causes an elimination of the reversed flow region at the diffuser hub.

Figs. 5-3 and 5-4 illustrate the effect of surface roughness on the spanwise distribution of radial and tangential velocity respectively at the diffuser. The spanwise direction is based on the diffuser width within the end walls (i.e., from the hub to shroud) and has been normalized such that it ranges between 0 and 1. The distributions have been obtained at different streamwise

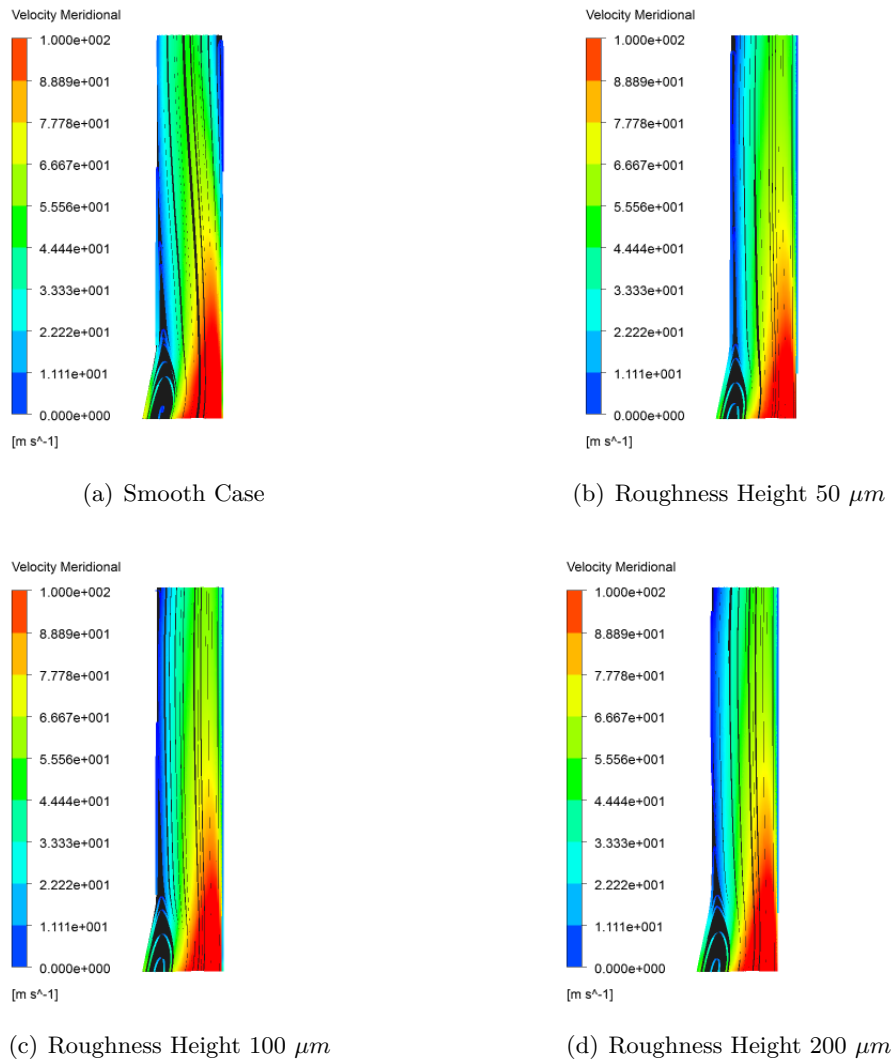


Figure 5-1: Meridional velocity streamlines along the diffuser meridional plane for different surface roughness

locations along the diffuser meridional plane. These locations are presented in Fig. 5-2. As depicted in the Fig. 5-3(a), reverse flow zone occurs at the diffuser inlet for all the simulated cases. However, an increase in the roughness results in a reduction in the flow reversals. Thus, an increase in the wall roughness at the impeller shroud and blades results in a stabilization of the outlet flow and results in reduced flow reversals at the diffuser inlet.

At streamwise location 2, it can be observed from the figure 5-3(b), that an increase in the roughness at the diffuser shroud results in a decrease in reverse flow zone. As a result of the increase in the magnitude of the surface roughness from 0-200 μm , it can be observed that the flow reversals are completely eliminated. Similar results are observed at further downstream locations. Fig. 5-3(c) shows complete elimination of the reverse flow zone as a result of an increase in surface roughness. As compared to the baseline smooth case, the cases with a roughness magnitude of 200 and 100 μm exhibit a complete elimination of the

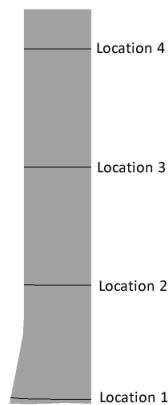


Figure 5-2: Streamwise locations used to study the spanwise distribution of radial and tangential velocities in the diffuser

flow instability at the shroud wall. Although the case with a roughness magnitude of $50 \mu m$ shows a reduction in the reverse flow zone as compared to the smooth case, a small region of separated flow still exists in this case. Furthermore, it can be observed from the figure that the peak of the radial velocity shifts towards the hub for the roughened cases. This shift in the velocity peak can be attributed to the increase in the boundary layer thickness at the shroud wall because of the increase in the roughness height.

It is seen in the Fig. 5-3(d) that a separated flow region exists close to the diffuser exit for the smooth case. However, addition of the roughness to the diffuser shroud eliminates this flow instability.

Fig. 5-4 elaborates upon the spanwise distribution of tangential velocity at different streamwise locations along the diffuser's meridional plane. It can be seen that the addition of roughness to the diffuser shroud results in a decrease in the tangential velocity. This translates to an overall performance reduction of the turbo-machine. However, a reduction in the tangential velocity also causes a decrease in the friction losses which compensates for the reduction in performance [44].

5-1-2 Effect of Surface Roughness on Impeller Flow Field

This section of the chapter presents the effect of increased surface roughness height on the flow field of the centrifugal impeller. The nature of the impeller flow, especially the exit flow has a significant effect on the performance of the compressor stage. A detailed investigation is thus performed to investigate the effect of wall roughness on the flow structure in the impeller. The analysis of the improvement in the flow structure is difficult using steady state simulations because the stall and surge are unsteady phenomena. Nevertheless, a brief insight has been provided by considering the flow behaviors at different locations in the impeller domain.

Fig. 5-5 shows the contours of total pressure at a section located at 70 % of the impeller span. The distribution of total pressure gives an indication of the flow disturbances and losses. Thus, the regions with a lower value of the total pressure correspond to the locations

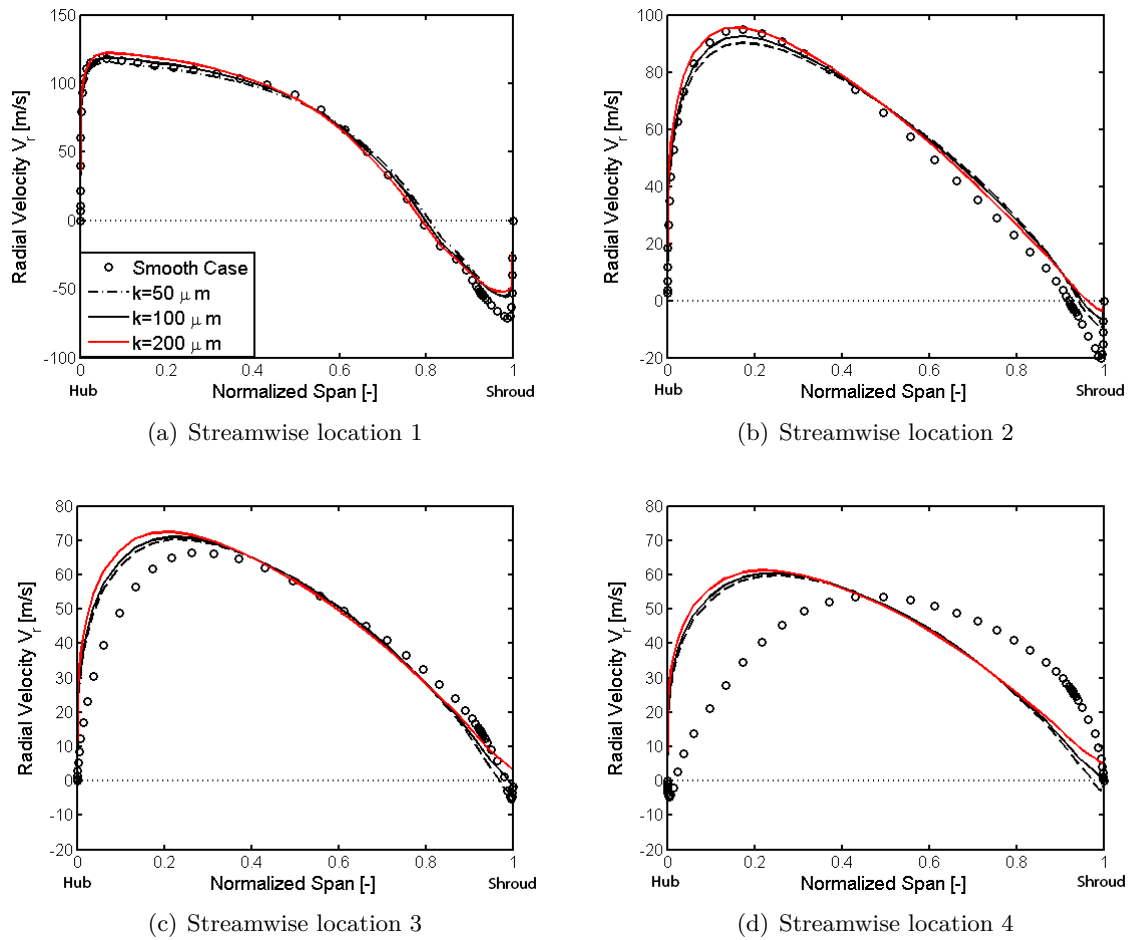


Figure 5-3: Variation of radial velocity from hub to shroud at different streamwise locations (Fig 5-2) along the diffuser

where the generated losses are significantly greater. In the smooth case Fig. 5-5(a), it can be observed that close to the main blade's suction side, an area of low total pressure is present (depicted by the blue region). This region can be attributed to the wake that develops as a result of the three-dimensional separation due to the secondary flows. It can be inferred from Figs.5-5(b), 5-5(c) and 5-5(d) that an increase in the magnitude of surface roughness at the impeller blade, impeller and inlet shroud causes a reduction of the low total pressure region.

The effect of the increased roughness magnitude can also be interpreted in terms of the variation of the mean meridional velocity from the inlet to the outlet of the impeller domain. This variation is depicted in Fig. 5-6. It can be seen that addition of roughness causes an increase in the magnitude of the meridional velocity. Since the meridional velocity is influenced by the blockage of the flow passage, an increase in the meridional velocity can be attributed to the additional blockage introduced by the thickening of the boundary layer.

Fig. 5-7 presents the contours of the meridional velocity at a streamwise location close to the impeller blade trailing edge. It can be seen from the Fig. 5-7(a) that a low momentum wake region exists near the main blade hub at a location close to the trailing edge. Furthermore,

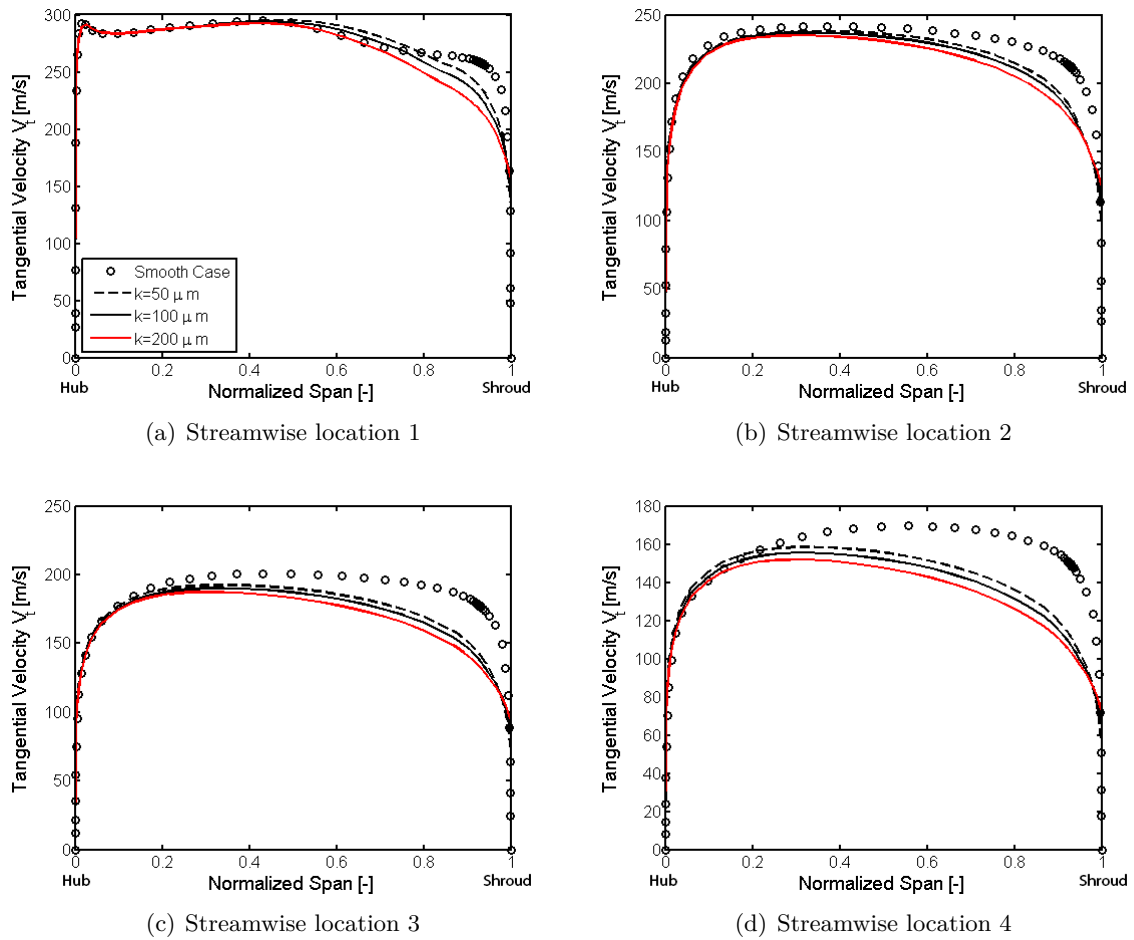


Figure 5-4: Variation of tangential velocity from hub to shroud at different streamwise locations (Fig 5-2) along the diffuser

it can be clearly seen that an increase in the roughness height results in a reduction in the separation zone (5-7(b), 5-7(b), 5-7(d)). The increase of the roughness height to $50 \mu m$ clearly causes a reduction in the wake region in proximity of the main blade.

Fig. 5-8 depicts the distribution of mass flux (mass flow per unit area) at the impeller trailing edge. The plot obtained from the analysis represent the blade to blade variation of the mass flux at three spanwise locations: hub, mid-span and shroud. At the shroud, the Fig. 5-8(a) reveals an improvement in the mass flux distribution near the suction side of the main blade. However, a significant improvement is not seen at the other blade to blade locations (Figs. 5-8(b) and 5-8(c)). This can be attributed to an increase in the boundary layer thickness close to the blades and shroud as a result of the surface roughness. This increase in the boundary layer thickness causes enhanced blockage effect. It can be further observed that the increase in the roughness height results in an increase in the mass flux distributions at the hub and mid-section of the impeller blade's trailing edge. Although the improvement at the midspan is not that significant, it gives an indication of the ability of the roughness elements to cause a slight improvement in the flow structure. The relative increase in the mass flux distribution

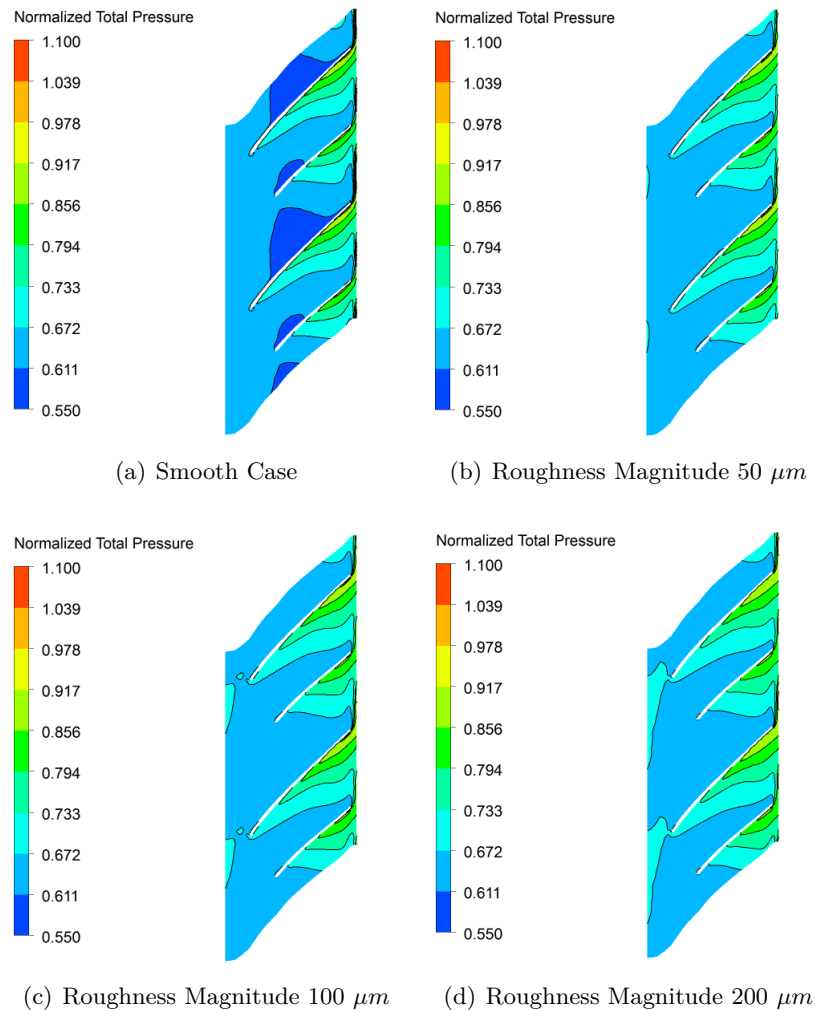


Figure 5-5: Normalized total pressure contours on a section located at 70 % of the impeller spanwise direction

as a result of the different roughness heights is observed to be the same. The increase in the mass flux represents a reduction in the flow instabilities as a consequence of the secondary and tip leakage flows. However, the gains achieved in terms of the reduction in low momentum wakes due to the roughness elements is also hampered by an increase in the boundary layer thickness.

5-2 Localized Roughness Strips and their Effect on Flow Field

The previous section of the chapter describes the effect of the wall roughness applied to impeller blades, impeller shroud, diffuser and inlet duct's shroud on the flow instabilities and flow structure within the compressors flow domain. It can be concluded from the analysis that the increase in the roughness height results in an improvement of the flow structure within the compressor.

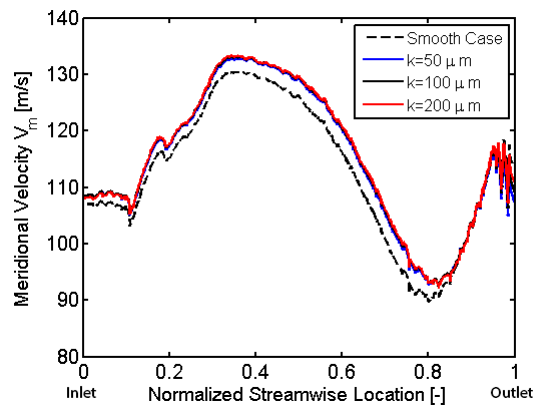


Figure 5-6: Variation of meridional velocity from the inlet to the outlet of the impeller domain mid span.

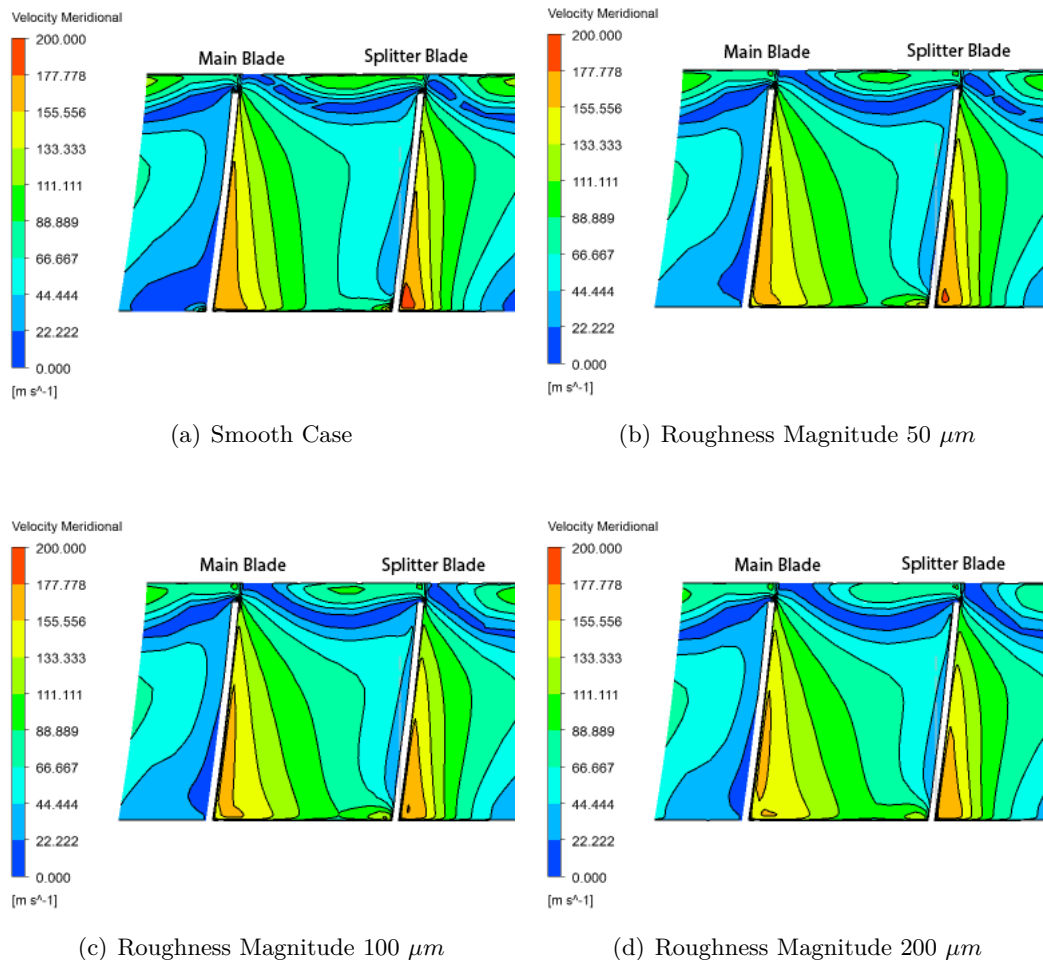


Figure 5-7: Meridional velocity contours at a location close to the trailing edge

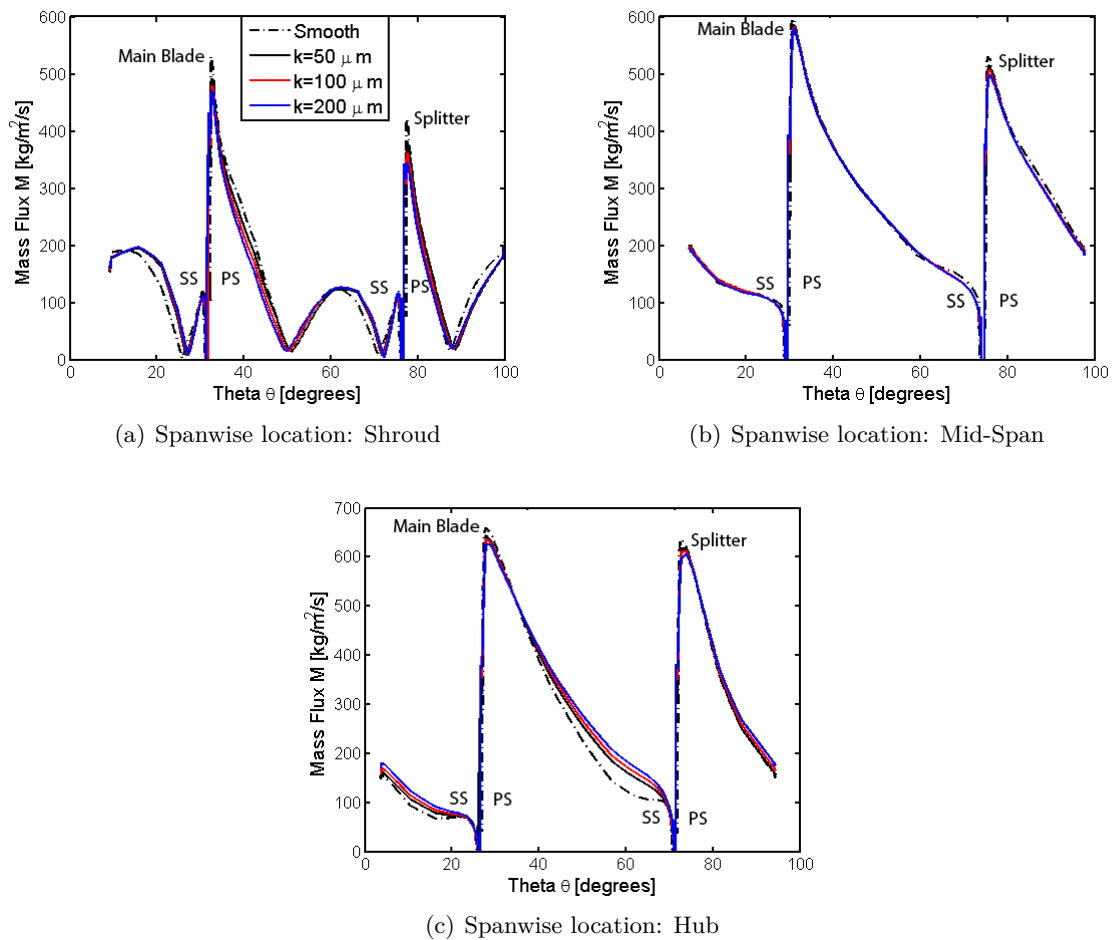
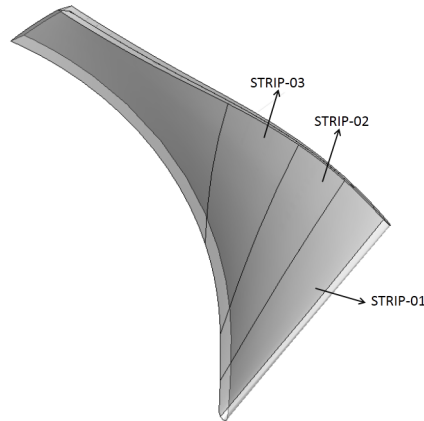


Figure 5-8: Circumferential mass flux distribution at the impeller trailing edge for the different roughness cases

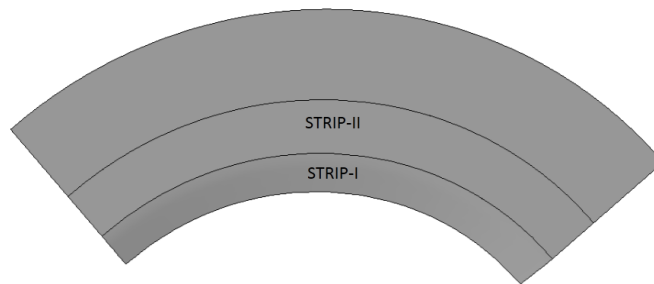
The current section of this chapter focuses on analyzing the effects of localized roughness strips applied to the diffuser shroud and impeller blade. This section is split into following parts: firstly, it describes the methodology adopted for modeling and analyzing the localized roughness strips. Next, it provides the details pertaining to the parametric roughness study. Lastly, the results of the study are described.

5-2-1 Modeling of Localized Roughness Strips

In order to study the effects of localized surface roughness on the flow instabilities in the compressor stage, the suction surface of the impeller blade has been divided into three sub regions. In addition to this, the shroud of the compressor diffuser has been split into two regions. The three patches on the impeller blade have been referred to as "I", "II" and "III". Those on the diffuser have been named as "1" and "2". The Fig. 5-9(a) and 5-9(b) presents the modified domains for the diffuser shroud and the impeller blade.



(a) Modified rotor domain



(b) Modified diffuser shroud

Figure 5-9: Modified impeller and diffuser domain for the parametric roughness study

5-2-2 Roughness Parametrization

This section presents the design of experiments applied for the parametric roughness study. Table 5-2 provides the information pertaining to the location and magnitude of the roughness strip. Numerical simulations have been carried out for all the cases documented in the table 5-2. Furthermore, for all the simulations, the impeller shroud and inlet duct have been modeled as a smooth wall. Thus, a roughness height of $50 \mu\text{m}$ at the diffuser inlet strip is sufficient to cause a improvement in flow structure.

5-2-3 Effects of Roughness Location and Magnitude

The current section of the report deals with the parametric study about effect of the roughness location and magnitude on the flow structure within the centrifugal compressor. The study has been conducted by carrying out numerical simulations at a mass flow rate lower than the last stable operating point defined by the experimental compressor map. Thus, the entire analysis has been based on the flow conditions at a mass flow rate of 38g/s and 220000 rpm rotational speed. In order to conduct a comparative study, all the results have been compared with the smooth baseline case which forms the benchmark for the current analysis. The entire

Table 5-2: Roughness magnitude and location

S No	Roughness Location	Roughness Height $R_a, (\mu m)$
1	I,1	50
		100
		200
2	II,2	50
		100
		200
3	3	50
		100
		200

study has been conducted by analyzing the effect of roughness location on the flow fields of impeller and diffuser. The subsequent literature provides the results pertaining to the study.

5-2-4 Effect of Roughness Strips on Diffuser Flow

The current subsection presents the results concerning the effect of localized roughness strips on the diffuser flow field. The results have been presented for Case 1,2 and 3 documented in table 5-2 and have been compared with the results for the smooth case. The subsequent literature presents the results for the three cases.

Roughness Case 1

The Fig.5-10 shows the radial velocity distribution at the diffuser mid and exit corresponding to the roughness height documented in Case 1 of the table 5-2. The figure depicts that the addition of localized roughness close to the diffuser inlet effects the flow profile. In comparison with the smooth case, the roughness strip at the inlet can be seen to reduce the magnitude of flow reversal at the mid-span of the diffuser. In addition to this, it causes a complete elimination of the reverse flow region close to the diffuser outlet. Thus, this gives an indication about the improvement in the flow structure brought about by the addition of localized roughness. However, the strip close to the inlet does not cause a significant effect on the flow reversal at the diffuser inlet. Furthermore, it can also be seen that different magnitudes of the roughness height have a similar effect on the flow profile.

Roughness Case 2

Fig. 5-11 shows the effect of localized roughness on the diffuser spanwise distribution of the radial velocity. The effect of the localized roughness has been considered in terms of the strip 2 defined in Fig. 5-9(b). The figure reveals that the addition of localized roughness strip at a streamwise location away from the diffuser inlet has limited influence on the diffuser flow instabilities. The increase in the surface roughness at the strip 2 does not cause a

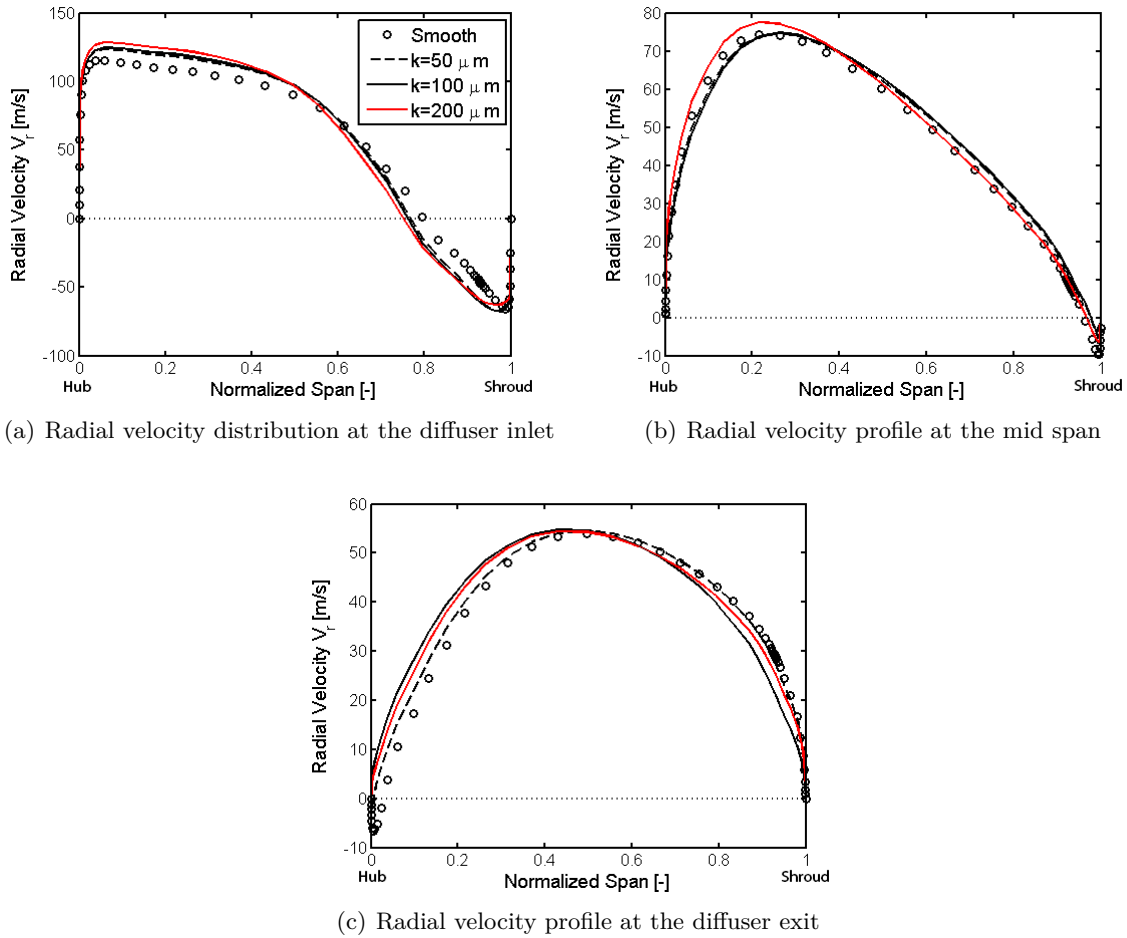


Figure 5-10: Modification of the radial velocity distribution as a result of the localized roughness applied to strip I at the diffuser

significant improvement in the flow structure at the shroud of the diffuser (Fig. 5-11(b)). However, roughness element causes a reduction of the reverse flow region at the hub close to the diffuser exit as depicted in Fig. 5-11(c). However, it does not cause a complete elimination of the flow reversals at the diffuser hub.

Thus, it can be concluded from the current analysis that addition of the localized roughness elements close to the diffuser inlet results in a reduction in the flow instability within a centrifugal compressor. In addition to this, it can be inferred from the current analysis that a roughness of $50 \mu m$ is sufficient to induce an improvement in the flow characteristics within the diffuser.

5-2-5 Effect of Roughness Strips on Impeller Flow Field

This section deals with analyzing the effect of roughness location and height on the flow in the centrifugal compressor's impeller. The study has been conducted by considering patches of roughness at the main blade's suction side as shown in Fig. 5-9(a). The roughness locations

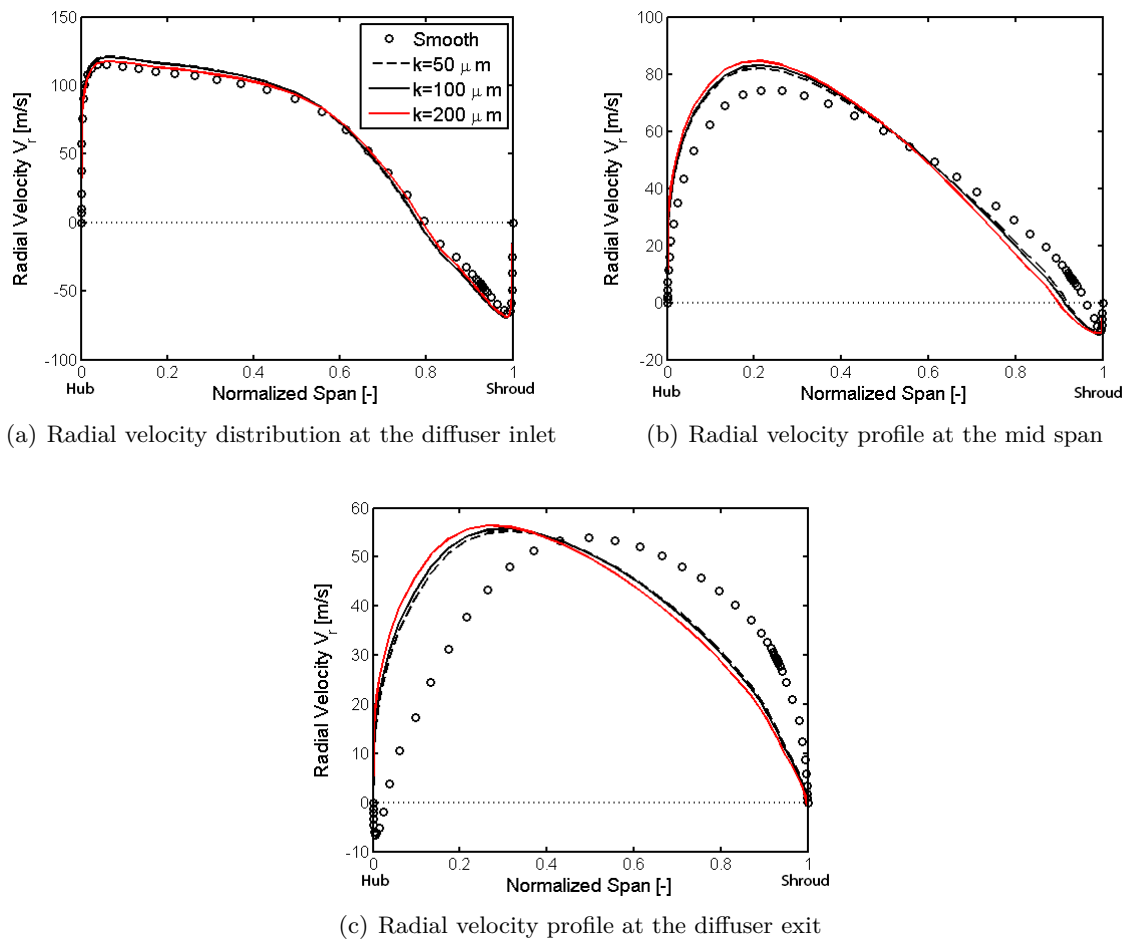


Figure 5-11: Modification of the radial velocity distribution as a result of the localized roughness applied to strip II at the diffuser

have been applied only to the suction side because a considerable wake affected flow can be observed near the suction side of the main blade. Furthermore, in order to reduce the viscous drag, sectioned roughness patches are considered instead of the overall wall roughness. The subsequent literature describes in detail the effect of localized impeller roughness strips on the flow behavior within the impeller domain. The study has been carried out by analyzing the effect of different roughness magnitudes applied to the independent locations 1, 2 and 3 as shown in Fig. 5-9(a).

Impeller Strip 1

The current section of the report presents the results of adding the roughness strip close to the leading edge of the impeller blade. The effect of adding roughness can be interpreted in terms of the mass flux distribution close to the impeller shroud. The Fig. 5-12 shows the effect of adding localized roughness strip close to the blades leading edge on the blade to blade mass flux distribution at the trailing edge. It can be seen that in comparison to

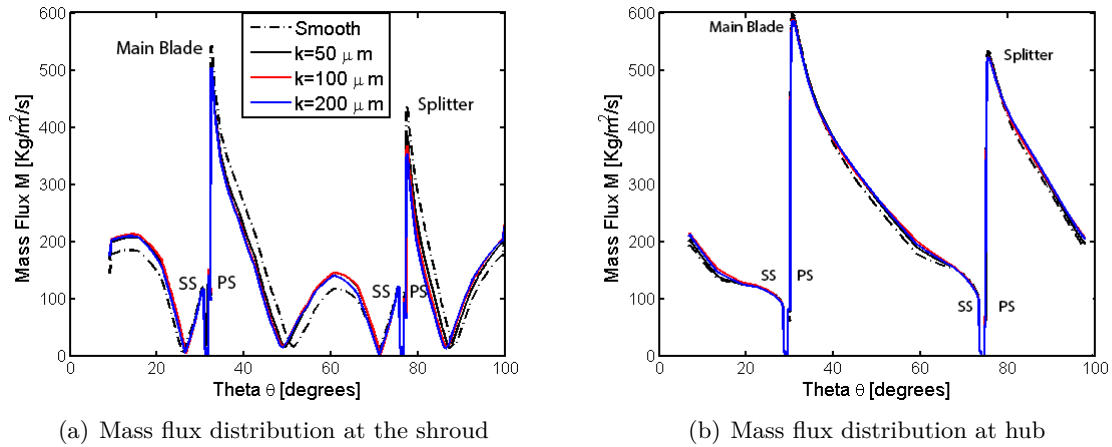


Figure 5-12: Modification of the mass flux distribution as a result of the localized roughness applied to strip 1 at the impeller

the overall roughness case, roughness at a strip 1 causes a significant improvement in mass flux distribution close to the trailing edge. The effective gain over the overall wall roughness case can be attributed to the reduced blockage accounted for by the boundary layer thickness and reduction in the separated flow region. Thus, the localized strip presents itself as an improvement over the wall roughness case. Fig. 5-13 presents the contours of the meridional velocity at a streamwise location close to the blades trailing edge. The contour plots also reveal a reduction in the wake region at the blade trailing edge. This explains the gain in the mass flux observed in the Fig. 5-12.

Impeller Strip 2

The current section deals with analyzing the effect of adding localized roughness at the rotor strip 2 defined in Fig. 5-9(a). The study has been carried out by considering roughness heights and analyzing their effect on the impeller flow. Fig. 5-12 presents the effect of roughness strips in terms of blade to blade variation of the mass flux at the blade's trailing edge. It is evident from the curves depicted in Fig. 5-12 that it causes an increase in the mass flux distribution at the trailing edge of the impeller blade. This increase in the mass flux represents a reduction in the low momentum flow region at the trailing edge. However, in comparison to the mass flux gain achieved by adding roughness elements to the strip 1 (Fig.5-12), the gain achieved in this case is lower. It is also observed that an increase in the roughness height from 50 to 200 μm does not cause a significant improvement in the mass flux distribution at the trailing edge.

Further, the distribution of the meridional velocity at a streamwise location close to the blades trailing edge is depicted in the contour plots in Fig. 5-15. The addition of the roughness at the strip 2 causes a reduction in the low momentum wake region. However, the gain observed in this case is lower than the case in which roughness is introduced at strip 1.

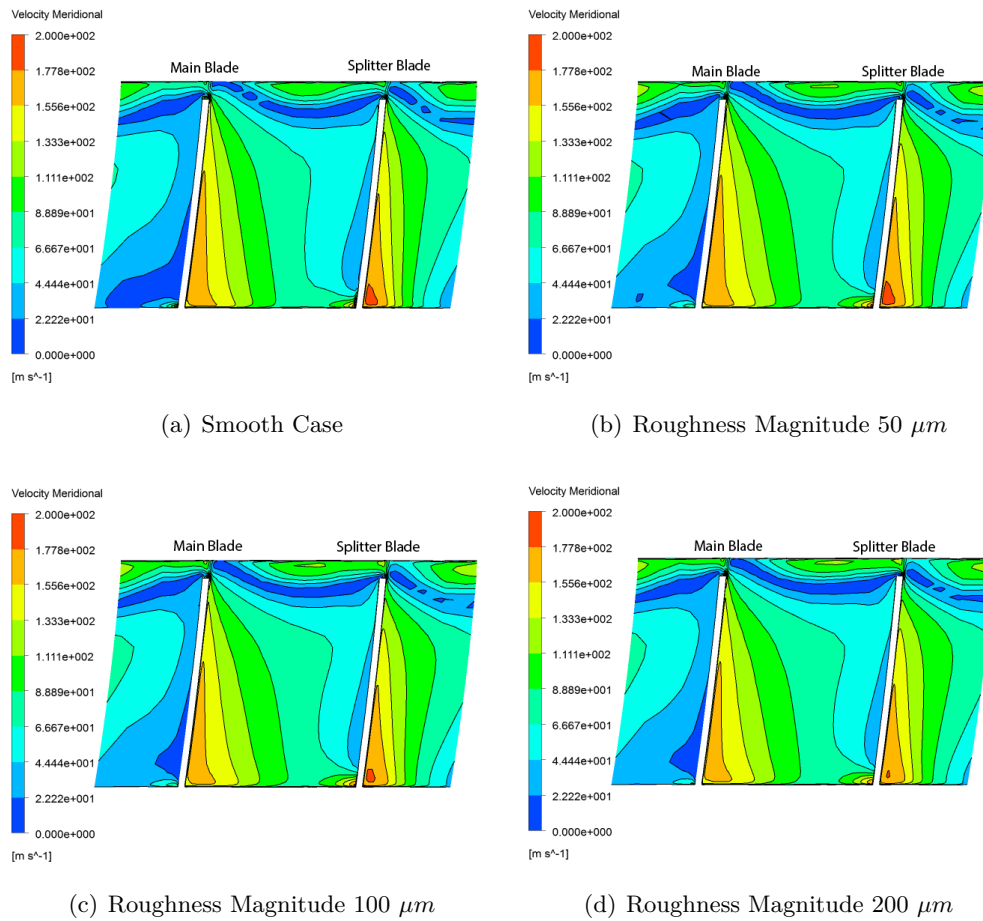


Figure 5-13: Meridional velocity contours depicting the influence of roughness strip 1 on the meridional velocity distribution at the impeller trailing edge

Impeller Strip 3

Fig. 5-16 presents the effect of adding localized roughness at the rotor strip 3 (Fig. 5-9(a)) on the impeller flow field. It can be inferred from the Fig. 5-16(a) that the roughness imposed at strip 3 of the impeller results in a reduction in the mass flux distribution at the impeller shroud close to the trailing edge in comparison with the roughness imposed at strip 1 and strip 2 in the impeller domain. Thus, the location 3 does not offer significant improvement in the flow stabilization. In addition to this, it can be seen that the increase in the roughness height causes a reduction in the mass flux distribution.

In order to further investigate the effect of roughness strip 3 on the impeller flow instability, meridional velocity contours have been plotted at a location close to the rotor's trailing edge. The plots reveal that the addition of roughness (Fig. 5-17(b) to 5-17(d)) results in a reduction in the low momentum region in comparison with the smooth case 5-17(a). In addition to this, it can also be inferred from the contour plots that, an increase in the roughness magnitude at the strip 3 causes an increase in the low momentum region relative to each other.

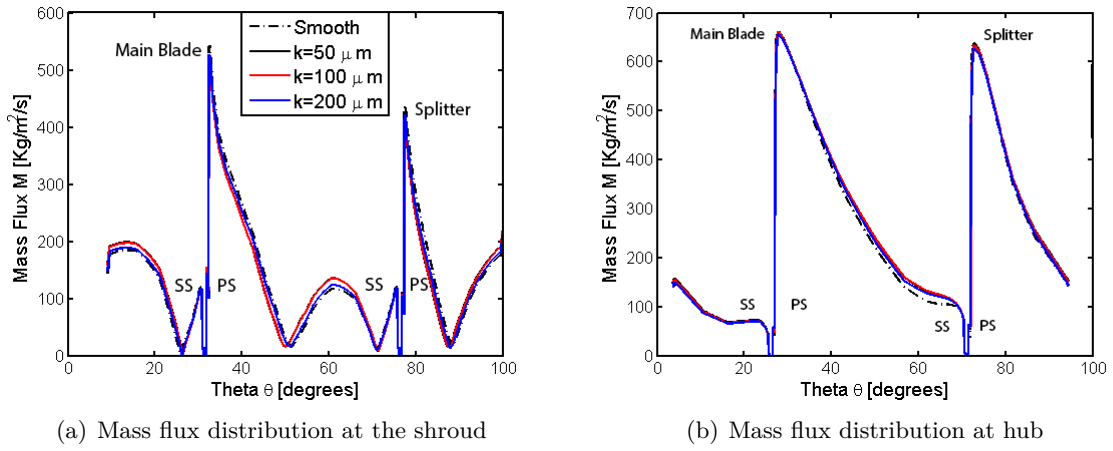


Figure 5-14: Modification of the mass flux distribution as a result of the localized roughness applied to strip 2 at the impeller

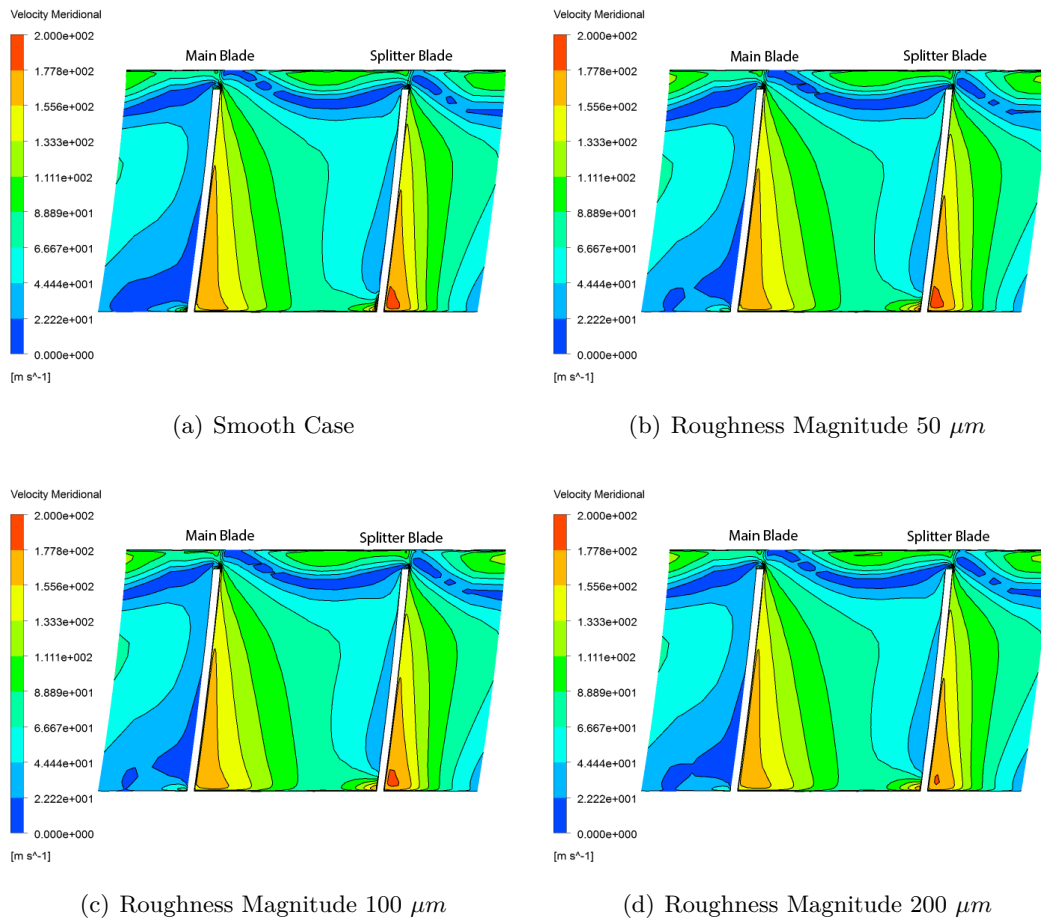


Figure 5-15: Meridional velocity contours location depicting the influence of roughness strip 2 on the meridional velocity distribution at the impeller trailing edge

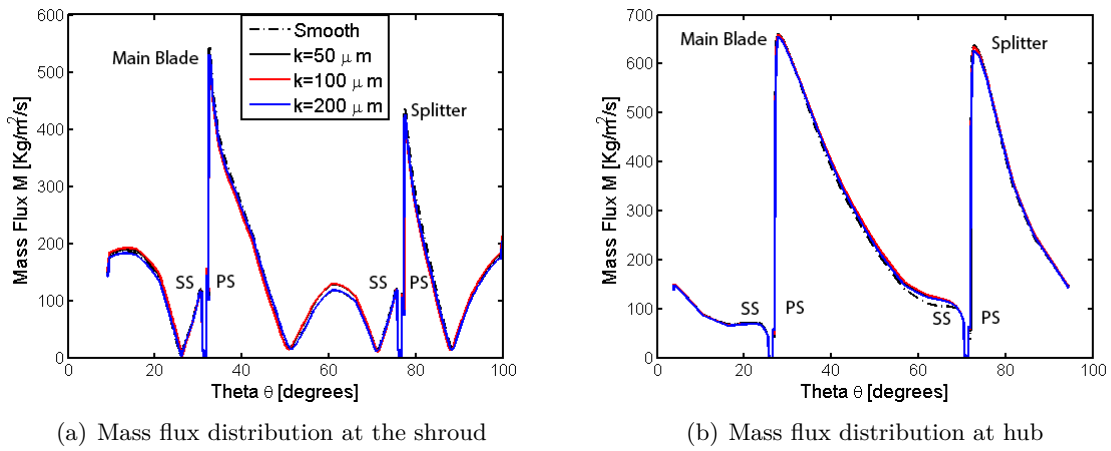


Figure 5-16: Modification of the mass flux distribution as a result of the localized roughness applied to strip 3 at the impeller

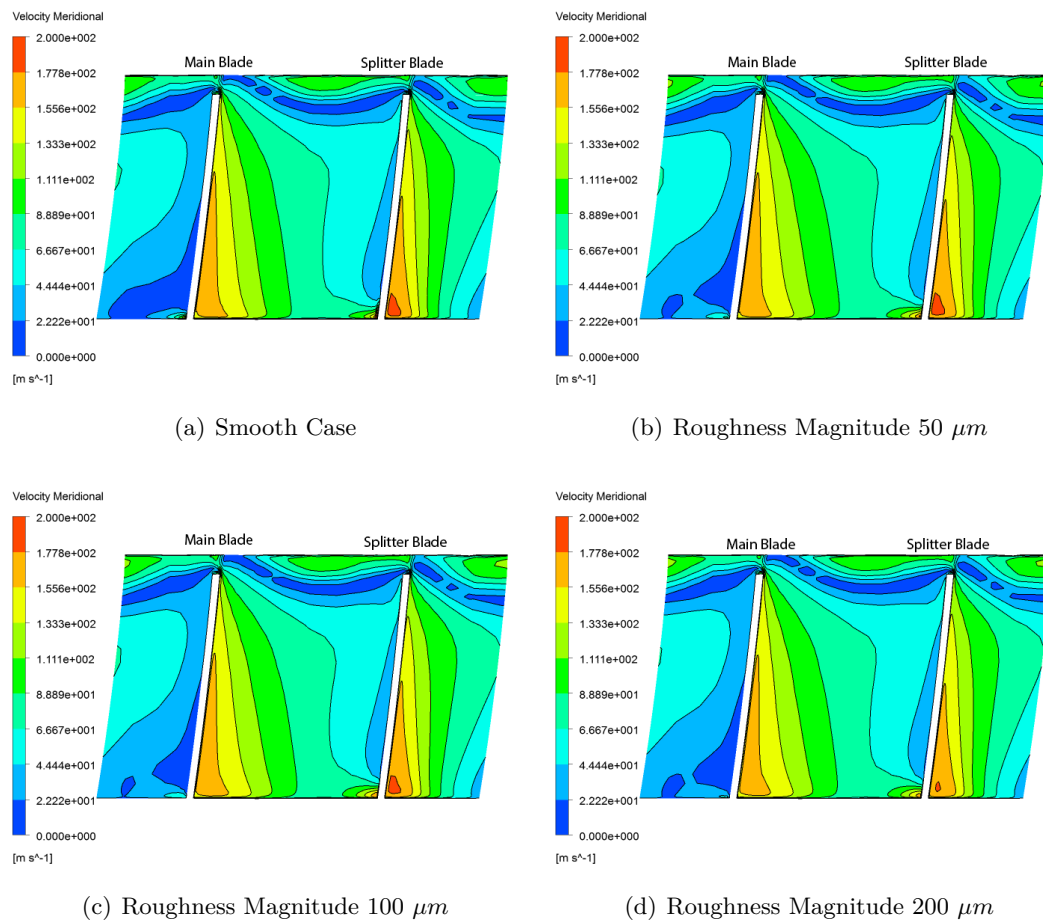


Figure 5-17: Meridional velocity contours depicting the influence of roughness strip 3 on the meridional velocity distribution at the impeller trailing edge

Summary and Conclusions

In this work, general purpose finite volume based solver, ANSYS CFX, has been adopted to perform flow and performance analysis of a centrifugal compressor that forms an integral part of the automotive turbocharger. For this purpose, the transition model formulation available in ANSYS CFX has been first used to evaluate and study the performance and flow field of a centrifugal compressor along a constant speed line. Secondly, the work focuses on evaluating the effect of surface roughness on the flow instabilities of a centrifugal compressor. This investigation results from the desire to improve the stability range of the centrifugal compressor.

Prior to evaluating the compressor performance and its analysis, the finite volume based RANS solver has been validated on 2D baseline test cases. These include flow over an adiabatic flat plate, roughened flat plate and a flat plate with imposed pressure gradient and roughness trips. This analysis has been performed to validate the ability of transition model to predict and model laminar to turbulent transition and also to validate its capability to predict the effect of surface roughness. The results obtained by the CFD simulations agree reasonably well with the test case reference data. Certain deviations are observed in the test cases with imposed surface roughness. These deviations can be attributed to the approximate correlations used for relating the equivalent surface roughness to the geometric roughness height of the roughness elements.

Next, the transition model formulation available in CFX has been validated for a turbomachinery test case. The model has been adopted for predicting the heat transfer over a highly loaded VKI transonic turbine guide vane. The turbine guide vane has been simulated for two flow configurations (MUR-235 and MUR-241). The results reveal that the numerical simulations underestimate the heat transfer coefficient over the blade surface. However, the model predicts the laminar to turbulent transition location at the suction side of the blade and has a good agreement with the reference test data. Thus, the model formulation available in CFX predicts the transition location fairly accurately.

After the model validation, comprehensive performance analysis of the test compressor has been carried out using the CFD tool. Firstly, the CFD setup of the compressor has been

validated by comparing the performance data obtained from numerical simulations with the experimental data. Overall, a close agreement is seen between the simulated performance and experimental data. However, some deviations in performance estimation are seen close to the choke point. Next, a detailed flow field analysis of the test compressor has been carried out at the peak efficiency point of the simulated speedline. Furthermore, a flow investigation has also been carried out with a view of understanding the evolution of unsteady flow in compressor with the reduction in the mass flow rate. The flow analysis at the peak efficiency point revealed the existence of a low relative Mach number region on the main blade suction side. This region grows from the shroud to the hub and is maximum near the blade trailing edge. In addition to this, the splitter blade's suction side exhibits a lower Mach number and also relatively smaller low-velocity region. This results in a higher outlet wake due at the main blade in comparison with that due to the splitter blade. The maximum loss production, observed in terms of the static entropy rise, is found close to the shroud and extends in the spanwise direction as a result of the low momentum region close to the main blade. Furthermore, the flow analysis reveals that at low flow rate operations, a significant portion of the impeller inlet flow is effected by the recirculating flow observed near the impeller shroud. Also, the mass flow reduction corresponding to different operating points (choke to surge) results in an increase in the low momentum wake region observed near the impeller blades. In addition to this, close to the stall limit, a recirculating region is observed near the diffuser shroud wall. All these flow phenomenon indicate unstable compressor operation.

Lastly, the report concludes by a parametric study about the effect of surface roughness on the flow instabilities in the centrifugal compressor. The roughness study has been split into two parts: the first part deals with analyzing the effect of adding wall surface roughness at the impellers' blade, impeller shroud, inlet shroud and diffuser shroud on the flow instabilities within the compressor's diffuser and impeller. In the second part, a study has been carried out by considering localized roughness strips on the main blade's suction side and the diffuser shroud. From the roughness analysis, it is observed that the surface roughness has a significant effect on the flow reversals at the diffuser shroud. The addition of the roughness elements to the diffuser shroud causes a significant reduction in flow reversals near the diffuser shroud. The application of roughness also results in complete elimination of the flow reversal near the diffuser hub. In the case of the impeller, the surface roughness causes a modification of the flow structure. However, the visualization of the flow field at the impeller poses challenging task for the steady state simulations as a result of the unsteady nature of the flow. Increase in the roughness magnitude causes a reduction in the low momentum wake regions along the impeller blade. In addition to this, it also causes an improvement in the mass flux distribution close to the trailing edge. However, increased blockage due to an increase in boundary layer thickness inhibits the gain achieved in terms of the reduction in the low momentum wake regions. The analysis also shows that the increase of the roughness magnitude from 50-200 μm does not cause a significant difference in terms of relative improvement of the flow structure. Finally, the report discusses overcoming the shortcomings of the overall roughness analysis by investigating the effect of adding localized roughness strips on the main blade's suction side and diffuser's shroud. The analysis reveals that the addition of roughness strip close to the diffuser shroud results in significant improvement in the flow structure. Furthermore, addition of the roughness strip close to the impeller blades leading edge results in the reduction of low momentum region. In this case, the increase in the roughness magnitude has a similar effect on the flow structure.

Recommendations and Future Work

The results obtained from the current analysis seem effective in terms of reducing the flow instabilities in a centrifugal compressor and hence demand further investigation. However, since the present work analyzes the improvement in flow instabilities using steady state simulations, the precise effect of the addition of roughness cannot be determined. Thus, in order to further investigate the improvement in the stability range, time-dependent simulations are proposed and recommended for the future evaluation. Furthermore, in order to validate the results obtained from the simulations, comprehensive experimental evaluations have been planned at MTEE.

Appendix A

Reference Data for the Test Cases

The relevant geometric and boundary data pertaining to the test cases documented in chapter 2 is presented in this appendix. Table 1 presents the boundary condition data relevant to the smooth flat plate, while Table A2 presents boundary layer data pertaining to the roughened flat plate.

Table A-1: Boundary data corresponding to the smooth flat plate

Boundary	Parameter	Magnitude
Reference Values	ρ_{∞} , [kg/m^3]	1.2
	T_{∞} , [K]	101634
	P_{∞} , [Pa]	293.1
	μ_{∞} , [$Pa.s$]	6.743e-05
Wall	Heat Transfer	Adiabatic
	U_{wall} , [m/s]	0
	k_{wall} , [m^2/s^2]	0
Inlet	P_{in} , [Pa]	101634
	ω_{in} , [$1/s$]	30
	k_{in} , [m^2/s^2]	40000
	T_{in} , [K]	293.1
Outlet	P_{out} , [Pa]	0.953e5

Table A-2: Boundary data corresponding to the roughened flat plate

Boundary	Parameter	Magnitude
Reference Values	$\rho_\infty, [kg/m^3]$	1.2
	$T_\infty, [K]$	101325
	$P_\infty, [Pa]$	293.1
	$\mu_\infty, [Pa.s]$	17.952e-6
Wall	Heat Transfer	Adiabatic
	$U_{wall}, [m/s]$	0
	$k_{wall}, [m^2/s^2]$	0
Inlet	$P_{in}, [Pa]$	101325
	$U_{in}, [m/s]$	100
	$Tu_{in}, [%]$	1.1
	$T_{in}, [K]$	293.1
Outlet	$P_{out}, [Pa]$	0.954e5

Table A-3: Boundary data corresponding to the roughened flat plate with imposed pressure gradient

Boundary	Parameter	Magnitude
Reference Values	$\rho_\infty, [kg/m^3]$	1.2
	$T_\infty, [K]$	101325
	$P_\infty, [Pa]$	293.1
	$\mu_\infty, [Pa.s]$	2.65e-05
Wall	Heat Transfer	Adiabatic
	$U_{wall}, [m/s]$	0
	$k_{wall}, [m^2/s^2]$	0
Inlet	$P_{in}, [Pa]$	101325
	$Tu_{in}, [%]$	0.5
	$T_{in}, [K]$	293.1
Outlet	$P_{out}, [Pa]$	101287

Table A-4: Boundary data corresponding to the turbomachinery test case-VKI transonic turbine guide vane

Boundary	Parameter	VKI-MUR235	VKI-MUR241
Reference Values	ρ_{∞} , [kg/m^3]	1.54	2.72
	T_{∞} , [K]	416.3	416.3
	P_{∞} , [Pa]	1.828e5	3.257e5
	μ_{∞} , [$Pa.s$]	1.716e-05	
Wall	T_{wall}	300	300
	U_{wall} , [m/s]	0	0
	k_{wall}^* , [m^2/s^2]	0	0
Inlet	P_{in} , [Pa]	1.828e5	3.257e5
	ω_{in} , [$1/s$]	5e4	1.1e5
	k_{in} , [m^2/s^2]	20.55	20.55
	T_{in} , [K]	416.4	416.4
Outlet	P_{out} , [Pa]	1.049e5	1.547e5

Appendix B

Matlab Code for the Volute Performance Estimation

```
clear all
clc

TT5 =377.155;
P5 =141297;

PT5 =189683 ;
VT5 =96.081;

VM5 = 215.089 ;
% Diffuser

R5 = 0.035;      % Outlet Radius (Diffuser) [m]
B5 = 0.00237;   %Diffuser Width at Outlet [m]

% Scroll
R6 = 0.03688;   %Scroll Centre Radius (m)
D7 = 0.0384;    % Exit Diameter (Scroll) (m)

% Input Thermodynamic Parameters
P01=101325;     %Inlet Total Pressure (Pa)
T01=293.15;     %Inlet Total Temperature (K)

% Constants
R=287;         %Gas constant for air (j/kg/k)
```

```

CP = 1005;    %Specific Heat of air at constant pressure (j/kg/k)
GMA = 1.4;    %Isentropic Coefficient

%*****Compressor Scroll Exit Parameters*****%

F1=.6;
F2=.6;

AR_SCRL=((D7)^2)/(8 * R5 * B5);    %Area Ratio (m2)
LMDA=VT5/VM5;    %Inlet Swirl Parameter

KM = F1 * (1/(1 + (LMDA^2)));    %Meridional Loss Component
KT = F2 * ((R5/R6)^2) * ((LMDA - (1/AR_SCRL))^2)/(1 + (LMDA)^2); %Tangential Loss
K_SCRL = KM + KT;    %Total Scroll Pressure Loss

if LMDA * AR_SCRL > 1    %Flow Diffuses

CP_SCRL = (2 * (LMDA - (1/AR_SCRL)))/(AR_SCRL * (1 + (LMDA)^2)); % Pressure
Recovery
else
CP_SCRL = (LMDA^2 - (1/AR_SCRL^2))/(1 + LMDA^2);
end

TT7 = TT5;    %Scroll Exit Total Temperature (K)
PT7 = PT5 - K_SCRL * (PT5 - P5);    %Scroll Exit Total Pressure (Pa)
P7 = P5 + CP_SCRL * (PT5 - P5);    %Scroll Exit Static Pressure (Pa)
T7 = TT7/((PT7/P7)^((GMA - 1)/GMA));    %Static Temperature at diffuser Exit (k)
M7 = sqrt((2/(GMA - 1)) * (((PT7/P7)^((GMA - 1)/GMA)) - 1));%Diffuser Exit Mach No
V7 = M7 * sqrt(GMA * R * T7); %Velocity at Scroll Exit (m/s)

%*****Stage Performance*****%

PRTT = PT7/P01 %Total to Total Stage Pressure Ratio
ETATT = (((PRTT)^((GMA - 1)/GMA)) - 1)/((TT7/T01) - 1) * 100 %Total to Total Eff

```

Experimental Compressor Map

Fig. C-1 below shows the experimental performance map of the test compressor in terms the variation of the pressure ratio with the volumetric flow rate. The experimental map has been obtained as a result of the experiments conducted at MTEE.

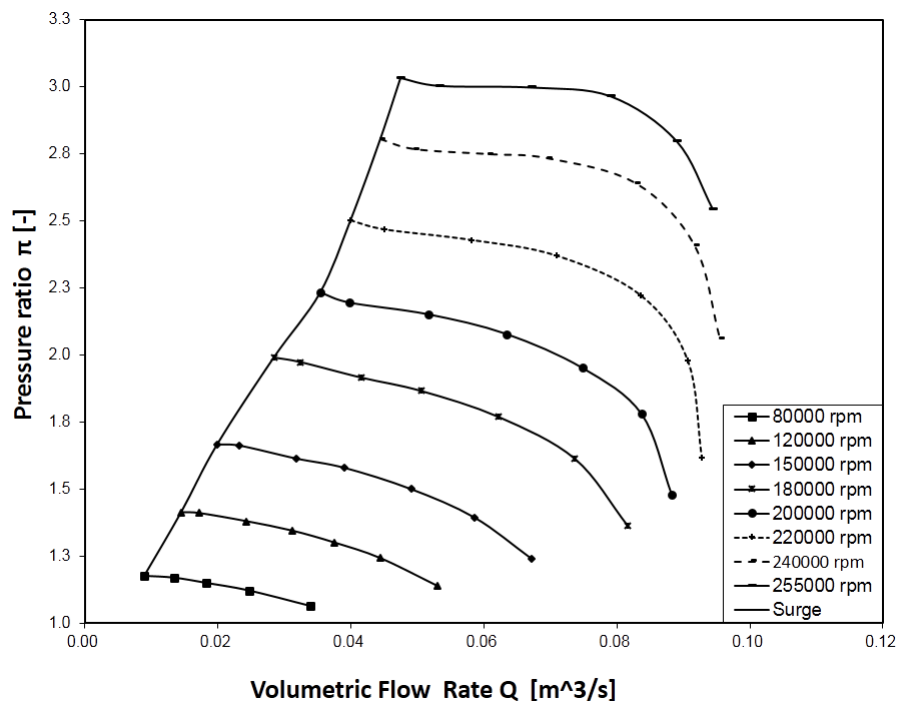


Figure C-1: Experimental map of the test compressor

Appendix D

Component Wise Mesh Distribution

This Appendix provides the component wise mesh distribution for the different components within the centrifugal compressors domain. The mesh elements for the inlet duct, impeller and the diffuser is documented in tableD-1.

Table D-1: Component wise mesh in the compressor domain

S.No	Component	Mesh Size
1	Inlet Duct	50344
2	Impeller	218844
3	Diffuser	126000

Bibliography

- [1] D. Japikse, “Stall, stage stall, and surge,” in *Proceedings of the Tenth Turbomachinery Symposium*, pp. 1–13, 1981.
- [2] R. Antonia and P.-Å. Krogstad, “Turbulence structure in boundary layers over different types of surface roughness,” *Fluid Dynamics Research*, vol. 28, no. 2, pp. 139–157, 2001.
- [3] R. Raspopov, “Modelling curvature effects on turbulence for turbomachinery flows,” Master’s thesis, TU Delft, Netherlands, 2013.
- [4] D. Japikse, “Centrifugal compressor design and performance(book),” *Wilder, VT: Concepts ETI, Inc, 1996.*, 1996.
- [5] W. Jansen, “Rotating stall in a radial vaneless diffuser,” *Journal of Fluids Engineering*, vol. 86, no. 4, pp. 750–758, 1964.
- [6] J. Paduano, E. Greitzer, and A. Epstein, “Compression system stability and active control,” *Annual Review of Fluid Mechanics*, vol. 33, no. 1, pp. 491–517, 2001.
- [7] Y. Senoo and Y. Kinoshita, “Influence of inlet flow conditions and geometries of centrifugal vaneless diffusers on critical flow angle for reverse flow,” *Journal of Fluids Engineering*, vol. 99, no. 1, pp. 98–102, 1977.
- [8] P. Frigne and R. Van den Braembussche, “Distinction between different types of impeller and diffuser rotating stall in a centrifugal compressor with vaneless diffuser,” *Journal of Engineering for Gas Turbines and Power*, vol. 106, no. 2, pp. 468–474, 1984.
- [9] Y. Tsujimoto, Y. Yoshida, and Y. Mori, “Study of vaneless diffuser rotating stall based on two-dimensional inviscid flow analysis,” *Journal of fluids engineering*, vol. 118, no. 1, pp. 123–127, 1996.
- [10] S. Niazi, *Numerical simulation of rotating stall and surge alleviation in axial compressors*. PhD thesis, Georgia Institute of Technology, 2000.

- [11] R. L. Simpson, "Turbulent boundary-layer separation," *Annual Review of Fluid Mechanics*, vol. 21, no. 1, pp. 205–232, 1989.
- [12] M. S. Genç, I. Karasu, H. H. Acikel, M. T. Akpolat, and M. Genc, "Low reynolds number flows and transition," *Low Reynolds Number Aerodynamics and Transition, Genc, MS Ed.; InTech: Rijeka, Croatia*, pp. 1–28, 2012.
- [13] R. E. Mayle, "The 1991 igt scholar lecture: The role of laminar-turbulent transition in gas turbine engines," *Journal of Turbomachinery*, vol. 113, no. 4, pp. 509–536, 1991.
- [14] F. Menter, R. Langtry, and S. Völker, "Transition modelling for general purpose cfd codes," *Flow, Turbulence and Combustion*, vol. 77, no. 1-4, pp. 277–303, 2006.
- [15] R. Langtry, "A correlation based transition model using local variables for unstructured parallelized cfd codes," 2006.
- [16] S. Likki, S. Y.B., P. Huang, F. Menter, and R. Langtry, "A correlation-based transition model using local variables -part 1: Model formulation," *Journal of Turbomachinery*, vol. 128, pp. 413–422, 2004.
- [17] S. Likki, S. Y.B., P. Huang, F. Menter, and R. Langtry, "A correlation-based transition model using local variables -part ii: Test cases and industrial applications," *Journal of Turbomachinery*, vol. 128, pp. 423–434, 2004.
- [18] A. Jamal, "Boundary layer tripping by a roughness element," Tech. Rep. 4, 1996.
- [19] P. Jonáš, O. Hladík, O. Mazur, and V. Uruba, "By-pass transition of flat plate boundary layers on the surfaces near the limit of admissible roughness," in *Journal of Physics: Conference Series*, vol. 318, p. 032030, IOP Publishing, 2011.
- [20] J. Nikuradse, *Laws of flow in rough pipes*. National Advisory Committee for Aeronautics Washington, 1950.
- [21] J. P. Bons, "A review of surface roughness effects in gas turbines," *Journal of Turbomachinery*, vol. 132, no. 2, p. 021004, 2010.
- [22] H. Schlichting, "Boundary layer theory," 1979.
- [23] H. Coleman, B. Hodge, and R. Taylor, "A re-evaluation of schlichting's surface roughness experiment," *Journal of fluids engineering*, vol. 106, no. 1, pp. 60–65, 1984.
- [24] R. L. Simpson, "A generalized correlation of roughness density effects on the turbulent boundary layer.," *AIAA Journal*, vol. 11, no. 2, pp. 242–244, 1973.
- [25] A. E. Von Doenhoff and E. A. Horton, *A low-speed experimental investigation of the effect of a sandpaper type of roughness on boundary-layer transition*. NACA, 1958.
- [26] M. W. Pinson and T. Wang, "Effects of leading-edge roughness on fluid flow and heat transfer in the transitional boundary layer over a flat plate," *International journal of heat and mass transfer*, vol. 40, no. 12, pp. 2813–2823, 1997.

-
- [27] X. F. Zhang and H. Hodson, “Combined effects of surface trips and unsteady wakes on the boundary layer development of an ultra-high-lift lp turbine blade,” *Journal of turbomachinery*, vol. 127, no. 3, pp. 479–488, 2005.
- [28] S. B. Pope, *Turbulent flows*. Cambridge university press, 2000.
- [29] F. R. Menter, “Two-equation eddy-viscosity turbulence models for engineering applications,” *AIAA journal*, vol. 32, no. 8, pp. 1598–1605, 1994.
- [30] D. Bergstorm, N. Kotey, and M. Tachie, “The effects of surface roughness on the mean velocity profile in a turbulent boundary layer,” *Journal of Fluids Engineering*, vol. 124, pp. 664–370, 2002.
- [31] A. Savill, “A synthesis of t3 test case predictions,” *Numerical simulation of unsteady flows and transition to turbulence*, pp. 404–442, 1992.
- [32] P. Dassler, D. Kožulović, and A. Fiala, “Modelling of roughness-induced transition using local variables,” in *V European Conference on CFD, ECCOMAS CFD*, 2010.
- [33] T. Arts and M. L. de Rouvroit, “Aero-thermal performance of a two-dimensional highly loaded transonic turbine nozzle guide vane: A test case for inviscid and viscous flow computations,” *Journal of turbomachinery*, vol. 114, no. 1, pp. 147–154, 1992.
- [34] Fluent, “12.1 user manual,” *ANSYS Inc*, 2010.
- [35] A. Javed and E. Kamphues, “Evaluation of the influence of volute roughness on turbocharger compressor performance from a manufacturing perspective,” in *Proceedings of the ASME Turbo Expo 2014*, 2014.
- [36] M. Olivero, *Evolution of a centrifugal compressor: From turbocharger to micro gas turbine applications*. PhD thesis, TU Delft, Delft University of Technology, 2012.
- [37] R. Chodkiewicz, K. Sobczak, A. Papierski, and T. Borzęcki, “Cfd code-a useful tool for the turbomachinery designer,” *TASK Quarterly: scientific bulletin of Academic Computer Centre in Gdansk*, vol. 6, pp. 553–575, 2002.
- [38] F. Breugelmans and M. Sen, “Prerotation and fluid recirculation in the suction pipe of centrifugal pumps,” in *Proc. 11th Int. Pump Symp., Texas A&M Univ*, pp. 165–180, 1982.
- [39] M. Ishida, D. Sakaguchi, and H. Ueki, “Suppression of rotating stall by wall roughness control in vaneless diffusers of centrifugal blowers,” *Journal of turbomachinery*, vol. 123, no. 1, pp. 64–72, 2001.
- [40] A. Abdelhamid, “Effects of vaneless diffuser geometry on flow instability in centrifugal compression systems,” in *American Society of Mechanical Engineers, Gas Turbine Conference and Products Show, Houston, Tex*, 1981.
- [41] A. Jaatinen-Värri, P. Röyttä, T. Turunen-Saaresti, and A. Grönman, “Experimental study of centrifugal compressor vaneless diffuser width,” *Journal of Mechanical Science and Technology*, vol. 27, no. 4, pp. 1011–1020, 2013.

-
- [42] H. Simon and A. Bulskamper, "On the evaluation of reynolds number and relative surface roughness effects on centrifugal compressor performance based on systematic experimental investigations," *Journal of Engineering for Gas Turbines and Power*, vol. 106, no. 2, pp. 489–498, 1984.
- [43] R. C. Dean and Y. Senoo, "Rotating wakes in vaneless diffusers," *Journal of Fluids Engineering*, vol. 82, no. 3, pp. 563–570, 1960.
- [44] J. Kurokawa, J. Matsui, T. Kitahora, S. L. Saha, *et al.*, "A new passive device to control rotating stall in vaneless and vaned diffusers by radial grooves," 1997.